

ULTRASONIC CHARACTERIZATION
OF THREE ANIMAL MAMMARY TUMORS
FROM THREE-DIMENSIONAL ACOUSTIC TISSUE MODELS

BY
JONATHAN M. MAMOU

Dipl., Ecole Nationale Supérieure des Télécommunications, Paris, 2000
M.S., University of Illinois at Urbana-Champaign, 2002

DISSERTATION

Submitted in partial fulfillment of the requirements
for the degree of Doctor of Philosophy in Electrical Engineering
in the Graduate College of the
University of Illinois at Urbana-Champaign, 2005

Urbana, Illinois

ABSTRACT

This dissertation investigated how three-dimensional (3D) tissue models can be used to improve ultrasonic tissue characterization (UTC) techniques. Anatomic sites in tissue responsible for ultrasonic scattering are unknown, which limits the potential applications of ultrasound for tumor diagnosis. Accurate 3D models of tumor tissues may help identify the scattering sites. Three mammary tumors were investigated: a rat fibroadenoma, a mouse carcinoma, and a mouse sarcoma. A 3D acoustic tissue model, termed 3D impedance map (3DZM), was carefully constructed from consecutive histologic sections for each tumor. Spectral estimates (scatterer size and acoustic concentration) were obtained from the 3DZMs and compared to the same estimates obtained with ultrasound. Scatterer size estimates for three tumors were found to be similar (within 10%). The 3DZMs were also used to extract tissue-specific scattering models. The scattering models were found to allow clear distinction between the three tumors. This distinction demonstrated that UTC techniques may be helpful for noninvasive clinical tumor diagnosis.

Cette thèse est entièrement dédiée à ma femme, ma famille et mes amis.

ACKNOWLEDGMENTS

I would like to thank my research advisor, Professor William O'Brien. His outstanding guidance, patience, and dedication to my growth as a researcher can not be put into words. I would also like to thank my committee members, Professors James Zachary, Leon Frizzell, Weng Chew, and Michael Insana. They all contributed in a significant way to my education. I also acknowledge the unconditional and day to day support of Professor Michael Oelze.

I would like to express my gratitude to Sue Clay. She makes anything impossible possible and anything possible easy. I am also very grateful to the many and diverse individuals who populated BRL during my years here. In particular, I would like to express my sincere appreciation to Dr. Rita Miller and James Blue.

I also had the chance to collaborate with the laboratoire d'imagerie paramétrique in Paris, France. I would like to mention the following individuals: Dr. Pascal Laugier, Dr. Lori Bridal, and Azzdine Ammi.

I would like to thank my parents for their endless support. Lastly, I would like to acknowledge Master Namsoo Hyong who helped me grow as a Martial Artist and as a Martial Art Instructor.

TABLE OF CONTENTS

LIST OF ABBREVIATIONS	ix
CHAPTER 1 INTRODUCTION	1
1.1 Quantitative Diagnostic Ultrasound	1
1.2 Breast Cancer Diagnosis	1
1.3 Frequency-Dependent Information	2
1.4 Scattering Sources	4
1.5 Three-Dimensional Modeling of Tissue	4
1.6 Ultrasonic Tissue Characterization	5
1.7 Noninvasive Diagnostic and Monitoring of Disease	6
CHAPTER 2 ULTRASONIC SCATTERING THEORY	7
2.1 Sound Scattering by Uniform Spheres and Cylinders	7
2.1.1 Faran's theory for a solid cylinder	7
2.1.2 Faran's theory for solid sphere	9
2.1.3 Faran's theory and biological materials	9
2.2 Weak Scattering in an Inhomogeneous Medium	10
2.3 Form Factor	11
2.3.1 Usual form factors	12
2.3.2 Anisotropic FF	13
2.3.3 Form factor from Faran's theory	14
2.3.4 Derivation of an advanced form factor	15
2.4 Scattering Structures and FF	17
2.5 Figures	18
CHAPTER 3 THREE-DIMENSIONAL MODELING METHODOLOGIES .	20
3.1 Tissue Preparation	20
3.2 Three-Dimensional Reconstruction	21
3.2.1 Contrast Adjustment	22
3.2.2 Registration	23
3.2.3 Interpolation	28

3.2.4	Assignment of acoustic impedance values	31
3.2.5	Three-dimensional renderings	32
3.3	Validation of the Methodologies	32
3.3.1	Registration algorithms	32
3.3.2	Missing section interpolation	33
3.3.3	Nine-section reconstruction	33
3.4	Sarcoma Acoustic Models	35
3.5	Fibroadenoma and Carcinoma Acoustic Models	37
3.6	Tables and Figures	37
CHAPTER 4 TISSUE CHARACTERIZATION METHODOLOGIES		59
4.1	Estimation Technique	59
4.2	Form Factor and Uniqueness of Estimation Results	62
4.3	Comparison of the 3DZM and Ultrasound Estimation Techniques	63
4.4	3DZM-Deduced Form Factor	64
4.4.1	Theory	64
4.4.2	Methodology	65
4.4.3	Implementation	66
4.5	Two-Parameter Exponential Model	68
4.6	Tables and Figures	70
CHAPTER 5 TISSUE CHARACTERIZATION RESULTS		73
5.1	Simulations	73
5.1.1	Single-population simulations	73
5.1.2	Two-population simulations	75
5.1.3	Gaussian size distribution simulations	76
5.2	Validation of the 3DZM-FF Extraction	80
5.3	Tumor Tissue Characterization Using the Gaussian FF	84
5.3.1	Rat fibroadenoma results	84
5.3.2	4T1 mouse mammary carcinoma results	85
5.3.3	EHS mouse sarcoma results	85
5.3.4	Comparison with ultrasonic results	86
5.3.5	Gaussian FF limitations	87
5.4	Tissue Characterization Using 3DZM-Deduced FF	88

5.4.1	Rat fibroadenoma results	89
5.4.2	4T1 mouse mammary carcinoma results	89
5.4.3	EHS mouse sarcoma results	90
5.4.4	Ultrasonic characterization	90
5.5	Tables and Figures	92
CHAPTER 6 CONCLUSIONS AND FUTURE WORK		109
6.1	Three-Dimensional Modeling Strategies	109
6.1.1	Improvement of the modeling strategies	109
6.1.2	Extensions of the modeling strategies	110
6.2	Three-Dimensional Impedance Maps and Tissue Characterization . . .	112
6.2.1	Assignment of acoustic impedance	112
6.2.2	Resolution	113
6.2.3	Biological phantoms	113
6.3	Identification of the Ultrasonic Scattering Sites	114
6.3.1	Identification using size estimates	114
6.3.2	Identification using form factors	115
6.4	Clinical Implementations	116
APPENDIX A HISTOPATHOLOGIC FEATURES		118
A.1	Table	119
APPENDIX B DERIVATION OF THE GAUSSIAN-GAUSSIAN FF . . .		120
APPENDIX C DERIVATION OF A POWER SPECTRUM		122
APPENDIX D OBLIQUE CUT THROUGH A THREE-DIMENSIONAL HISTOLOGIC VOLUME		124
D.1	Figure	124
REFERENCES		125
AUTHOR'S BIOGRAPHY		132

LIST OF ABBREVIATIONS

1D	One-dimensional
2D	Two-dimensional
3D	Three-dimensional
3DZM	Three-dimensional impedance map
BRL	Bioacoustics Research Laboratory
CT	X-ray computed tomography
DOF	Degree of freedom
ECM	Extracellular matrix
EHS	Englebreth-Holm-Swarm
FF	Form factor
H&E	Hematoxyn and eosin
MI	Mutual information
MRI	Magnetic resonance imaging
MSE	Mean squared error
MSTD	Mean standard deviation
NMI	Normalized mutual information
QUS	Quantitative ultrasound
ROI	Region of interest
RF	Radio frequency
RGB	Red green blue
RMSD	Root mean squared image difference
SAF	Spatial autocorrelation function
SNR	Signal to noise
SSS	Stretched spherical shell
STD	Standard deviation
UTC	Ultrasonic tissue characterization

CHAPTER 1

INTRODUCTION

1.1 Quantitative Diagnostic Ultrasound

Diagnostic ultrasound has become a significant modality in the medical imaging world [1]. It is a fast, safe and relatively low-cost modality. However, the competing imaging modalities such as magnetic resonance imaging (MRI) or X-ray computed tomography (CT) are now going towards advanced methodologies that include quantitative and functional imaging [2, 3]. Thus, if diagnostic ultrasound wants to stay competitive in the medical imaging world, it is necessary to go beyond qualitative (i.e., morphological) imaging. The work presented in this dissertation investigates how ultrasound imaging can be extended beyond the production of qualitative images. Quantitative ultrasound (QUS) images which are being investigated are believed to have great diagnostic potential. To achieve meaningful construction of this new type of ultrasound imaging, the spectral content (i.e., the frequency-dependent information) contained in the echo signals needs to be understood, correctly interpreted and displayed. Thus, this dissertation focuses on the basic science aspects of QUS: the fundamental understand fundamentally how ultrasound interacts with biological tissue microstructure. Part of this fundamental research was conducted on three animal models of human breast cancers. The goal was hence to create QUS images that would help in detection and diagnosis (characterization) of breast tumors.

1.2 Breast Cancer Diagnosis

Breast cancer is a very serious disease in the United States. There are over 200 000 new cases of invasive breast cancer in women every year and there will be over 40 000 deaths related to breast cancer in 2005 [4].

Early detection of cancer is critical; prognosis is much better when the disease is detected at an early stage. Nowadays, breast cancer is usually detected by

mammography, self-examination, or clinical breast examination. Mammography has been able to detect smaller tumors than palpations [5]. However, it is also demonstrated that about 15% of palpable cancers are not detected by mammography [6]. Thus, to maximize chances of detection both palpation and mammography are necessary.

Once a suspicious cyst or structure has been detected in the breast, the next step is usually to extract a sample of the suspicious tissue (biopsy). Then, tissue histology is assessed by a pathologist who can diagnose the patient's medical condition and for example, assess the stage of the cancer. Appendix A reviews the histologic features of tissue used for diagnosis. Histologic assessment of biopsy tissue is still regarded as the gold standard for breast cancer diagnosis. However, biopsy is far from a perfect diagnostic tool. Biopsy is an invasive, time-consuming, and expensive procedure. Even more importantly, sometimes tissue samples may have been extracted from a part of the breast that does not contain pathologic tissues, thus leading to a false negative diagnosis.

QUS may offer the exact opposite of the biopsy. In particular, it is noninvasive, virtually real time, and inexpensive. Furthermore, QUS techniques rely on the frequency-dependent content of the ultrasonic echo signals in order to quantify the same tissue microstructures that pathologists use to diagnose diseases. However, understanding how ultrasound interacts with tissue microstructures is necessary to correctly interpret the frequency-dependent content and reconstruct meaningful QUS images. This fundamental understanding is challenging and the research presented in this dissertation is meant to lay the foundations for new strategies to comprehend such complicated physical phenomena.

1.3 Frequency-Dependent Information

Conventional ultrasonic images (B-mode images) are derived from backscattered radio frequency (RF) echo signals [1]. The RF echoes are created by reflections from interfaces between acoustically different regions (macrostructure) and by coherent and incoherent scattering from tissue microstructure. Those echo signals contain frequency-dependent information about the smaller scale tissue structures (< wavelength). B-mode image processing removes the frequency-dependent content available in the RF echo signals. B-mode images are good at displaying larger scale

tissue structures ($>$ wavelength) but, to display and quantify smaller scale structures, the frequency-dependent content must be utilized.

The RF echo signals backscattered from biological tissues contain information about the size, shape, number, and relative impedance (ratio of the acoustic impedance difference between the background and the scatterers to that of the background, the acoustic impedance is defined as the product of the density and the propagation speed of sound) of the scattering objects. The backscattered signal is a superposition of wavelets scattered from numerous small structures confined within the volume of ensonified tissue. The frequency-dependent backscattered signal is dependent on the average tissue properties (size, shape, number, compressibility, density) of the scatterers within the ensonified region relative to the compressibility and density of the medium surrounding the scatterers [7]. The backscattered signal is, therefore, modeled as a statistical distribution of scatterers.

It is hypothesized that enhancing existing B-mode images with quantified physical properties of the average tissue microstructure can improve diagnosis of diseased tissue. QUS images, images enhanced by scatterer parameters like the average scatterer size and acoustic concentration (product of the number density and the square of the relative acoustic impedance of the scatterers), have successfully been used to characterize different aspects of tissue microstructures. Noteworthy are the pioneering studies that have demonstrated theoretically and experimentally the ability to ultrasonically quantify ocular, liver, prostate, renal, and cardiac tissues [8–11]. Research revealed [12] that the effective scatterer size in ocular tumors was a strong indicator of cancer. Further, QUS results have provided greater diagnostic accuracy in prostate cancer detection and lesion localization than all other noninvasive techniques combined [13, 14]. Anisotropy measurements of renal tissues showed that changes in the scatterer strength (acoustic concentration) were responsible for the anisotropy of backscatter rather than changes in scatterer size [11]. QUS imaging techniques were shown to be capable of differentiating among conditions that caused increased cortical echogenicity and structural changes like glomerular hypertrophy [15–18]. Furthermore, QUS measurements agreed well with physical measurements of those structures in biopsy samples.

1.4 Scattering Sources

Even though the QUS images (scatterer size and acoustic concentration) have shown their effectiveness in differentiating masses in animal mammary tumor models, what is missing to more fully exploit the QUS approach is an understanding of the anatomical scattering sources. This understanding is hypothesized to lead to the identification of the actual anatomical scattering sites in tissues. Identification of scattering sites will lead to improved scattering models. These improved models will yield more accurate and precise parameter-estimation techniques from which it is also hypothesized to lead to QUS capabilities for diagnosing disease. Identification of the scattering sites is also important for estimating the optimal frequency range of interrogation for different kinds of tissues. To help in identifying the potential scattering sources on a tissue-specific basis, it is important to have a clear understanding of the fundamental ultrasonic scattering theories. These theories and ultrasonic scattering models will be reviewed in Chapter 2.

1.5 Three-Dimensional Modeling of Tissue

The necessity of being capable of modeling tissue has become critical in the last 20 years for further development of the diagnostic potential of ultrasound technologies. Specifically, the scattering sources are not identified and limit the understanding of QUS images. Modeling tissue may be extremely helpful to identify scattering structures. It is hypothesized that tissue microstructure is responsible for ultrasound scattering [19]; thus, if accurate tissue models can be constructed, then clever techniques could be devised to identify scattering sources. Therefore, a novel approach is introduced herein to obtain three-dimensional (3D) models of tissue to help in discovering the anatomical structures responsible for ultrasonic scattering. This approach uses volume sections (3D histologic maps) corresponding to actual scanned tumor volumes to generate a 3D acoustic model of tissue or 3D impedance map (3DZM). The 3DZMs are created by aligning serial photomicrographs of stained histologic tumor sections. Impedance values are assigned to the different stained structures by the use of look-up tables of acoustical properties of the different tissue elements. Furthermore, ultrasonic scattering theories (Chapter 2) indicate that the Fourier transform of the 3D spatial autocorrelation function (SAF) of the 3DZM can

be used to estimate scatterer properties. A similar approach has been shown to be successful in the case of trabecular bones [20], where a binary 3D impedance map was used to describe bone microstructures.

However, the reconstruction of the 3DZMs are challenging and utmost care need to be taken in order to obtain accurate models: inaccurate models would obviously yield misleading results. Specifically, for the 3D models to be an accurate representation of tissue volumes some critical steps must be considered correctly. The tissue must be prepared (sectioned at a given thickness usually $3\text{--}10\ \mu\text{m}$, stained and imaged). Tissue preparation is challenging and leads to a dataset of two-dimensional (2D) stained histologic sections with imperfections. To mitigate these imperfections, several signal and image processing steps have to be considered. The contrast of all the sections must be the same, the sections must be precisely aligned (registered) and the sections lost during tissue sectioning must be interpolated. Finally, care must also be taken when each voxel of the 3D histologic volume is converted to an impedance value to yield the 3DZM. The 3D modeling strategies are dealt with in great detail in Chapter 3.

1.6 Ultrasonic Tissue Characterization

The motivation beyond the reconstruction of 3DZMs is that they are tremendous tools to help in the fundamental understanding of how ultrasound interacts with media of high complexity such as tissue. In particular, 3DZMs can be used to characterize tissue (i.e., obtain estimates of scatterer properties) independently of the ultrasonic backscattered measurements [21–26]. However, validity and accuracy of the 3DZMs are difficult to assess, but comparison of the ultrasonic characterization results with 3DZM characterization results can be a first test of the validity of the 3DZMs.

Another great application of the 3DZMs is that they can be used to devise realistic ultrasonic scattering models because 3DZMs are obtained from precise morphological descriptions of tissue. New scattering models can then be used with the ultrasonic backscattered measurements to obtain estimates that characterize tissue. The rationale is that these 3DZM-derived models are expected to accurately model tissue scattering. Thus, 3DZM-derived models should improve the accuracy of the structural descriptions. In particular, these models may lead to potentially improved

contrast in the reconstructed QUS images. Improved contrast may transcribe into improved detection (possibly early detection) and diagnosis of breast diseases.

Chapter 4 introduces the methodologies used for ultrasonic tissue characterization from the 3DZMs. Chapter 5 presents the results obtained by using these methodologies on simulated 3DZMs and histology-based 3DZM obtained from three animal models of human breast cancer. The three models chosen were a rat fibroadenoma, a mouse mammary carcinoma, and a mouse sarcoma. These models were chosen for their clearly distinct histopathologic features.

1.7 Noninvasive Diagnostic and Monitoring of Disease

The long-term goal of the research presented in this dissertation is the development of a new clinical ultrasonic imaging capability. This device would be in real-time capable of creating B-mode images supplemented by QUS information. The QUS information would be obtained from spectral analysis of the RF backscattered signals using advanced scattering models deduced from 3DZMs. The hope is that the displayed QUS information would be pathology-specific enough that it would allow physicians to distinguish clearly between diseased and healthy tissues, and also between different types of diseased tissues. If this ambitious goal were achieved, it would then be possible to confidently bypass biopsy and detect/diagnose/monitor several types of breast cancer in real time from noninvasive ultrasound scans. The future directions and the conclusions of the research are gathered in Chapter 6.

CHAPTER 2

ULTRASONIC SCATTERING THEORY

This chapter reviews the theories developed to study the scattering of sound waves by different structures. Faran's theory gives some exact solutions of the scattered field created by simple shapes. More general approaches are used to predict the scattered wave in a weakly scattering inhomogeneous medium. These theories naturally lead to the concept of the form factor (FF) to model ultrasonic scattering. FFs are frequency-dependent functions that contain information to predict the scattered wave behavior in an inhomogeneous medium.

2.1 Sound Scattering by Uniform Spheres and Cylinders

The Faran theory gives closed-form solutions for the scattered pressure radiated by a uniform sphere or a uniform cylinder [27] from an incident plane wave, $p_{inc} = P_0 \exp(-ikx)$. The time-harmonic dependent term, $\exp(i\omega t)$, is assumed and thus is omitted. The propagating medium has a speed of sound, c , a density, ρ , and a wavenumber, $k = \frac{\omega}{c}$. The equations in the original Faran paper [27] contained a few typos that were later corrected by Hickling [28].

Faran's equations are obtained by first expressing the incident and the scattered pressure waves by the appropriate cylindrical or spherical wave decomposition. In particular, the coefficients of the scattered wave decomposition are the unknowns. To determine these coefficients, three boundary conditions are applied at the surface of the scatterer. First, the pressure in the fluid must be equal to the normal stress in the solid. Second, the normal displacement must be continuous at the interface. Third, there can be no tangential stress at the surface of the scatterer. The closed-form solutions are briefly introduced below.

2.1.1 Faran's theory for a solid cylinder

A solid cylinder of radius a (infinite in the z -direction) is considered. The solid cylinder supports shear waves (with speed c_2 and corresponding wavenumber k_2) and

compressional waves (with speed c_1 and corresponding wavenumber k_1) and has a density ρ_1 .

The scattered pressure can be written as a cylindrical wave decomposition:

$$p_{sca} = \sum_{m=0}^{\infty} A_m \cos(m\theta) [J_m(kr) + iN_m(kr)] \quad (2.1)$$

where θ and r are the cylindrical coordinates, and J_m and N_m are the cylindrical Bessel function of the first and second kind, respectively. The A s are the unknown decomposition coefficients which are given by:

$$A_m = -\varepsilon_m P_0 i^{m+1} e^{-i\gamma_m} \sin(\gamma_m), \quad (2.2)$$

where

$$\tan \gamma_m = \tan \delta_m(ka) \frac{\tan \Phi_m + \tan \alpha_m(ka)}{\tan \Phi_m + \tan \beta_m(ka)}, \quad (2.3)$$

$$\epsilon_m = \begin{cases} 1 & \text{if } m = 0 \\ 2 & \text{if } m \geq 2 \end{cases}, \quad (2.4)$$

and

$$\tan(\delta_m(ka)) = -\frac{J_m(ka)}{N_m(ka)} \quad (2.5)$$

$$\tan(\alpha_m(ka)) = -ka \frac{J'_m(ka)}{J_m(ka)} \quad (2.6)$$

$$\tan(\beta_m(ka)) = -ka \frac{N'_m(ka)}{N_m(ka)} \quad (2.7)$$

$$\tan(\Phi_m) = (-\rho/\rho_1) \tan(\xi_m(k_1 a, \sigma)), \quad (2.8)$$

with

$$\tan(\xi_m(k_1 a, \sigma)) = \frac{-(k_2 a)^2}{2} \frac{\frac{k_1 a J'_m(k_1 a)}{k_1 a J'_m(k_1 a) - J_m(k_1 a)} - \frac{2m^2 J_m(k_2 a)}{m^2 J_m(k_2 a) - k_2 a J'_m(k_2 a) + (k_2 a)^2 J''_m(k_2 a)}}{\frac{\frac{\sigma}{1-2\sigma}(k_1 a)^2 [J_m(k_1 a) - J''_m(k_1 a)]}{k_1 a J'_m(k_1 a) - J_m(k_1 a)} + \frac{2m^2 [k_2 a J'_m(k_2 a) - J_m(k_2 a)]}{m^2 J_m(k_2 a) - k_2 a J'_m(k_2 a) + (k_2 a)^2 J''_m(k_2 a)}} \quad (2.9)$$

where σ is the Poisson's ratio of the cylinder. This last equation is written as a function of k_1 , a , and σ , because the compressional speed, the shear speed, and the Poisson's ratio are related by the following equation:

$$\sigma = \frac{1}{2} \left[\frac{c_1^2 - 2c_2^2}{c_1^2 - c_2^2} \right], \quad (2.10)$$

which allows for the elimination of the c_2 dependency from the equations. This equation demonstrates that when $c_2 \rightarrow 0$ (i.e., there are no shear waves) the Poisson's ratio converges to $\frac{1}{2}$.

2.1.2 Faran's theory for solid sphere

For the case of a solid sphere of radius a , and using the same notation for the sphere's properties as for the cylinder's, similar equations are derived. For symmetry reasons, equations make use of the spherical Bessel functions of the first and second kind j_m and n_m . The scattered pressure is expressed by a spherical wave decomposition:

$$p_{sca} = -P_0 \sum_{m=0}^{\infty} (2m+1) i^m e^{-i\gamma_m} \sin \delta_m P_m(\cos \theta) [j_m(kr) + i n_m(kr)], \quad (2.11)$$

where P_m is the Legendre function of the first kind,

$$\tan \gamma_m = \tan \delta_m(ka) \frac{\tan \Phi_m + \tan \alpha_m(ka)}{\tan \Phi_m + \tan \beta_m(ka)} \quad (2.12)$$

and

$$\tan(\delta_m(ka)) = -\frac{j_m(ka)}{n_m(ka)} \quad (2.13)$$

$$\tan(\alpha_m(ka)) = -ka \frac{j'_m(ka)}{j_m(ka)} \quad (2.14)$$

$$\tan(\beta_m(ka)) = -ka \frac{n'_m(ka)}{n_m(ka)} \quad (2.15)$$

$$\tan(\Phi_m) = (-\rho/\rho_1) \tan(\xi_m(k_1 a, \sigma)) \quad (2.16)$$

where

$$\tan(\xi_m(k_1 a, \sigma)) = \frac{-(k_2 a)^2}{2} \frac{\frac{k_1 a j'_m(k_1 a)}{k_1 a j'_m(k_1 a) - j_m(k_1 a)} - \frac{2(m^2+m) j_m(k_2 a)}{(m^2+m-2) j_m(k_2 a) + (k_2 a)^2 j''_m(k_2 a)}}{\frac{\frac{\sigma}{1-2\sigma}(k_1 a)^2 [j_m(k_1 a) - j''_m(k_1 a)]}{k_1 a j'_m(k_1 a) - j_m(k_1 a)} + \frac{2(m^2+m)[k_2 a j'_m(k_2 a) - j_m(k_2 a)]}{(m^2+m-2) j_m(k_2 a) + (k_2 a)^2 j''_m(k_2 a)}} \quad (2.17)$$

and σ is Poisson's ratio of the sphere.

2.1.3 Faran's theory and biological materials

The formula presented above and derived by Faran [27] allow for good comparison with scattering from tissues, because some of the tissue constituents can be seen in a first approximation as spheres or cylinder. However, going beyond these simple

models is necessary, and therefore a better understanding of the interactions between ultrasonic waves and tissue microstructure is needed. Nevertheless, the pioneering formulas of Faran have been compared to many scattering models [7].

Also, the formulas take into account the possible existence of shear waves. Another model that was developed by Anderson [29] describes the scattering from a fluid sphere (i.e., no shear waves). The Anderson model was developed slightly before Faran's theory and can be rederived from Faran's formula by letting Poisson's ratio approach $\frac{1}{2}$ (i.e., $\sigma \rightarrow \frac{1}{2}$ in Eq. (2.17))

2.2 Weak Scattering in an Inhomogeneous Medium

The theory of scattering of a propagating acoustic wave in a heterogeneous medium is reviewed in this section [30]. Weak scattering is the case where the inhomogeneities that cause scattering have tissue property values (density, ρ , and compressibility, κ) very close to those of the rest of the medium. For an incident plane wave of unit amplitude, in the case of the Born approximation (multiple scattering is ignored), the backscattered pressure wave far from the interrogated (or scattering) volume is a spherical wave:

$$p_{bs} = \frac{e^{-ikr}}{r} \Phi(2k), \quad (2.18)$$

where bs denotes backscattered, k is the propagation constant ($k = \omega/c$ where ω is the angular frequency and c is the propagation speed), and the angle distribution function $\Phi(2k)$ is

$$\Phi(2k) = \frac{k^2}{4\pi} \iiint_{V_0} \gamma(r_0) e^{-2ikr_0} dv_0. \quad (2.19)$$

V_0 represents the scattering volume, and the function $\gamma(r)$ is

$$\gamma(r) = \gamma_\kappa(r) - \gamma_\rho(r) \quad (2.20)$$

where

$$\gamma_\kappa(r) = \frac{\kappa(r) - \kappa_0}{\kappa_0} \quad (2.21)$$

and

$$\gamma_\rho(r) = \frac{\rho(r) - \rho_0}{\rho(r)}, \quad (2.22)$$

where $\rho(r)$ and $\kappa(r)$ are the density and compressibility of the scattering sites, and ρ_0 and κ_0 are the density and the compressibility of the material surrounding the scattering sites, respectively. The functions $\gamma_\kappa(r)$ and $\gamma_\rho(r)$ are therefore the relative changes in compressibility and density in the scattering volume V_0 , respectively.

The backscattered intensity is hence

$$I_{bs} = Ak^4|\Phi(2k)|^2, \quad (2.23)$$

where A is a proportionality constant.

In the case of weak scattering, that is, when γ_κ and γ_ρ are very small (for example < 0.1 for this first order Taylor series approximation to be accurate), the function $\gamma(r)$ approximates to [19]

$$\gamma(r) = -2\frac{z(r) - z_0}{z(r)} = -2\frac{\Delta z}{z}, \quad (2.24)$$

where z is the plane wave impedance $z = \rho c = \sqrt{\rho/\kappa}$, $z(r)$ is the characteristic acoustic impedance value at location r and z_0 is the background impedance, that is, the impedance of the medium with no scatterers. Thus, the function $\gamma(r)$ is proportional to the relative change in the characteristic acoustic impedance.

Combining Eqs. (2.19), (2.23), and (2.24) yields

$$I_{bs} = A'k^4S(2k) \quad (2.25)$$

where

$$S(2k) = \left| \frac{\iiint_{V_0} \frac{\Delta z}{z} e^{-2ikr_0} dv_0}{\iiint_{V_0} \frac{\Delta z}{z} dv_0} \right|^2 = \frac{S'(2k)}{S'(0)}, \quad (2.26)$$

A' is a new proportionality constant, and $S(2k)$ is normalized such that $S(0) = 1$

The backscattered intensity divided by k^4 is proportional to the magnitude squared of the Fourier transform of the relative impedance function, which is equal to the Fourier transform of the SAF of the relative impedance function of the scattering volume [31]. $S'(2k)$ and $S(2k)$, defined by Eq. (2.26), are termed *power spectrum* and *normalized power spectrum* of the medium, respectively.

2.3 Form Factor

FFs are functions that describe the amplitude of the backscattered intensity due to a single scattering structure or to an ensemble as a function of frequency, or more

commonly as a function of the wave vector amplitude k . The FFs are based on 3D spatial correlation models by assuming some form or shape for the scattering tissue structures. Usually simple scattering shapes are assumed, and in most cases they have a spherical symmetry. Mathematically, FFs are related to the shape of the scatterer through the Fourier transform. Specifically, the FF is the Fourier transform of the 3D SAF of a 3D medium containing a single scatterer, that is, the magnitude squared of the Fourier transform of the single scatterer's shape. FFs are normalized to a value of 1 when $k = 0$ and their derivative usually vanishes when $k = 0$ [19]. They are therefore readily comparable to the normalized power spectrum $S(2k)$ (Eq. (2.26)).

2.3.1 Usual form factors

Commonly used FFs include the Gaussian, the fluid sphere, and the spherical shell. They all describe spherically symmetric scatterers and depend only on the radius a of the scattering structure. For the fluid sphere FF the scatterer is assumed to be a homogeneous sphere filled with a fluid. For the spherical shell FF the scatterer is assumed to be a solid shell, and therefore, no wave is propagated inside the sphere. The Gaussian FF is a continuous distribution with spherical symmetry of relative impedance between the scatterer and the surrounding medium. The common FF definitions are [7, 19]

$$F_a^1(2k) = e^{-0.827k^2a_{eff}^2} \quad (\text{Gaussian}), \quad (2.27)$$

$$F_a^2(2k) = \left[\frac{j_1(2ka)}{\frac{2}{3}ka} \right]^2 \quad (\text{fluid sphere}), \quad (2.28)$$

$$F_a^3(2k) = [j_0(2ka)]^2 \quad (\text{spherical shell}). \quad (2.29)$$

The subscript eff in Eq. (2.27) denotes *effective* because the radius does not correspond to a sharp discontinuity for a continuous distribution; a_{eff} is related to the correlation distance d by $d = (3\sqrt{\frac{\pi}{2}})^{\frac{1}{3}}a_{eff} = 1.55a_{eff}$ [19]. The subscript eff is omitted in the remainder of the dissertation. Also, the term “scatterer size” will always refer to the diameter of the scatterer (i.e., $2a$ or $2a_{eff}$ for the Gaussian model). The terms j_0 and j_1 are the spherical Bessel function of the first kind of order 0 and 1, respectively.

Figure 2.1 shows plots of the Gaussian, fluid-filled sphere, and the spherical shell form factors (all figures and tables appear in the last section of each chapter). The Gaussian and the fluid-filled sphere FF are almost identical up to a value of $ka = 1$. Above $ka = 1$ the fluid-filled sphere FF curve has a steeper slope than the Gaussian

FF curve. The spherical shell FF is the FF with the steepest slope over the range $0 \leq ka \leq 1.5$. The spherical shell FF vanishes around $ka = 1.5$ and then slightly increases to reach a local maximum near $ka = 2.3$. Figure 2.1 clearly demonstrates that the common FFs are different and that will logically lead to different results when used to model ultrasonic scattering.

The Gaussian FF (Eq. (2.27)) has often been used to model scattering from soft tissues [9, 23, 32]. The Gaussian FF allows for efficient estimation schemes to be utilized when estimating scatterer properties (i.e., the scatterer size and acoustic concentration). Goodness-of-fit has been used to determine the best model for describing scattering; however, the anatomical scattering sources are still undetermined. There may exist undiscovered FFs that better model scattering than those FFs commonly used.

2.3.2 Anisotropic FF

The usual FFs introduced in Section 2.3.1 are all modeling spherical (or isotropic) scatterers. Equivalently, the FF depends only on the magnitude $k = \sqrt{k_x^2 + k_y^2 + k_z^2}$ of the 3D frequency variable of the 3D Fourier transform. These FFs can be easily extended to nonisotropic models.

Specifically, nothing prevents the use of a 3D FF to model tissue microstructure that would be nonisotropic. An example could be to choose a 3D Gaussian FF that modeled “ellipsoidal” scatterers:

$$F_{a,b,c}(k_x, k_y, k_z) = e^{-0.827[k_x^2 a^2 + k_y^2 b^2 + k_z^2 c^2]}, \quad (2.30)$$

where a , b , and c are the effective radii in the three directions, and k_x , k_y , and k_z are the three frequency variables of the 3D Fourier transform. Equation (2.30) can hence be used to model a scatterer that would be ellipsoidal in shape. Furthermore, Eq. (2.30) can be extended to model cylindrical scatterers by for example letting $a = b$ while $c \rightarrow \infty$.

The above 3D Gaussian FF was introduced to give an example of a nonisotropic FF. It would also be possible to derive a formula similar to Eq. (2.30) for the case of a 3D ellipsoidal shell FF or of a 3D fluid-filled ellipse FF. Obviously, nonisotropic FF can be readily used to model ultrasonic scattering from nonisotropic tissue structures. Therefore, nonisotropic models constitute a valuable extension of the common isotropic models.

Anisotropic FFs were used to model and characterize tissue for which the scattering sources were believed to not be isotropic. For example, the ultrasonic scattering from renal parenchyma was hypothesized to be due to cylindrical structures called *nephrons* [33]. To test this hypothesis this study used cylindrical FFs. Cylindrical FFs are independent of k_z and function of $k = \sqrt{k_x^2 + k_y^2}$ and $\phi = \arctan\left[\frac{k_y}{k_x}\right]$ only.

2.3.3 Form factor from Faran's theory

Faran's theory yields the scattered pressure by a uniform sphere or cylinder. The backscattered far-field pressure can be computed and used to derive a theoretical FF from Faran's theory for any material. Specifically, to obtain the FF, the backscattered intensity is obtained from the backscattered pressure for a finite-size scatterer and then divided by the limit of the same quantity when $ka \rightarrow 0$ [7]. $ka \rightarrow 0$ leads to the long-wavelength (or small scatterer) limit case and therefore the backscattered intensity converges to that of a Rayleigh scatterer [30]. Thus, potentially Faran's theory can be used to describe any FF of any material that would have a simple shape such as a sphere or a cylinder.

However, not only is it obvious that many tissue constituents cannot be approximated by such simple shapes as a sphere or a cylinder, but moreover Faran's theory needs values for the density, speed of sound, and Poisson's ratio. Such values are not available for most tissue constituents. Finally, even if the values were known and the shape simple (i.e., sphere or cylinder), computation of the Faran's theory FF is fairly involved as shown by the equations of Section 2.1.1. In particular, these equations involve infinite series that need to be truncated with care. Computation is also quite extensive when compared to the time it would take to compute the Gaussian FF, Eq. (2.27), for example.

Figure 2.2 displays two Faran-derived FFs for a glass sphere and a fat sphere. The spheres were considered to be buried in a medium for which the speed of sound was 1540 m/s and the density was 1000 kg/m³. The speeds of sound were taken to be 5570 m/s (glass) and 1460 m/s (fat). The densities were taken to be 2300 kg/m³ (glass) and 940 kg/m³ (fat), and the Poisson's ratios were taken to be 0.21 (glass) and 0.4993 (fat). These values were compiled from published measurements [34] and also were used by Insana et al. [7].

These density and speed of sound values indicate that glass is a strong scatterer (with respect to the background medium) whereas fat is a weak scatterer. Also, glass supports shear waves whereas the Poisson's ratio of fat is so close to 0.5 that shear waves only slightly contribute to the computed FF. The fact that the backscattered pressure amplitude would be much greater for the case of the scattering of a glass sphere when compared to that of the fat sphere can not be seen from the FF plots (Figure 2.2); this is due to the normalization when computing FF from Faran's theory [7, 27]. Figure 2.2 shows that the fat sphere FF is slowly decreasing and has a zero near $ka = 2.2$, while the glass sphere FF has a steeper decrease but does not vanish over the ka -range ($0 \leq ka \leq 3$).

Furthermore, Insana et al. have compared common FFs (Eqs. (2.27)-(2.29)) with the results of the Faran theory for spheres [7]. Their results have shown variable agreement between closed-form results and the common FFs for different types of spherical scatterers. The variability is extremely dependent upon the acoustical properties of the considered spherical scattering structure. Form factor models do not take into account the presence of shear waves in the scatterers, whereas the theory of Faran incorporates shear.

2.3.4 Derivation of an advanced form factor

This section describes how it is possible to obtain theoretical FFs that describe more advanced scattering models than the common models proposed in Section 2.3.1. The theoretical approach is fairly general and can be applied to model numerous possible scatterers. It is applied here to derive the theoretical FF that would have a population of Gaussian scatterers with a Gaussian distribution of size of mean a and standard deviation σ . Let's denote this FF by $F_{a,\sigma}^{GG}(2k)$ where the superscript reminds the Gaussian-Gaussian aspect of the distribution.

The theoretical FF is deduced by computing the volume-weighted average of the Gaussian FF over the Gaussian distribution of size:

$$F_{a,\sigma}^{GG}(2k) = \frac{1}{A} \int_{-\infty}^{\infty} \left[\frac{4}{3}\pi x^3 \right]^2 F_x^1(2k) \frac{e^{-\frac{1}{2}\left(\frac{x-a}{\sigma}\right)^2}}{\sqrt{2\pi\sigma^2}} dx, \quad (2.31)$$

where the first term inside of the integral accounts for the fact that the contribution of each scatterer to the power spectrum is proportional to the square of the (effective) volume of the Gaussian spheres. The second term, the Gaussian FF, accounts for the spectral (scattering) properties of each Gaussian scatterer. The last term within

the integral is the probability distribution of a Gaussian random variable of mean a and standard deviation σ . Finally, A is a normalization constant chosen such that $F_{a,\sigma}^{GG}(0) = 1$ and is equal to

$$A = \int_{-\infty}^{\infty} \left[\frac{4}{3} \pi x^3 \right]^2 \frac{e^{-\frac{1}{2}(\frac{x-a}{\sigma})^2}}{\sqrt{2\pi\sigma^2}} dx. \quad (2.32)$$

In particular Eq. (2.31) shows that the derivative of $F_{a,\sigma}^{GG}$ is vanishing at $k = 0$.

The integrals in Eqs. (2.31) and (2.32) were written to include nonrealistic negative radii because doing so allows for closed-form integration of Eq. (2.31). The negative part of the integral is negligible for all practical cases because the Gaussian size distribution is centered around a .

Equations (2.31) and (2.32) can be very simply adapted to model other scatterers following other size distribution. First, the form factor within the integral can be changed to virtually any other FF and second, the size probability distribution can be changed to follow any other distribution. Once more, this Gaussian-Gaussian example is meant to illustrate the methodology and leads to closed-form evaluation of Eqs. (2.31) and (2.32).

Details of the integration are given in Appendix B and yield:

$$F_{a,\sigma}^{GG}(2k) = \frac{1}{A} \frac{e^{\frac{C^2}{4B(k)}}}{B^{3.5}(k)} \left[\frac{C^6}{4B^3(k)} + \frac{15C^4}{2B^2(k)} + \frac{45C^2}{B(k)} + 120 \right], \quad (2.33)$$

where the normalization constant A , the frequency-dependent term $B(k)$, and the constant C are given by:

$$A = 16\sqrt{2}\sigma^7 e^{\frac{a^2}{2\sigma^2}} \left[\frac{a^6}{\sigma^6} + \frac{15a^4}{\sigma^4} + \frac{45a^2}{\sigma^2} + 60 \right], \quad (2.34)$$

$$B(k) = 0.827k^2 + \frac{1}{2\sigma^2}, \quad (2.35)$$

$$C = \frac{a}{\sigma^2}. \quad (2.36)$$

Equation (2.33) shows that the resulting expression is fairly involved, but at least there exists a closed-form expression. In particular, it takes some effort to prove that if $\sigma \rightarrow 0$ then $F_{a,\sigma}^{GG}(2k) \rightarrow F_a^1(2k) = e^{-0.827k^2a^2}$. Figure 2.3 displays three Gaussian-Gaussian FFs; the regular Gaussian FF with $a = 16 \mu\text{m}$ (and $\sigma = 0$), the Gaussian-Gaussian FF for which $a = 16 \mu\text{m}$ and $\sigma = 4 \mu\text{m}$ and the Gaussian-Gaussian FF for which $a = 16 \mu\text{m}$ and $\sigma = 12 \mu\text{m}$. From these plots, as the standard deviation increases, so does the slope of the corresponding Gaussian-Gaussian FF.

Figure 2.3 also demonstrates how a Gaussian-Gaussian FF for which $\sigma > 0$ may be very different from the regular Gaussian FF thus leading to different results when used to model ultrasonic scattering.

Structures in tissue have varying sizes; thus extending the usual FFs by including a size distribution is valuable to model tissue scattering more accurately. The Gaussian-Gaussian FF presented in this section describes a Gaussian distribution of sizes of Gaussian scatterers. However, so structures in tissue exist that would have a continuous and smooth change in impedance value. Thus, the Gaussian FF may already be understood to include the effect of a size distribution for scattering structures that would have abrupt change in impedance. Therefore, the Gaussian-Gaussian FF is more a theoretical tool than a realistic physical model because it can be interpreted as taking into account a size distribution twice.

2.4 Scattering Structures and FF

FFs are related to tissue microstructure through the Fourier transform. If a very accurate FF were known, the inverse Fourier transform would yield information regarding the anatomic microstructures responsible for ultrasonic scattering. The difficult part is to obtain an accurate FF.

The work presented in this dissertation will introduce methodologies to extract FFs directly from tissue morphology. Specifically, 3D tissue models will be obtained from optical micrographs of consecutive tissue sections. Methodologies will be introduced to reconstruct these 3D tissue models and use them to characterize tissue scattering properties.

2.5 Figures

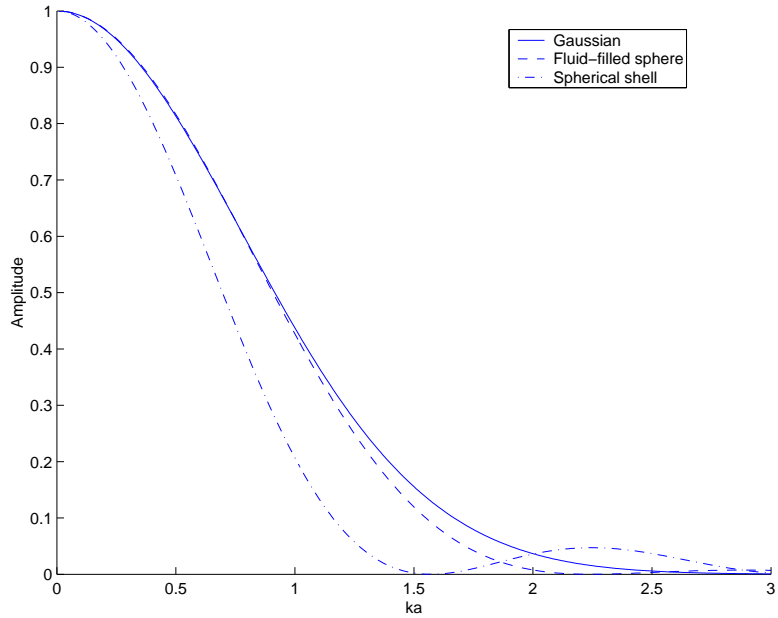


Figure 2.1 Plots of the Gaussian, the fluid-filled sphere, and the spherical shell form factors. The plots are displayed as a function of ka over the range $0 \leq ka \leq 3$.

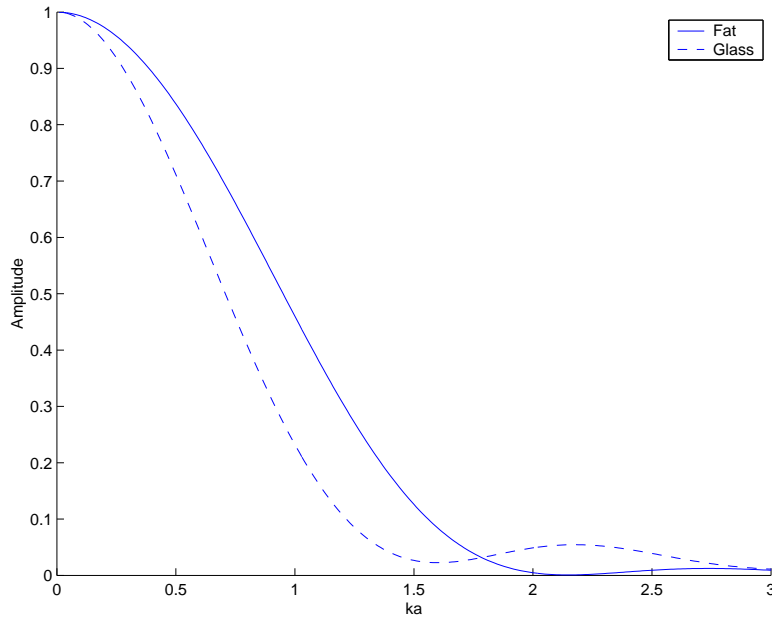


Figure 2.2 Plots of two form factors derived from Faran's theory: fat sphere and glass sphere. The plots are displayed as a function of ka over the range $0 \leq ka \leq 3$.

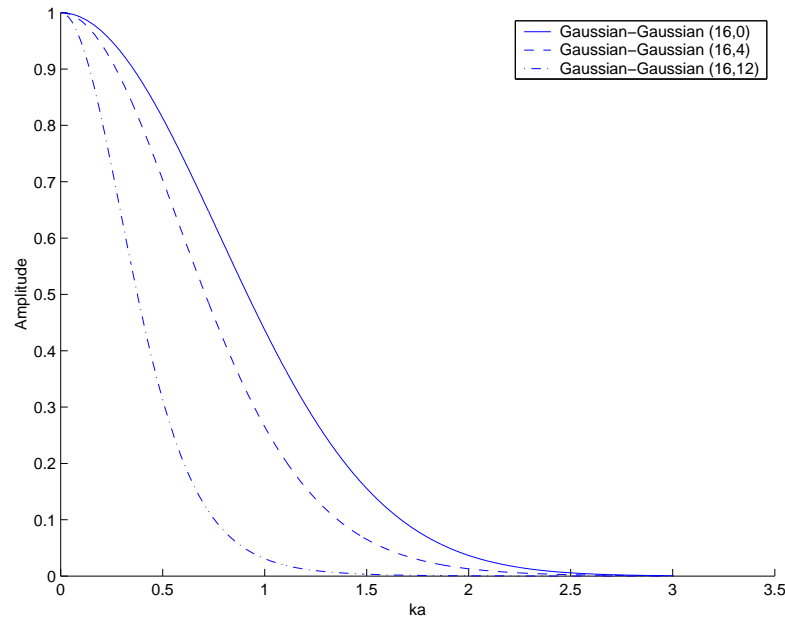


Figure 2.3 Plots of three Gaussian-Gaussian form factors. The plots are displayed as a function of ka over the range $0 \leq ka \leq 3.5$. The numbers between parentheses are the value used for a and σ in Eq. (2.33) in micrometer.

CHAPTER 3

THREE-DIMENSIONAL MODELING METHODOLOGIES

This chapter presents a set of signal and image processing strategies to reconstruct a 3DZM from consecutive 2D histologic tissue sections. The strategies are illustrated using the 200-section histologic dataset of a mouse sarcoma. Hematoxyn and eosin (H&E) stained sections are imaged using optical microscopy. Typical histologic datasets have problems that need to be addressed in order to obtain accurate 3D representations. In particular, consecutive histologic sections may have different contrasts (they acquire different amounts of stain) and their initial alignment is suboptimal. Furthermore, during the tissue sectioning process some of the sections are damaged and cannot be used.

3.1 Tissue Preparation

Three-dimensional reconstruction strategies are developed and demonstrated with a murine sarcoma tumor model. The EHS (Englebreth-Holm-Swarm) tumor (ATCC - CRL-2108, American Type Culture Collection) is a transplantable sarcoma in C57BL/6 mice. This tumor grows subcutaneously and produces extracellular matrix (ECM) components such as laminin, collagen IV, entactin, and heparan sulfate proteoglycan. The EHS stock was thawed, resuspended in culture media (Ham's F12K medium), gently pelleted by centrifugation, resuspended in a small volume of culture media, and injected subcutaneously into a mouse. The tumor was allowed to grow until it was of sufficient size for harvesting. At this point, the mouse was euthanized by cervical dislocation under anesthesia and the tumor dissected free from the subcutaneous tissue. It was placed in culture media and was processed under aseptic conditions. The tumor was minced with a scalpel blade into small pieces and then passed under pressure through a series of hypodermic needles of decreasing luminal diameters to reduce the size of the tissue components. When the material freely passed through an 18-gauge hypodermic needle, it was suspended in culture

media, washed by gentle agitation, gently pelleted by centrifugation, resuspended in a small volume of culture media, and injected subcutaneously into 10 mice. Nine of these mice were then used for studies; one was used to pass the tumor as described above into an additional 10 mice. This process was repeated as needed to maintain the transplantable sarcoma for these studies.

Sections of the EHS sarcoma were fixed by immersion in 10% neutral-buffered formalin, embedded in paraffin, sectioned at 3- μm thickness, mounted on glass slides, and stained with H&E for evaluation.

The processes of fixation, paraffin infiltration, and sectioning of the EHS sarcoma for histopathologic evaluation causes a minor degree of inherent tissue shrinkage that is small, but indeterminate for each section. In addition, it is not possible to obtain 200 serial sections (one section after another) without the loss of some sections in the series due to technical difficulties in tissue sectioning.

EHS sarcoma sections, mounted on glass slides, were examined and captured using a Nikon Optophot-2 light microscope equipped with a Sony color video camera. Each image was manually registered with the preceding image by a board-certified pathologist via a microscope stage that was rotated in x and y planes such that three readily identifiable microstructures in the image were visually aligned with the same three microstructures of the preceding tissue section. This process was repeated for all sections in the series. Digital images were stored as bitmap images for additional analysis. The manual registration process is labor-intensive and imprecise; therefore, an automatized registration algorithm was developed.

For the EHS dataset, the optical images measured laterally 400 μm by 300 μm . The EHS dataset contained 200 sections of which 54 sections (27%) were lost during tissue preparation. Each bitmap image measured 640 pixels by 480 pixels with 8-bit accuracy for each red, green and blue (RGB) component.

3.2 Three-Dimensional Reconstruction

The 3D reconstruction of a tissue volume from 2D sections involves several signal and image processing steps. First, the contrast of the sections was equalized because the uptake of stain, in general, was not uniform; nor was the video capture intensity necessarily the same from section to section. Next, a fine-tuning registration was conducted. Finally, for the missing sections, interpolation was performed.

3.2.1 Contrast Adjustment

Consecutive histologic sections generally have different contrasts. Each section may have been stained for a slightly different duration or may have a slightly different thickness or both. These differences result in variability of stain uptake. Image contrast was equalized prior to registration in order to increase the robustness of the registration algorithm. Equalization was conducted for each of the three color components (i.e., red, green and blue (RGB)) of each image.

Specifically, let H_c^I denote the cumulative histogram of image I (for one of the color components). Thus, $H_c^I(\alpha)$ is the number of pixels with intensity level $\leq \alpha$ in the image (α is assumed to be an integer in the range 0–255 because of the 8-bit accuracy for each color component). Then, if $I(i, j)$ represents the intensity level of pixel (i, j) in image I , the new pixel intensity in the equalized image I' at (i, j) is given by [35]:

$$I'(i, j) = 255 \frac{H_c^I(I(i, j))}{N}, \quad (3.1)$$

or equivalently the equalizing transform is given by:

$$\alpha' = 255 \frac{H_c^I(\alpha)}{N}, \quad (3.2)$$

where N is the total number of pixels in the image and the factor 255 has been added so that the new pixel intensity is in the range 0–255 (because $0 \leq H_c^I/N \leq 1$). Thus, α' is the new intensity value for each of the pixels that had an intensity value of α . During processing, it was not necessary to round Eq. (3.2) to the nearest integer. However, if the equalized sections were saved into a 24-bit bitmap, Eq. (3.2) needed to be rounded because of the 8-bit accuracy in each color component.

Figure 3.1(a) shows the original histogram (red color component) of section 1 of the EHS dataset. The great majority (>90%) of the pixel intensities were in the range 120–205. This is typical of an image that is neither dark nor bright and has a poor contrast. A dark image would, for example, have most of its pixel intensities in the range 0–127, while a bright image would have its pixel intensities in the range 128–255. An image with good contrast would ideally show a histogram spreading the range 0–255.

Figure 3.1(b) shows the equalized histogram. The entire 0–255 pixel intensity range was utilized, even though the equalized histogram contained only 55 distinct

intensity levels, whereas the original histogram contained 199 distinct intensity levels. The decrease in the number of distinct intensity levels was due to the fact that the digitized image was a discrete 2D signal whose intensity levels were also discrete (i.e., integers of the range 0–255). This is also why the equalized histogram was not perfectly flat. The new histogram was much flatter than the original (Figure 3.1(a)). The improvement can be quantified by evaluating the kurtosis of the image histograms before and after equalization. The kurtosis was reduced from 4.26 to 1.79 after equalization. The reduced kurtosis demonstrates that the histogram of the equalized image is flatter than that of the original image. Furthermore, the value 1.79 is approximately equal to the theoretical kurtosis value, $\frac{9}{5}$, of a uniform distribution [36].

Figure 3.1(c) displays the equalization transform that has been deduced from Eq. (3.2). This transform is a scaled version of the cumulative histogram of the original image; it is therefore a nondecreasing transform. The flat part of the transform (intensity range 0–89) means that any pixel with intensity level less than 89 in the original image will be transformed to a pixel with 0 intensity level in the equalized image. Similarly, the flat part over 206–255 indicates that any pixel with intensity level greater than 206 will be transformed to a pixel with intensity 255 in the equalized image.

Figure 3.2(a) shows the original image (section 1 of the EHS dataset) while Figure 3.2(b) shows the same image after histogram equalization for the three color components. It is visually obvious that the equalized image has the better contrast. The contrast difference between the dark and bright structures is much greater in Figure 3.2(b) than in Figure 3.2(a). For example, the white space in the lower middle (lumen of a blood vessel) and upper left to middle (artifactual separation of connective tissue planes due to processing) is much brighter in the equalized image. In addition, the light pink circular structure (muscle) in the middle of Figure 3.2(a) has become purple in Figure 3.2(b).

3.2.2 Registration

Registration or alignment is an essential step in the 3D reconstruction of the tissue model from serially sectioned photomicrographs. If the consecutive sections are not aligned correctly, then the resulting 3D model yields misleading or incorrect results that lead to potentially serious artifacts.

Many image registration techniques exist for medical images [37]. For our 3D

modeling, each section needs to be aligned with the next. Specifically, we are trying to determine the best transformation to apply to an image I_2 so that it is the most similar to the original and adjacent image I_1 . Hence, the registration algorithm is composed of three main parts: set of transformations, similarity measure and optimization.

Set of transformations The goal of this part of the registration algorithm is to transform I_2 using a transformation T so that $T(I_2)$ is as similar as possible to I_1 . It is necessary to define which types of transforms T can be used. This set, S , usually falls into two main categories, rigid and nonrigid transformations [38–40]. The rigid transformation set, S_r , is composed of rotations and translations (it has three degrees of freedom (DOFs), two translational and one rotational). The nonrigid transformation set S_{nr} is composed of just about any conceivable adjustable parameter. In the present work S_r was used as it is a reasonable choice considering the error sources in the initial manual alignment of the images. However, a subset of S_{nr} limited to the affine transformations (S_{af}) was also considered because this class of transforms can compensate for the unknown inherent tissue shrinkage that occurs during tissue preparation.

Specifically, if $T \in S_r$ then the new coordinate (x', y') of a pixel (x, y) can be defined according to the matrix equation:

$$\begin{pmatrix} x' \\ y' \\ 1 \end{pmatrix} = \begin{pmatrix} \cos(\theta) & \sin(\theta) & T_x \\ -\sin(\theta) & \cos(\theta) & T_y \\ 0 & 0 & 1 \end{pmatrix} \begin{pmatrix} x \\ y \\ 1 \end{pmatrix}. \quad (3.3)$$

Equation (3.3) describes a rigid transformation with three DOFs that consists of a rotation (of angle θ) and a translation vector $\begin{pmatrix} T_x \\ T_y \end{pmatrix}$. Figure 3.3 illustrates how an image is modified under a rigid transformation. The original Cartesian grid (Figure 3.3(a)) is transformed to a new grid (Figure 3.3(b)) by a rigid transformation for which $\theta = -5^\circ$, $T_x = -15$ pixels and $T_y = 25$ pixels. Figure 3.3 shows that a rigid transform conserves angles and distances (i.e., the squares were transformed to squares of the same size).

A similar decomposition is available for $T \in S_{af}$:

$$\begin{pmatrix} x' \\ y' \\ 1 \end{pmatrix} = \begin{pmatrix} \Gamma & T_x \\ 0 & 1 \end{pmatrix} \begin{pmatrix} x \\ y \\ 1 \end{pmatrix}, \quad (3.4)$$

where

$$\Gamma = \begin{pmatrix} \cos(\theta) & \sin(\theta) \\ -\sin(\theta) & \cos(\theta) \end{pmatrix} \begin{pmatrix} S_x & 0 \\ 0 & S_y \end{pmatrix} \begin{pmatrix} 1 & \beta \\ 0 & 1 \end{pmatrix}. \quad (3.5)$$

T is decomposed into a rotation (of angle θ), a scaling along both axis (defined by S_x and S_y), an x -shear (defined by β), and a translation vector $\begin{pmatrix} T_x \\ T_y \end{pmatrix}$. For an affine transformation to be invertible one needs to enforce $S_x S_y \neq 0$. Basically, an affine transformation is the composition of a translation with any invertible linear transformation. Therefore, S_{af} is the set of all the transforms that conserves parallelism. It is also important to notice that a rigid transform is an affine transform for which $S_x = 1$, $S_y = 1$ and $\beta = 0$. Figure 3.4 illustrates how an image is modified under an affine transformation. The original Cartesian grid (Figure 3.4(a)) is transformed to a new grid (Figure 3.4(b)) by an affine transformation for which $\theta = -6^\circ$, $S_x = 1.1$, $S_y = 0.9$, $\beta = 0.2$, $T_x = 20$, and $T_y = -10$ pixels. Figure 3.4 shows that an affine transform respects parallelism but not angles or distances (or areas).

When the pathologist performs an initial manual registration, it is a rigid registration; i.e., only rotation or translation or both are performed. Therefore, when rigid registration is considered herein, it is a fine-tuning registration. In particular, the same image could have been obtained by optical microscopy if the sections were perfectly aligned. On the other hand, affine transforms include DOFs (stretching and shearing) that are not available to the pathologist when aligning adjacent sections.

Similarity measure Once the image I_2 is transformed it is necessary to quantify how $T(I_2)$ is similar to I_1 . Let us define $F(I, J)$ as a function that quantifies the similarity between image I and image J . Many choices are possible for F [40, 41]. For example, the root mean squared of the image difference (RMSD) $|I - J|$ or the correlation between I and J are standard similarity measures. However, the functions F based on information theory concepts (entropy) are usually very robust [42, 43]. This trend was also observed in the present study. Therefore, the normalized mutual information

(NMI), based on entropy concepts, was used as a similarity measure [37, 38, 44]. RMSD, correlation and NMI values between image 1 and an affine-transformed version of image 2 of the EHS dataset were computed for a complete range of transform parameters. The best RMSD, correlation, and NMI values occurred for the same values of the six DOFs. However, the NMI showed a much sharper maximum (after normalization) than the other two measures (Figure 3.5). The sharper maximum demonstrated that the NMI measure was more robust because it would be easier to find the optimal transform.

The rationale behind using information theory concepts for registration is that when images are registered the new information contained in the second image should be minimum relative to the original image. This abstract idea of “information” is formalized in the concept of entropy.

For a gray-level image I , its probability distribution, p_I , is defined as the normalized histogram of I . Specifically, $p_I(i)$ is equal to the number of pixels with intensity level i in image I divided by the total number of pixels in I . The notation $H(I)$ will be used to denote the entropy of an image I using the above definition for the underlying probability distribution of the image. $H(I)$ is defined by

$$H(I) = - \sum_i p_I(i) \log [p_I(i)]. \quad (3.6)$$

Given two images, the joint probability distribution of images I and J (I and J are assumed to have the same dimensions), $p_{I,J}(i,j)$, is equal to the number of pixels that have intensity level i in I and j in J divided by the total number of pixels of image I (or J).

The joint entropy of images I and J is defined by

$$H(I, J) = - \sum_{i,j} p_{I,J}(i,j) \log[p_{I,J}(i,j)], \quad (3.7)$$

and the normalized mutual information (NMI) by [37, 38, 44]

$$NMI(I, J) = \frac{H(I) + H(J)}{H(I, J)} = 1 + \frac{MI(I, J)}{H(I, J)}. \quad (3.8)$$

Equation (3.8) gives the definition of the mutual information (MI) that can also be used as a similarity measure but has been shown to be less robust than NMI [37, 38, 43].

The images are assumed to be aligned when the NMI value is maximum. In other words, the images are aligned when the amount of information they contain about

each other is maximum. In the present work, the NMI was evaluated on intensity (gray-level) images deduced from the color images by averaging the color components. However, the resulting gray-scale image was coded using 24 bits per pixels.

Optimization The next step is to update the transform ($T \rightarrow T'$) so that $F(I_1, T'(I_2)) \geq F(I_1, T(I_2))$, where T and T' belong to the set of transforms. Many algorithms (e.g., gradient, Newton's method, Levenberg-Marquardt method) rely on the possibility of evaluating or easily estimating the gradient or the Hessian of the similarity function (with respect to the transformation's DOFs) or both. These techniques are not readily applicable to the NMI measure, even though expressions exist for the gradient of the MI [45].

Popular algorithms that bypass the need for derivatives are Powell's algorithm and the simplex method. Powell's algorithm optimizes each of the transformation's DOFs one by one [46, 47]. The simplex method considers all DOFs simultaneously. The latter was used in the present work [48]. Briefly, an initial simplex is composed of $N_{DOF} + 1$ points in the function's DOFs space, where N_{DOF} is the goal function's number of DOFs (Figure 3.6). Then, the value of the goal function is evaluated at each of the points in the simplex. The point that yields the least value is replaced by its image with respect to the hyperplane generated by the other N_{DOF} points of the simplex. This process leads to a new simplex and the algorithm keeps updating the simplex until convergence is achieved. The algorithm includes strategies for reducing the size of the simplex (i.e., an optimal point can be found within a prescribed precision) and for avoiding the generation of the same simplex more than once (i.e., guaranteed convergence).

For these iterative algorithms the starting point was critical because the NMI function may have had several local minima at which the optimization algorithm could become trapped. Therefore, a random starting point was used because no prior information was known about how two consecutive sections were misaligned. Specifically, the NMI was computed for 1024 random transforms for rigid registration and 2048 for affine registration. The transform that yielded the largest NMI value was used as a starting point for the simplex optimization routine. More random trials were necessary for affine registration because of the greater DOFs.

3.2.3 Interpolation

Interpolation was necessary for two different steps of the 3D reconstruction: registration and missing sections.

Registration interpolation When an image was transformed, there was a high probability that the new grid did not line up with a Cartesian grid (Figures 3.3(b) and 3.4(b)). Therefore, an interpolation was needed so that the transformed image match the Cartesian grid for computer implementation. During registration optimization, a relatively basic 2D interpolation algorithm was used. The algorithm should be fast because many interpolations were required for the optimization procedure. For that reason, nearest neighbor interpolation was used to interpolate the transformed images on a Cartesian grid during registration. However, once the best transform was found, a more accurate 2D interpolation algorithm was used for reconstruction. Even though computationally slower, it needed to be applied only once and led to images of better quality. A bicubic interpolation algorithm was used for the reconstruction of the registered sections. Bicubic interpolation uses a third-order interpolation polynomial as kernel. A new pixel was obtained from the 16 pixels in the nearest 4 by 4 neighborhood of the pixel in the original image. The third-order cubic kernel is given by [49]:

$$g(s) = \begin{cases} \frac{3}{2}|s|^3 - \frac{5}{2}|s|^2 + 1 & \text{if } |s| \leq 1 \\ -\frac{1}{2}|s|^3 + \frac{5}{2}|s|^2 - 4|s| + 2 & \text{if } 1 < |s| \leq 2 \\ 0 & \text{if } |s| > 2 \end{cases} . \quad (3.9)$$

Specifically, a continuous image (I_{cont}) was reconstructed from the discrete image (I) using:

$$I_{cont}(x, y) = \sum_{i,j} I(i, j)g(x - i)g(y - j), \quad (3.10)$$

where (x, y) symbolizes the new continuous variables of the reconstructed continuous image, while (i, j) symbolizes the samples of the discrete image. Then, the transformed image was obtained by sampling $T(I_{cont})$ on a regular grid. The same process was used for nearest-neighbor interpolation where g was replaced by the zeroth order polynomial kernel:

$$g_{nearest}(s) = \begin{cases} 1 & \text{if } |s| \leq \frac{1}{2} \\ 0 & \text{if } |s| > \frac{1}{2} \end{cases} . \quad (3.11)$$

Figure 3.7 displays the nearest-neighbor, cubic and sinc kernels over the range -3.5 – 3.5 for s . The sinc kernel is the ideal reconstruction kernel (for bandlimited signals) [31]. Specifically, if the original continuous signal has been sampled above the Nyquist frequency, then using the sinc kernel instead of g in Eq. (3.10) leads to the exact original continuous signal. However, its infinite support makes it unusable for implementation. The nearest-neighbor kernel is not a good approximation for the ideal sinc kernel whereas the cubic kernel, Eq. (3.9), follows the sinc kernel more accurately over the range $-1 \leq s \leq 1$. The discrepancies observed for $|s| > 1$ between the sinc and the cubic kernels indicated that even though better than the nearest-neighbor kernel, the cubic kernel is far from being an ideal kernel. Figure 3.7 also indicates that all the kernels are unity when $s = 0$ and vanish when s is equal to any other integer. This property is necessary and sufficient for $I_{cont}(i, j) = I(i, j)$, i.e., the reconstructed continuous image passes through every sample of the discrete image.

Missing section interpolation When tissue is sectioned, some sections are lost or destroyed. Therefore, it is necessary to interpolate the missing sections to avoid further artifacts in the 3D tissue model. A 3D interpolation algorithm was developed to interpolate the missing sections. Interpolating missing sections was different from interpolating transformed images, because for the case of the missing sections, fewer points were needed to be interpolated.

To interpolate the missing voxels, cubic Hermite polynomials were used. Specifically, the 3D interpolation was first reduced to several one-dimensional (1D) interpolations by considering the 1D signal formed by following the intensity at the same pixel location from one section to the next (and for each of the three color bands). Thus, this 1D signal was regularly sampled but had missing samples. Let's denote $f_{(i,j)}^\kappa(k)$ as this 1D signal, where the subscript denotes the location of the pixel in every section indexed by k . The exponent κ takes value 1, 2, or 3 which designs the red, green, or blue color components, respectively.

Assuming that there were missing data between sections k_1 and k_2 , (i.e., $f_{(i,j)}^\kappa(k_1)$ and $f_{(i,j)}^\kappa(k_2)$ were available but $f_{(i,j)}^\kappa(k)$ for $k_1 < k < k_2$ needed to be interpolated), then the Hermite interpolation searches for a third-order polynomial, $P(k)$, (i.e., four

unknowns) so that the following four equations were satisfied:

$$P(k_1) = f_{(i,j)}^\kappa(k_1) \quad (3.12)$$

$$P(k_2) = f_{(i,j)}^\kappa(k_2) \quad (3.13)$$

$$P'(k_1) = f_{(i,j)}^\kappa(k_1) \quad (3.14)$$

$$P'(k_2) = f_{(i,j)}^\kappa(k_2). \quad (3.15)$$

To solve these equations, it was necessary to estimate the derivatives of the discrete signal $f_{(i,j)}^\kappa$ with respect to k (in Eqs. (3.14) and (3.15)). A common method to estimate the derivative of $f_{(i,j)}^\kappa(k_1)$ is by computing the slope between $f_{(i,j)}^\kappa(k_1)$ and the closest available $f_{(i,j)}^\kappa$ value. From the above equations, it was clear that the Hermite interpolation led to continuous signals with continuous derivatives.

Figure 3.8 illustrates the Hermite interpolation methodology. It shows a 57-sample signal with 16 missing samples (including four consecutively), its continuous reconstruction from Hermite interpolation and finally its reconstructed samples. The Hermite-reconstructed signal passed through all the available samples which was a desired property. Also, the signal appeared to be constant (equal to one) over the range 0–10 (i.e., the eleven first samples) where 3 samples were missing. Further, the Hermite-reconstructed signal was strictly constant over the range 0–10, in particular there were no oscillations between the samples.

Figure 3.8 illustrates two properties of the Hermite reconstruction methodology. The Hermite-reconstructed signal was *shape-preserving* and *monotonicity-preserving*. On intervals where the available samples were monotonic, the Hermite-reconstructed signal was also. At a point where the available signal had a local extremum, the Hermite-reconstructed signal did too. For example, samples 11 and 49 were local minima of the available signal, and the reconstructed signal also had local minima at these points. Further, the available signal was decreasing over the range 16–23, as was the reconstructed signal.

The fact that the Hermite reconstruction scheme preserved extrema has the advantage that it also preserved the range of the signal. This fact was of particular interest when dealing with images, because it guarantees that the reconstructed signals will still be in the range 0–255, thus avoiding the need for postprocessing to compress values into the range 0–255.

The final step was to recompose the missing sections by gathering the information from the three 1D interpolations (for each color) for each pixel of each missing

section. Specifically, the missing section k_0 was reconstructed from the set $\{f_{(i,j)}^\kappa(k_0), \text{for } \kappa \in \{1, 2, 3\} \text{ and for every } (i, j)\}$.

3.2.4 Assignment of acoustic impedance values

To convert each pixel value to an appropriate acoustic impedance value a color-threshold algorithm was used on every H&E stained bitmap image (after reconstruction). The range of colors of the different structures in the bitmap images were recorded. Each structure was assigned an impedance value (Table 3.1). The histology images represent a 2D matrix with colors represented by three 8-bit values corresponding to red, green and blue. The ranges of color values corresponding to the different structures were used to project the bitmap into a 2-D matrix where certain color ranges, corresponding to identified structures, were given the value corresponding to its assigned impedance value from the table.

Tissue proteins stained with eosin have shades of color ranging from very light pink to dark pink, depending on the concentration of protein within the structure. This differential staining allowed for the recognition of unique microstructures in the tissue. A range of colors corresponding to an identified microstructure in the stained bitmap images was then assigned a single color. The new single color was thus representative of the acoustic impedance for that tissue microstructure.

For each pixel of the same color in the color-thresholded bitmap image the same acoustic impedance value was assigned. Figure 3.9 shows an example of an original H&E stained photomicrograph of a tissue section and the color-thresholded bitmap from a EHS mouse sarcoma.

Three different mammary tumors were used in our analysis. The impedance values used for the different tissue microstructures contained into the tissue were somewhat empirical, but also based on a large body of measured data [50–52]. For most soft tissues, the propagation speeds and densities fall within a relatively narrow range (speeds: 1520-1580 m/s; densities: 980-1010 kg/m³; impedances: 1.5-1.6 Mrayl), with whole blood (speed: 1580 m/s; density: 1040 kg/m³; impedance: 1.6 Mrayl) at the high end of most soft tissues. For lipid-based tissues, both the speed and density are somewhat lower (speeds: 1400-1500 m/s; densities: 920-970 kg/m³; impedances: 1.3-1.5 Mrayl). For the collagen-based tissues, both the speed and density are somewhat greater than most soft tissues (speeds: 1600-1700 m/s;

densities: 1020-1100 kg/m³; impedances: 1.6-1.9 Mrayl).

3.2.5 Three-dimensional renderings

The 3D renderings presented in this dissertation were generated from the reconstructed sections by the software package Amira 3.1.1 (Mercury Computer Systems, Berlin, Germany, www.amiravis.com).

3.3 Validation of the Methodologies

3.3.1 Registration algorithms

The rigid and affine registration algorithms were exercised using 160 cases for which the optimal transforms were known. Specifically, the first section of the EHS dataset was used as the first image. The second image was generated from the first section by applying a rigid or an affine transform selected randomly. Contrast was also randomly altered. The transformed images were interpolated using the cubic interpolation methodology. The ranges of the transformation parameters are reported in the first two rows of Table 3.2, and were chosen to extend beyond those expected from the histologic datasets.

The registration process was repeated 160 times (80 rigid and 80 affine transforms) leading to four sets of error statistics. Mean errors (\pm standard deviations) were computed for these four cases (Table 3.3). The first row of Table 3.3 indicates that rigid registration performed well when the optimal transform was rigid. The mean translation errors were less than two pixels and the mean rotation error was less than 0.05°. The second row indicates that the affine registration algorithm was capable of accurate tracking when the transformation was rigid. The accuracy is manifested by the small errors obtained in S_x , S_y and β . Furthermore, the mean errors in translation (<2 pixels) and rotation (<0.05°) were similar to those of the first row. Because the rigid transforms are a subset of the affine transforms, the NMI value could not decrease when going from rigid to affine registration. However, the NMI value slightly increased from 1.441 to 1.443. It is normal not to expect a significant increase in the NMI value because the optimal transform is rigid.

The rigid registration algorithm performed poorly when the optimal transform was affine (third row, Table 3.3) because the rigid registration algorithm could not track the shearing and stretching alterations. In particular, the NMI value of 1.039

was much lower than that of the other rows. Also, the mean translation errors were greater than 3 pixels and the mean rotation error was greater than 2.5° . The last row indicates that the affine registration performed accurately when the optimal transform was affine. The mean errors were in the same range as the first two rows. The mean translational errors were near 2 pixels and the mean rotational error was less than 0.1° . The NMI value of 1.428 was slightly smaller than those of the first two rows (1.441 and 1.443, respectively). An affine transformation produces greater alteration in the transformed image than a rigid transform would because of the additional DOFs for shearing and stretching. Thus, smaller NMI values were obtained because it was slightly more difficult to mitigate the affine transformation effects.

The small errors observed in the second and fourth row demonstrated that the affine registration algorithm performed well and independent of whether the optimal transform was rigid or affine. Thus, affine registration was used for the study.

3.3.2 Missing section interpolation

Evaluation of the interpolation strategy is necessary to appreciate the extent to which artifacts might occur in the reconstructed volume. Section 16 of the EHS dataset was missing and Hermite interpolation (after contrast equalization and registration) was used to reconstruct it (Figure 3.10). Even though the interpolated section looked very similar to sections 15 and 17 it was difficult to quantify the quality of the reconstructed missing section. The interpolated section showed some of the usual artifacts of interpolated signals, i.e., it was not as sharp as sections 15 and 17. The white structure at the bottom of the three images is more blurry in the interpolated section (Figure 3.10(b)). For a qualitative assessment, a board-certified pathologist examined the interpolated section under blinded conditions. The pathologist was able to recognize the histopathologic characteristics of the tissue that were diagnostically consistent with an EHS sarcoma such as the islands of tumor cells intermixed with ECM (right half of Figure 3.10(b)) without noting artifacts introduced by interpolation except for the blurriness.

3.3.3 Nine-section reconstruction

To validate the 3D reconstruction methodologies (Section 3.2), two 9-section datasets were designed. Each dataset was generated from the first section of the

EHS sarcoma dataset. For both datasets the fifth section was missing and the other seven sections were created by transforming the first section. The transformations of one of the nine-section datasets were confined to be rigid (Figure 3.11) and those of the other nine-section dataset were confined to be affine (Figure 3.12) (transformation parameter ranges: last two rows of Table 3.2). Contrast of each image was also randomly altered. The transformed images were interpolated using the cubic interpolation methodology.

Figure 3.13 shows the reconstructions for the rigid-transformed dataset (Figure 3.11). All of the sections visually appeared similar (even the Hermite-interpolated missing section 5). Figure 3.14 reconstructions for the affine-transformed dataset (Figure 3.12) showed equally satisfactory results. To quantify the reconstructed datasets, NMI values were computed (Figure 3.15).

Figure 3.15(a) shows the greatest NMI values obtained during registration optimization (i.e., using the nearest-neighbor kernel for interpolation) for both nine-section datasets (note: section 5 is missing so section 4 was registered with section 6). NMI values were fairly constant for both rigid- and affine-transformed datasets, within the narrow range of 1.41–1.45. The affine-transformed NMI values tended to be slightly smaller than the rigid-transformed NMI values because shearing and stretching led to artifacts that were more difficult to mitigate than just rotation and translations.

Figure 3.15(b) shows the NMI values from one section to the next after reconstruction (i.e., using cubic-kernel for transformation and Hermite-interpolation of missing sections). These values were all greater than the values shown in Figure 3.15(a), which was likely due to the interpolation kernel. During registration optimization the nearest-neighbor kernel, Eq. (3.11), was used, whereas for reconstruction the cubic kernel, Eq. (3.9), was used. Using the cubic kernel led to a reconstructed image of better quality from Eq. (3.10). Therefore, it is reasonable to expect greater NMI values after reconstruction. The two greatest NMI values for the rigid-transformed data points were for 4/5 and 5/6. The reason for this may be due to the Hermite interpolation scheme that made the reconstructed (interpolated) section 5 very similar to the adjacent sections. However, this was not observed in the affine data points that were fairly constant in the range 1.62–1.67.

Figure 3.15(c) shows the NMI values between section 1 and each section

after reconstruction to evaluate if there were a progressive alignment error of the consecutive reconstructed sections. A progressive misalignment would have been demonstrated by monotonically decreasing NMI values. There was no clear trend of decreasing values. The rigid-transformed NMI values oscillated in the range 1.58-1.68 except for 1/9. The value 1.44 for 1/9 was likely due to a slightly larger error in the registration of section 8 with 9 for which the rigid-transformed NMI value for 8/9, 1.53 in Figure 3.15(b), was also the smallest NMI value. The affine-transformed NMI values increased at first and then reached a plateau at 1.52 for 1/6. The above studies validated the overall 3D reconstruction scheme presented because these training/testing nine-section datasets contained all the artifacts that were expected to be contained in the histologic EHS dataset.

3.4 Sarcoma Acoustic Models

The 3D reconstruction strategies were then applied to the EHS dataset. Figure 3.16 shows 43 consecutive sections of the original EHS dataset. These sections were subimages of size $218 \mu\text{m}$ by $156 \mu\text{m}$ (i.e., 350 by 250 pixels) of the original $400 \mu\text{m}$ by $300 \mu\text{m}$ EHS images. Among these 43 consecutive sections, 7 were missing (including 4 consecutive sections). The sections were misaligned, and the contrast between sections was also slightly different. The misalignment can be observed by following the pink quasicircular structure (muscle) from one section to the next. In addition, sections 8 and 17 have slightly better contrast than the neighboring sections. In each section of the EHS dataset, the histopathologic characteristics of the tissue that are diagnostically consistent with an EHS sarcoma, (the islands of tumor cells intermixed with ECM) were clearly visible.

Figure 3.17 shows the reconstructed 43-section dataset. To align the images, affine registration was used. However, for each registration the best transform was found to be “quasi-rigid” in the sense that β was always smaller than $5 * 10^{-4}$ (i.e., there was no shearing), and S_x and S_y were always found to be in the range 0.95-1.05, (i.e., there was less than 5% stretching).

Figure 3.17 shows that all the reconstructed images had a very similar contrast. None of the sections visually stood out as clearly darker or lighter than the others. The sections were also aligned, as can be observed by following the oblique structures in the top left corner. The interpolated missing sections were of lower quality than

the others because the interpolated missing sections were not as sharp and contained some edge artifacts. This was particularly true for the four reconstructed images of the four consecutive missing sections. In particular, the purple background in the bottom-right corners of the interpolated images was not as uniform as in the other sections. The background appeared to be “noisy” and to contain random small structures with blurry edges. Except for the artifacts noted, in each section of the EHS dataset, the histopathologic characteristics of the tissue were diagnostically consistent with an EHS sarcoma.

Normalized mutual information values computed for the reconstructed 43-section dataset yielded much smaller values (Figure 3.18) than those obtained during training of the methodologies. Specifically, the majority of the NMI were near 1.03, which was much smaller than the values displayed on Figure 3.15 or Table 3.3 (second and fourth rows). The larger values obtained during validation of the methodologies are explained by the fact that all the training images were generated from section 1 of the EHS dataset. Thus, it is normal to expect larger NMI values when registering transformed versions of the same image than when registering different images. The outlier values in Figure 3.18 (for example, 15/16 and 16/17) occur for all the NMI values that involved Hermite-interpolated sections. For example, section 16 was missing and 15/16 and 16/17 values were about the same. Thus, the Hermite interpolation scheme made the sections artificially quite similar.

Figure 3.19(a) shows a 3D rendering from the 43-section reconstructed EHS dataset (Figure 3.17). The interpolated section artifacts were noticeable on the bottom half of the left side of the volume where the rendering was blurry. It also seems that the same section was repeated in this part of volume. This artifact was due to the Hermite interpolation that generated artificially quite similar images (Figure 3.18).

To obtain a 3DZM of the EHS sarcoma, seven distinct impedance values were used (right column of Table 3.1): 2.00 Mrayl for the nuclear heterochromatin (black on Figures 3.9 and 3.19(b)), 1.85 Mrayl for the nuclear euchromatin (blue), 1.70 and 1.65 Mrayl for the extracellular matrix (dark red/red), 1.60 for the vascular space/whole blood (white), and 1.58 and 1.55 for the cytoplasm (green/yellow).

3.5 Fibroadenoma and Carcinoma Acoustic Models

A 3DZM was also obtained for a rat fibroadenoma and a mouse carcinoma. However, reconstruction was simplified because the smaller number of sections (39 and 66 for the fibroadenoma and the carcinoma, respectively) allowed for accurate alignment by the pathologist.

For the rat fibroadenoma, each of the thirty-nine 10- μm -thick tissue sections measured laterally $800 \times 600 \mu\text{m}$. Each bitmap image measured 640 pixels by 480 pixels. Thus, each pixel represents a square of size $1.25 \times 1.25 \mu\text{m}$. Figure 3.20(a) shows the 3D H&E stained histologic map. For this tumor, three impedance values were used (left column of Table 3.1): 1.58 Mrayl (for the epithelial cells (in green in Figure 3.20(b))), 1.54 Mrayl for the mammary duct (in red) and 1.8 Mrayl for the connective tissue (background impedance, z_0 in blue).

For the mouse carcinoma [4T1 mouse mammary carcinoma, CRL-2539 American Type Culture Collection (ATCC, Manassas, VA)], each of the sixty-six 5- μm -thick tissue sections measured laterally $200 \times 150 \mu\text{m}$. Each bitmap image measured 640 pixels by 480 pixels. Thus, each pixel represents a square of size $0.31 \times 0.31 \mu\text{m}$. Figure 3.21(a) shows the 3D H&E stained histologic map. For this tumor four distinct impedance values were used (center column of Table 3.1): 1.45 Mrayl for the fat (white in Figure 3.21(b)), 1.58 Mrayl for the cytoplasm (gray), 1.60 Mrayl for the nuclei (blue), 1.60 Mrayl for the red blood cells (red) and 1.8 Mrayl for the connective tissue (green). Also, for this tumor the background impedance (z_0) was assumed to be 1.55 Mrayl.

3.6 Tables and Figures

Table 3.1 Impedance values (Mrayl) used for the 3D impedance maps.

Rat fibroadenoma	Mouse carcinoma	Mouse sarcoma
1.58 - epithelial cells	1.45 - fat	2.00 - nuclear heterochromatin
1.54 - mammary duct	1.58 - cytoplasm	1.85 - nuclear euchromatin
1.80 - connective tissue (z_0)	1.60 - nuclei 1.60 - red blood cells 1.80 - connective tissue 1.55 - background (z_0)	1.70/1.65(z_0) - extracell. matrix 1.60 - vascular space/blood 1.58/1.55 - cytoplasm

Table 3.2 Ranges of the parameters used to transform images and alter contrasts to exercise and validate registration and reconstruction strategies. Rigid transformations do not need values for S_x , S_y , and β as indicated by NA (not applicable). To alter contrast, all the pixel intensities were linearly compressed to the range C_{Min} – C_{Max} . All the parameters were random realizations of uniform distributions over the prescribed ranges. The first two rows show the ranges used to exercise the registration algorithms. The last two rows show the ranges used to exercise the overall reconstruction strategies. Ranges were chosen to extend beyond those expected from the histologic datasets.

Methodology	C_{Min}	C_{Max}	θ (degrees)	S_x	S_y	β	T_x (pixel)	T_y (pixel)
Rigid reg.	0–63	192–255	-16–16	NA	NA	NA	-60–60	-60–60
Affine reg.	0–63	192–255	-16–16	0.75–1.25	0.75–1.25	-0.25–0.25	-60–60	-60–60
Rigid recons.	0–63	192–255	-12–12	NA	NA	NA	-50–50	-50–50
Affine recons.	0–63	192–255	-12–12	0.80–1.20	0.80–1.20	-0.20–0.20	-50–50	-50–50

88

Table 3.3 Statistics of registration errors. Each row of statistics is computed from 80 registrations. The first column indicates which registration algorithm was used. The second column indicates the type of the optimal transform. The next six columns give the error statistics for each DOF of the transforms. Rigid registration does not yield values for S_x , S_y , and β as indicated by NA (not applicable). The last column displays the average of the greatest NMI obtained during registration optimization. Range of the DOFs of the random rigid and affine transforms are shown on the first and second row of Table 3.2, respectively.

Regis.	Trans.	θ (degrees)	S_x	S_y	β	T_x (pixel)	T_y (pixel)	NMI
Rigid	Rigid	0.0386 (\pm 0.16)	NA	NA	NA	1.44 (\pm 1.12)	1.41 (\pm 1.09)	1.441
Affine	Rigid	0.0414 (\pm 0.17)	$< 10^{-3}$	$< 10^{-3}$	$< 10^{-3}$	1.43 (\pm 1.11)	1.41 (\pm 1.09)	1.443
Rigid	Affine	2.72 (\pm 2.33)	NA	NA	NA	3.89 (\pm 3.76)	3.12 (\pm 2.78)	1.039
Affine	Affine	0.0652 (\pm 0.097)	$< 6.5 * 10^{-4}$	$< 4.5 * 10^{-4}$	$< 2 * 10^{-3}$	2.03 (\pm 1.34)	1.44 (\pm 1.12)	1.428

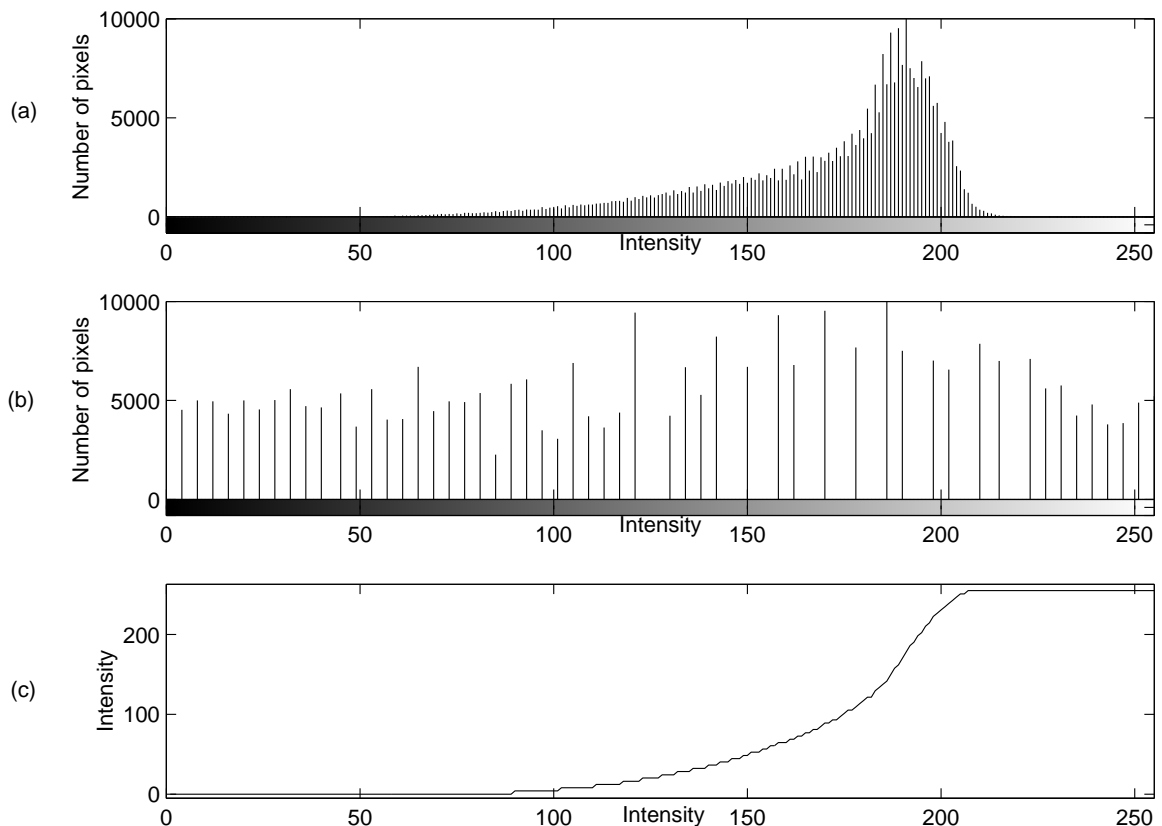


Figure 3.1 Illustration of contrast equalization. (a) Histogram of the red channel of original section 1 of the EHS dataset. (b) Equalized histogram of the red channel. (c) Equalization transform. Histogram kurtosis reduced from 4.26 before equalization to 1.79 after equalization.

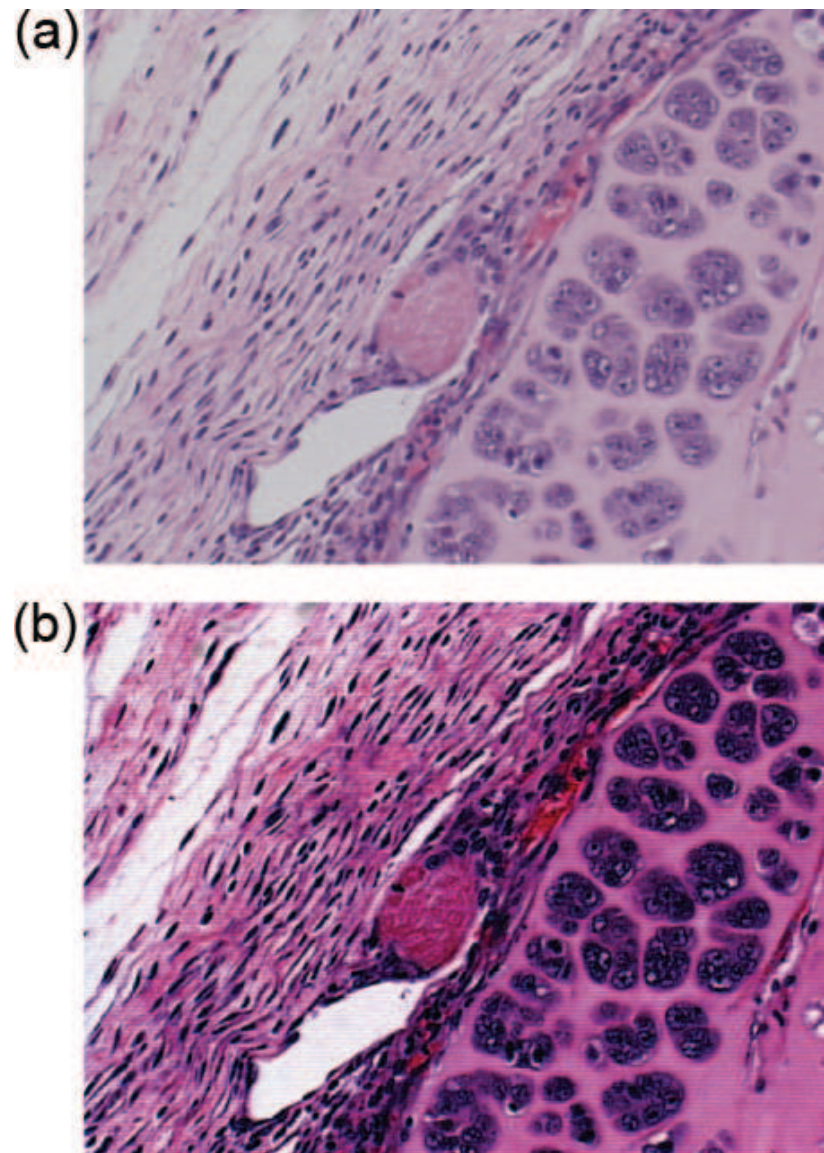
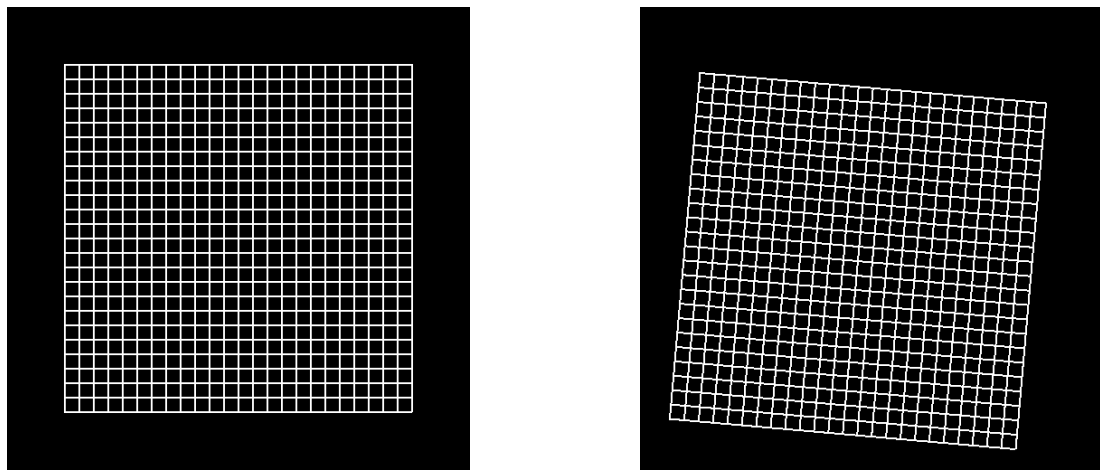


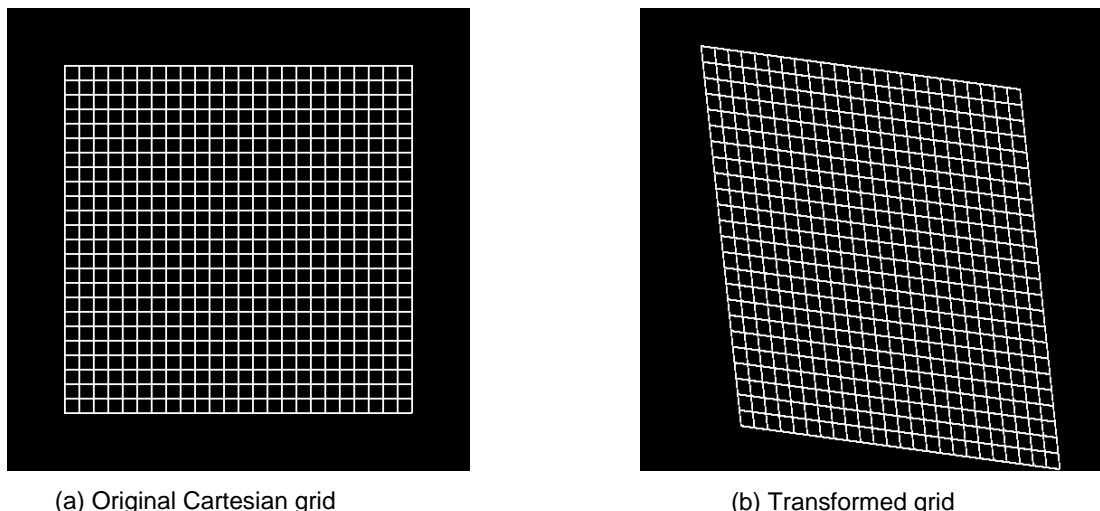
Figure 3.2 Illustration of contrast equalization. (a) Original section 1 of the EHS dataset. (b) Contrast-equalized section 1. Image (b) has a better contrast than image (a). For example, the white space in the lower middle (lumen of a blood vessel) is much brighter in (b) than in (a).



(a) Original Cartesian grid

(b) Transformed grid

Figure 3.3 Cartesian grid (a) transformed (b) by a rigid transformation for which $\theta = 5^\circ$, $T_x = -15$ pixels, and $T_y = 25$ pixels.



(a) Original Cartesian grid

(b) Transformed grid

Figure 3.4 Cartesian grid (a) transformed (b) by an affine transformation for which $\theta = -6^\circ$, $S_x = 1.1$, $S_y = 0.9$, $\beta = 0.2$, $T_x = 20$ pixels, and $T_y = -10$ pixels.

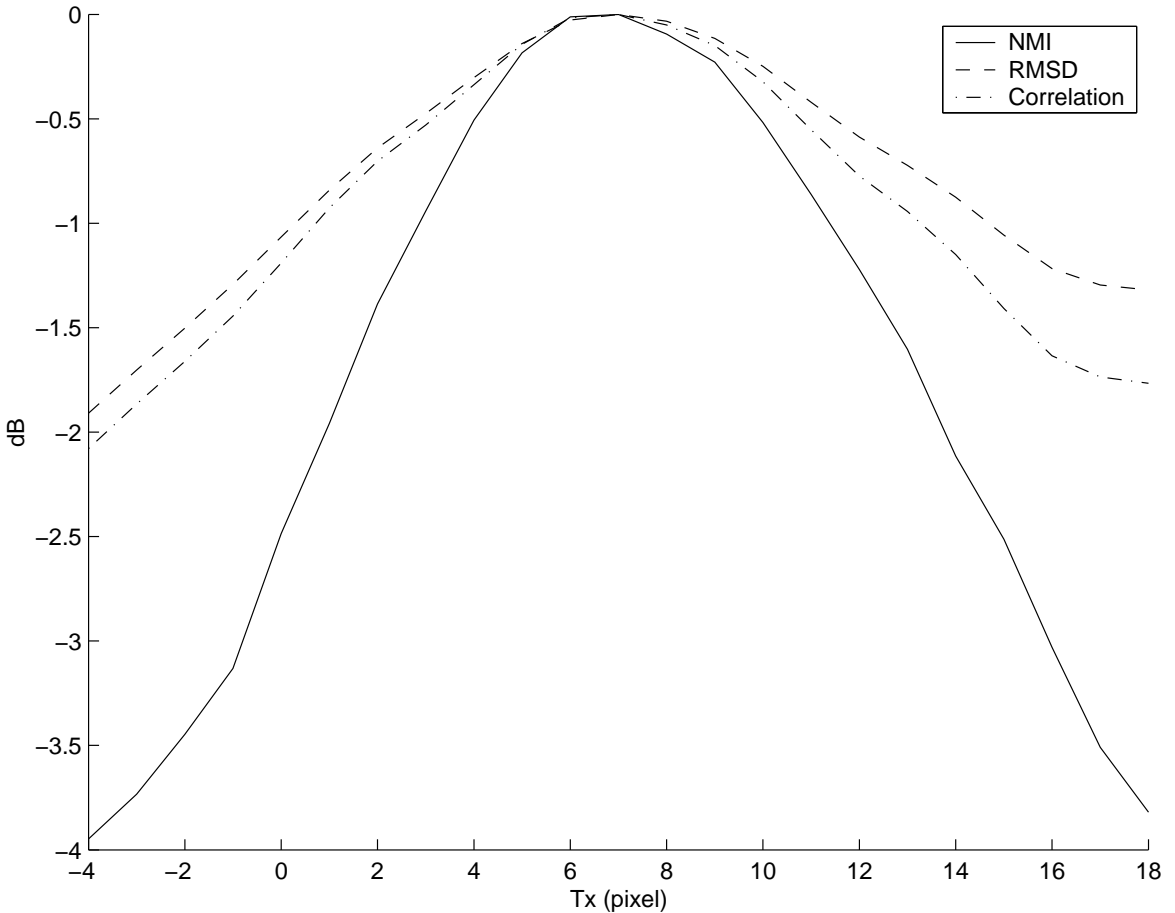


Figure 3.5 Illustration of the better performance of the NMI similarity measure compared to the root mean squared of the image difference (RMSD) and the correlation. Plots shows the normalized values in decibel (dB) of the three similarity measures evaluated using section 1 and an affine transformed version of section 2 of the EHS dataset. The values are displayed as a function of the affine transform DOF, T_x . The other five DOFs of the affine transforms were fixed at their optimal value (i.e., value leading to the best NMI, RMSD, and correlation). The NMI shows a sharper maximum (at $T_x=7$ pixels) than the other two measures.

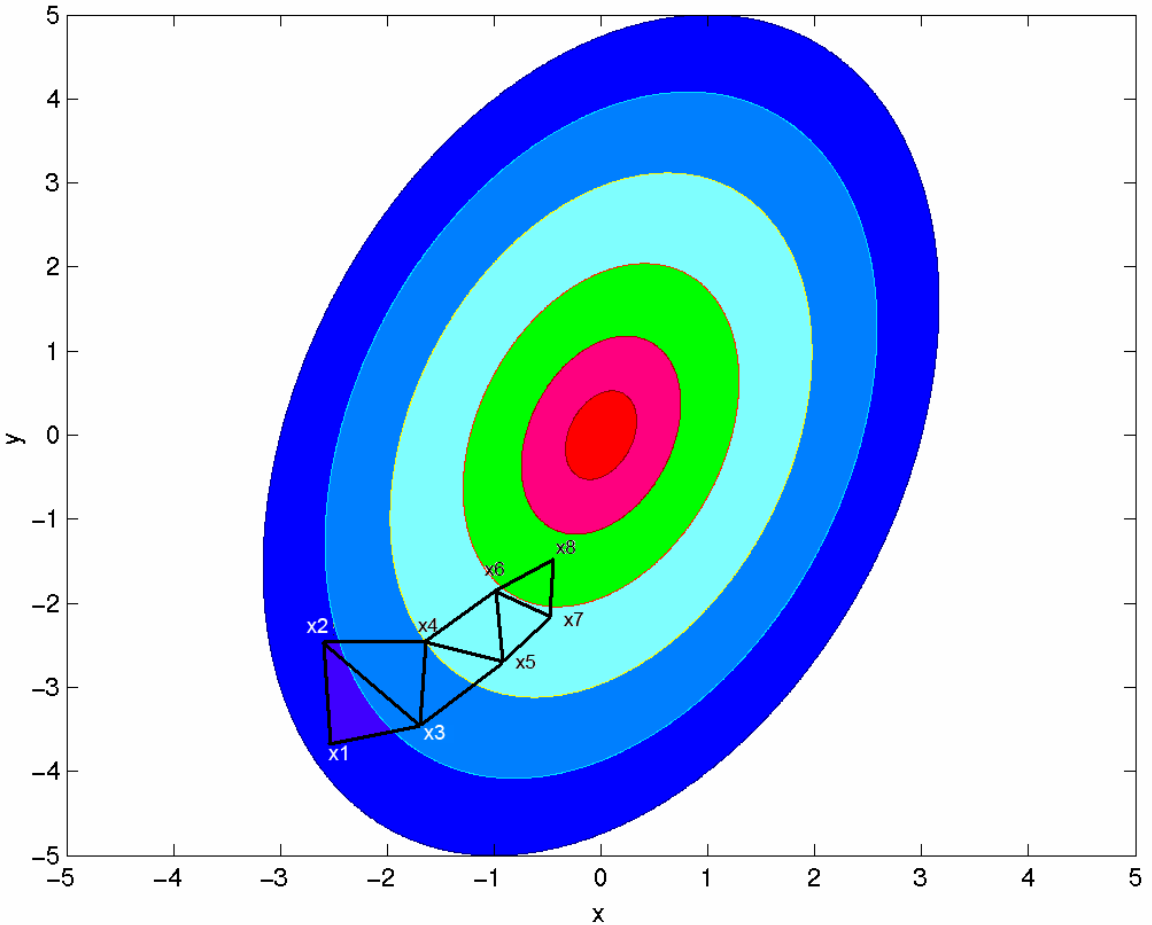


Figure 3.6 Illustration of the simplex optimization routine. The figure shows the contour plot of a function (f) of two variables (x and y). The maximum is at $x = 0$ and $y = 0$. The initial simplex is composed of $\{x_1, x_2, x_3\}$ and x_1 is replaced by x_4 because $f(x_1) < f(x_2)$ and $f(x_1) < f(x_3)$. The point x_4 is not exactly the image of the point x_1 with respect to the hyperplane x_2, x_3 because the simplex slightly compresses to enhance precision of the routine. The same process is repeated until convergence is reached.

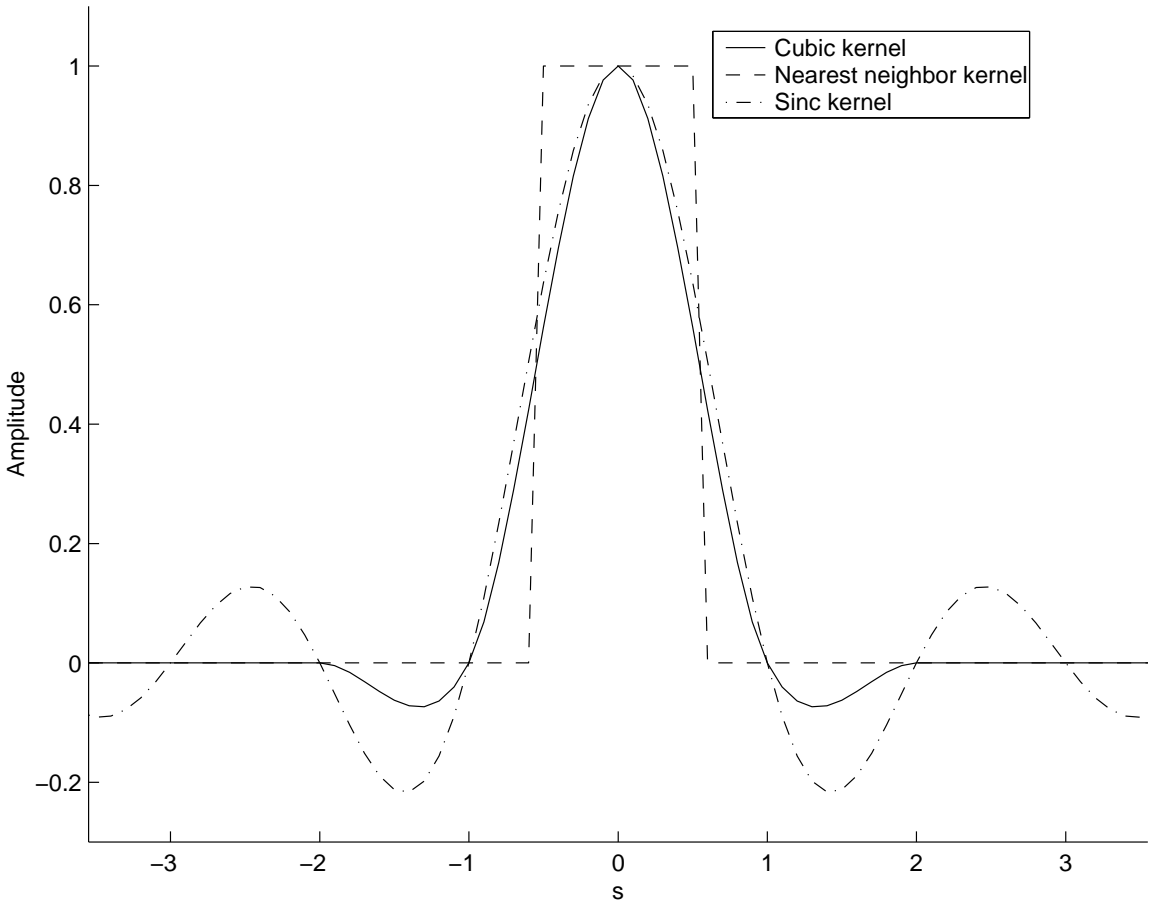


Figure 3.7 Interpolation kernels used during registration (nearest neighbor and cubic) and ideal sinc kernel over the range $-3.5 \leq s \leq 3.5$. Nearest-neighbor kernel is used during registration optimization. The cubic-kernel is used for reconstruction after the best transform has been found. The sinc kernel is the ideal kernel (i.e., leads to perfect reconstruction for bandlimited signals).

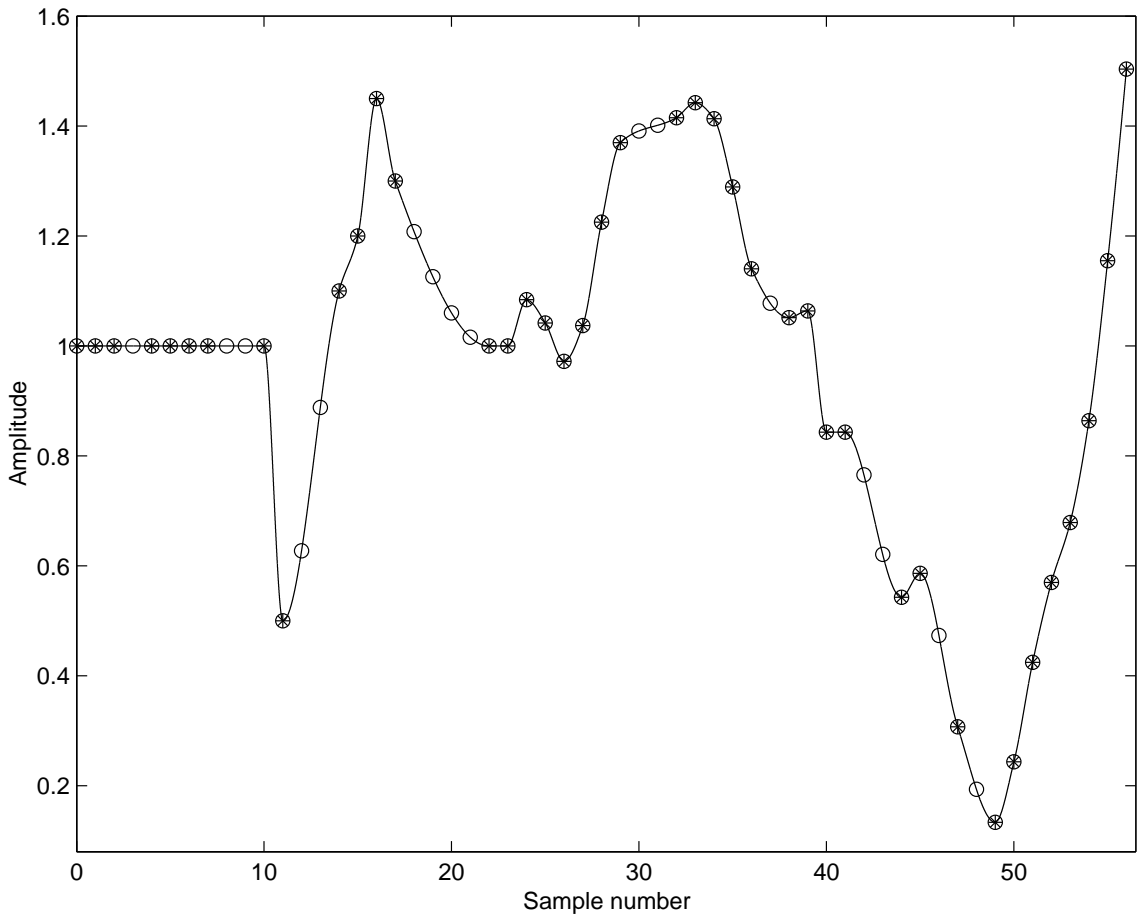


Figure 3.8 Illustration of the Hermite-interpolation methodology. The *'s represent the available samples, solid is the continuous Hermite reconstructed signal, circles are the interpolated missing values. Hermite-interpolation is used to generate the sections lost during tissue preparation.

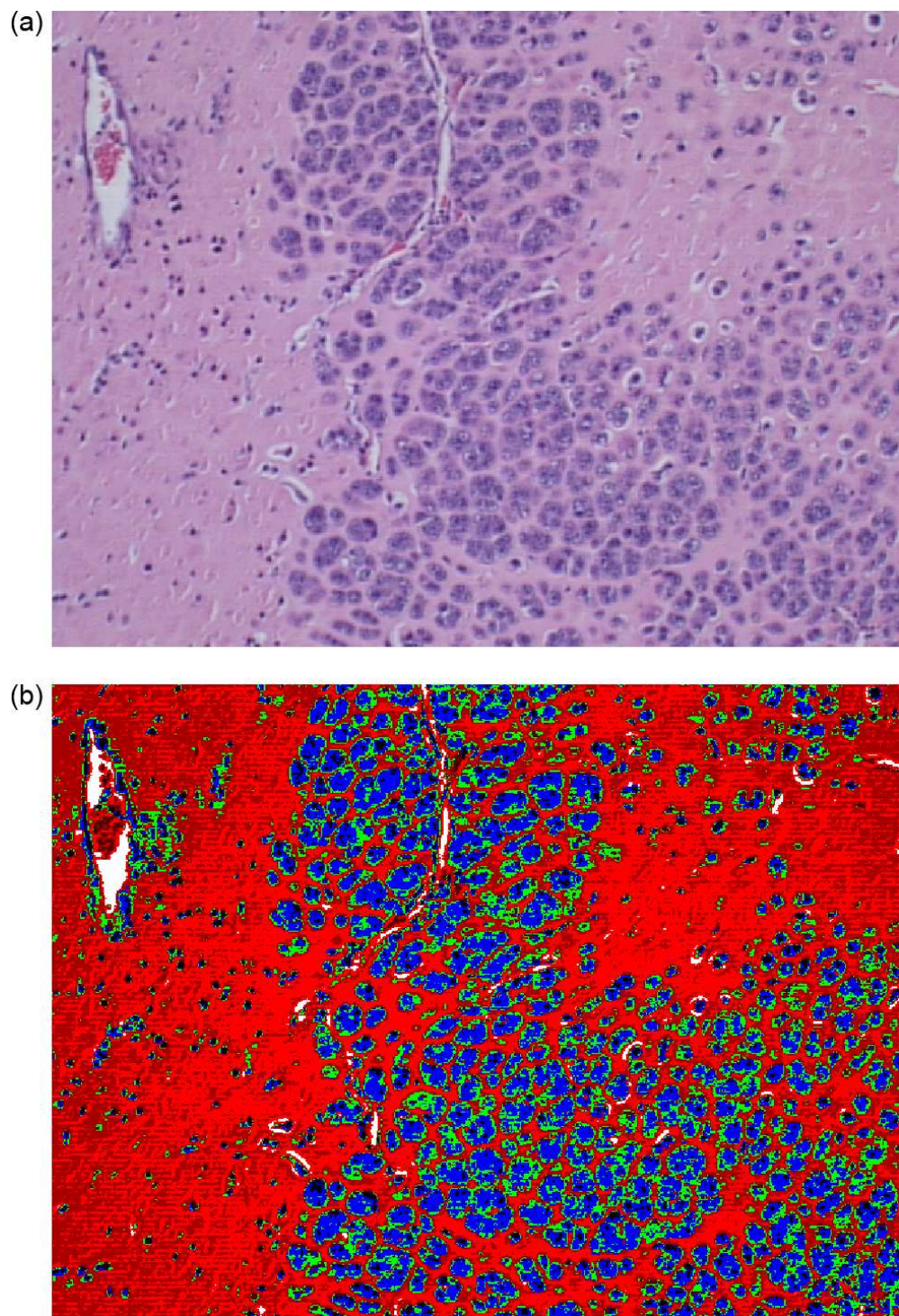


Figure 3.9 (a) Image of a light microscopy illustration of the H&E-stained histology of a tissue section from a EHS mouse sarcoma. (b) Image of the impedance map derived from this histologic section. Both images are $600 \times 800 \mu\text{m}$.

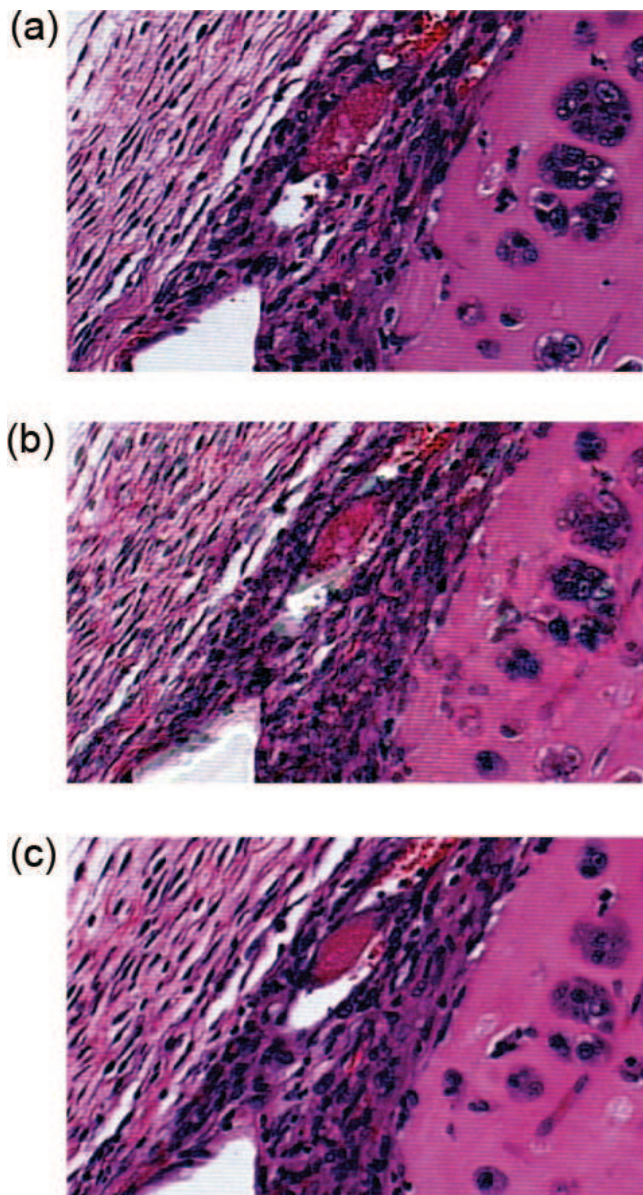


Figure 3.10 Section 15 (a) and 17 (c) of the EHS dataset and Hermite-interpolated missing section 16 (b). Image (b) was submitted to a pathologist under blind conditions for histopathologic evaluation.

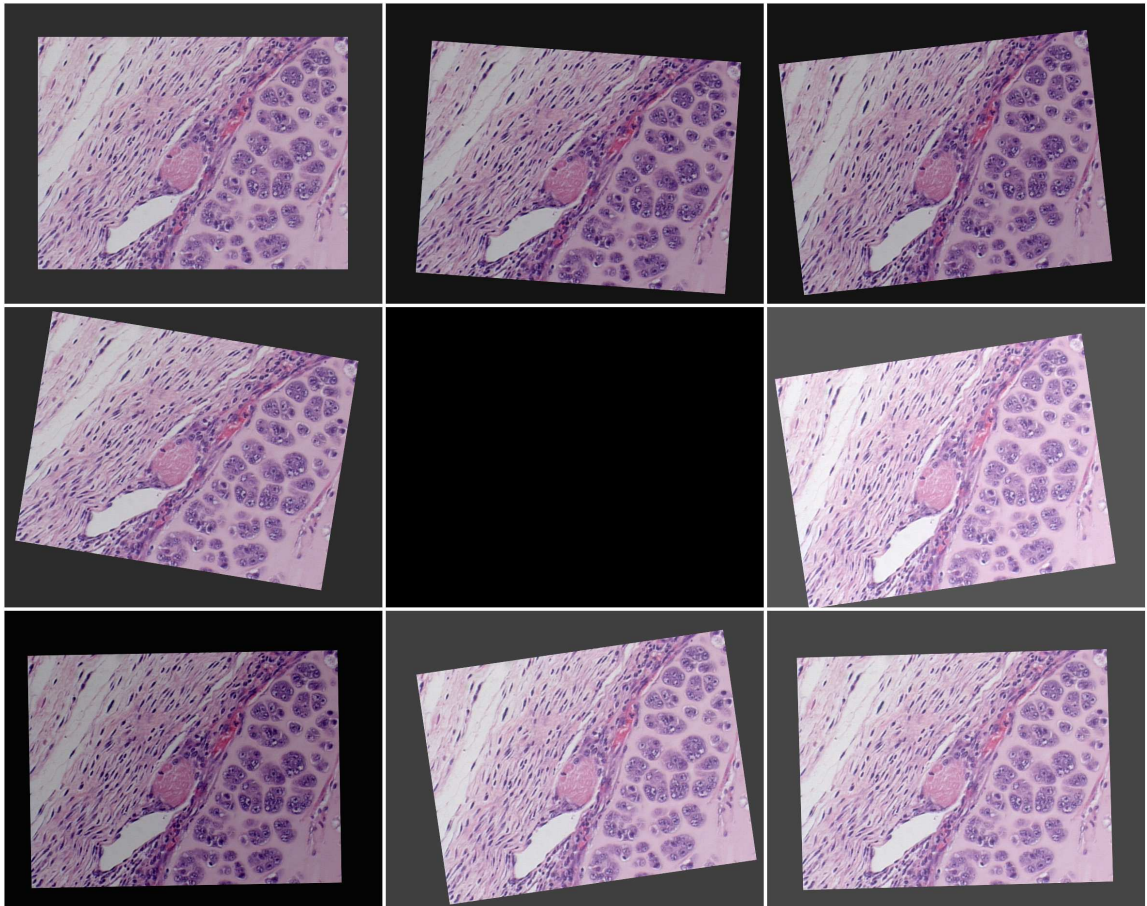


Figure 3.11 Nine-section dataset generated from the first section of the EHS dataset. Section numbering goes from left to right and top to bottom. Section 5 is missing and the other seven sections are deduced from the first section by random rigid transformation and random contrast change. Range of the DOFs of the random rigid transforms is shown on the third row of Table 3.2.

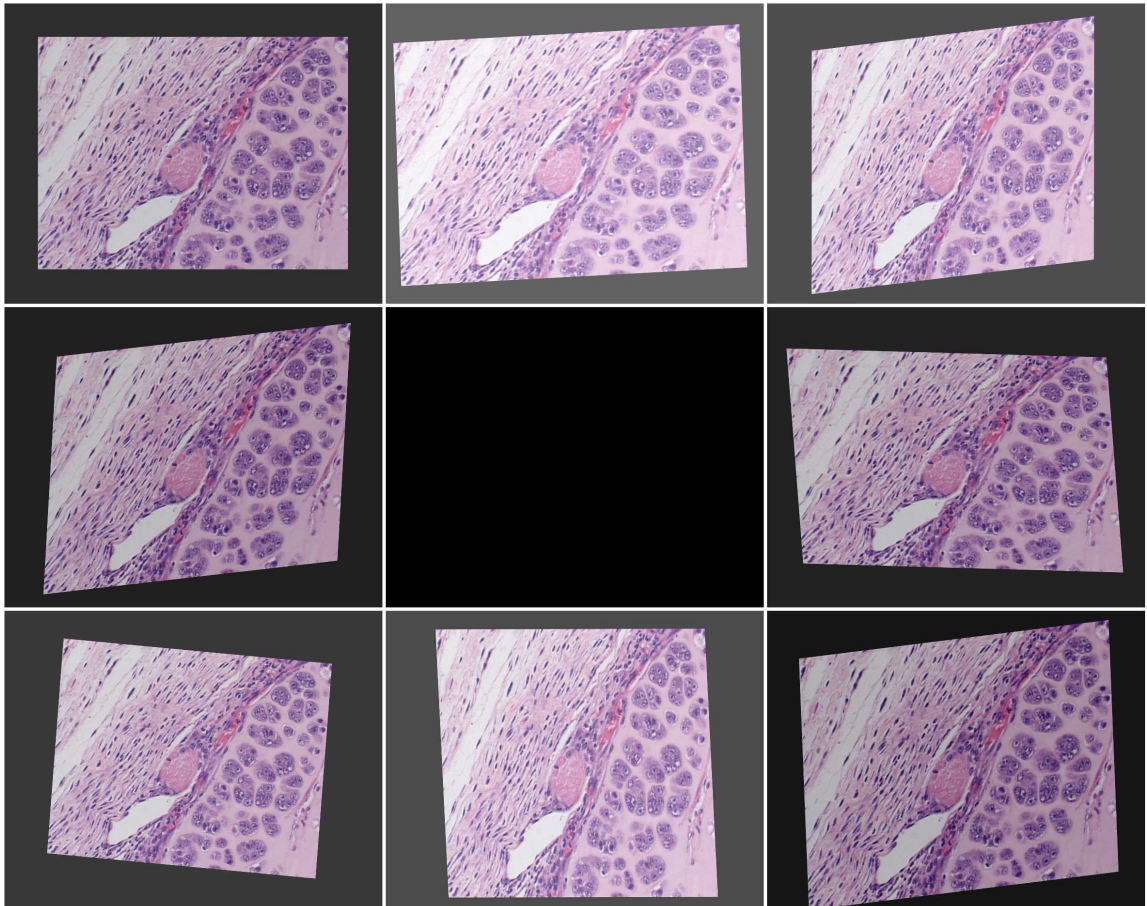


Figure 3.12 Nine-section dataset generated from the first section of the EHS dataset. Section numbering goes from left to right and top to bottom. Section 5 is missing and the other seven are deduced from the first section by random affine transformation and random contrast change. Range of the DOFs of the random affine transforms is shown on the fourth row of Table 3.2.

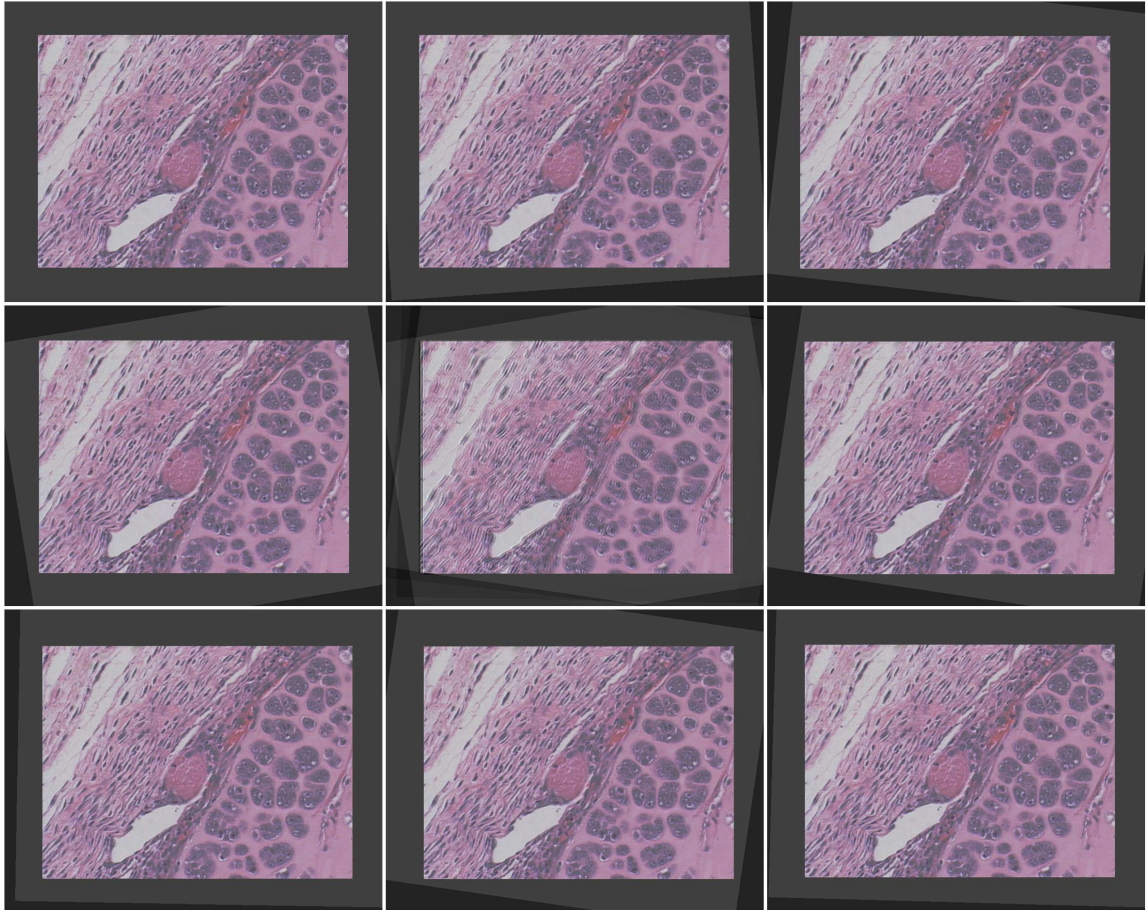


Figure 3.13 Reconstruction from the nine-section dataset of Figure 3.11. Section numbering goes from left to right and top to bottom.

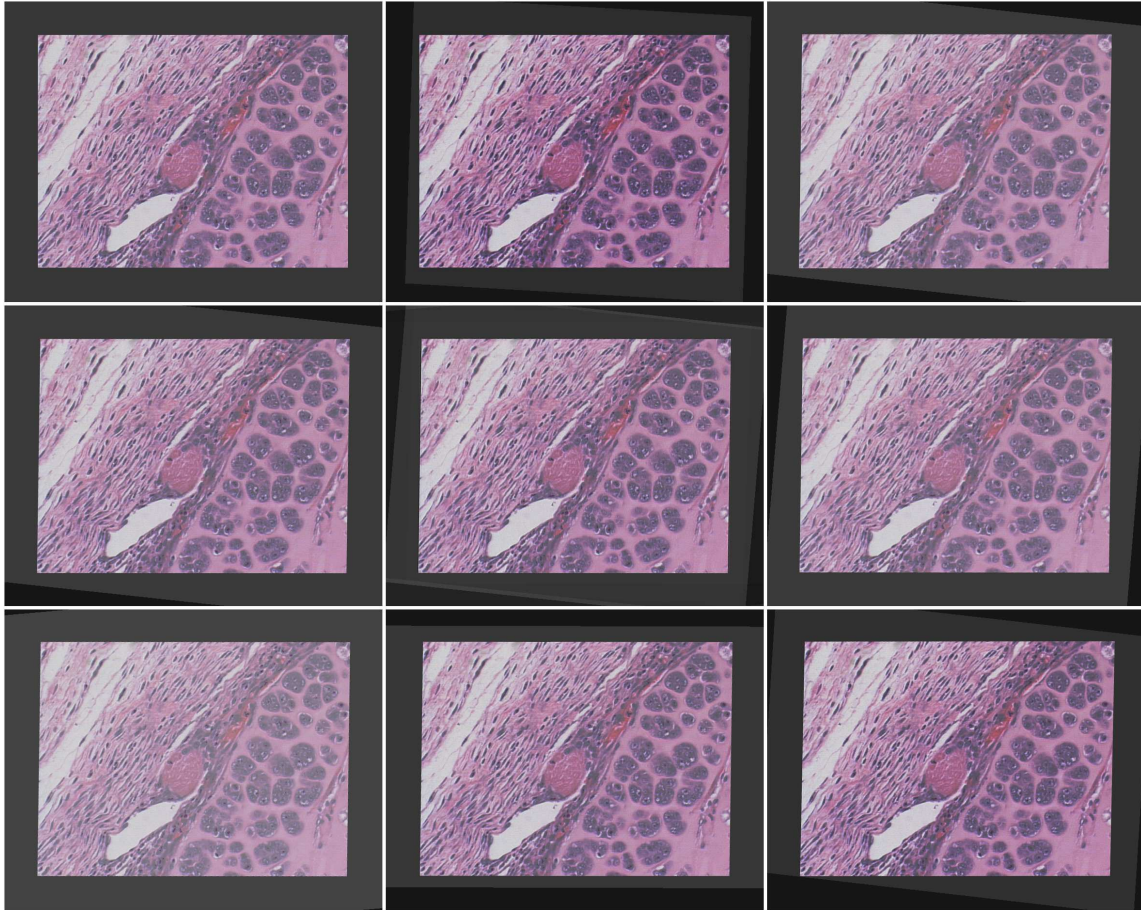


Figure 3.14 Reconstruction from the nine-section dataset of Figure 3.12. Section numbering goes from left to right and top to bottom.

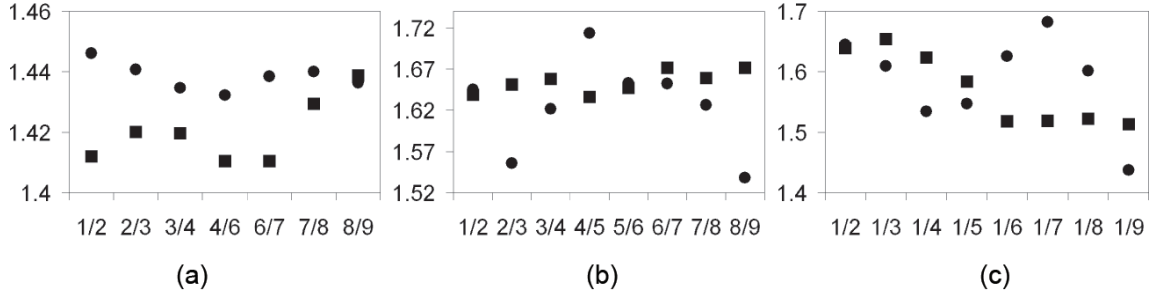


Figure 3.15 NMI plots deduced from the reconstructed datasets of Figures 3.13 and 3.14. Circles symbolize the NMI values for the rigid-transformed datasets and squares symbolize values for affine-transformed dataset. On the x -axis n/m represents the alignment between sections n and m . (a) Greatest NMI value obtained during registration optimization (i.e., using nearest-neighbor kernel). (b) NMI values from one section to the next after reconstruction (i.e., using cubic kernel for transformation and Hermite interpolation for missing section 5). (c) NMI values with respect to section 1 after reconstruction.

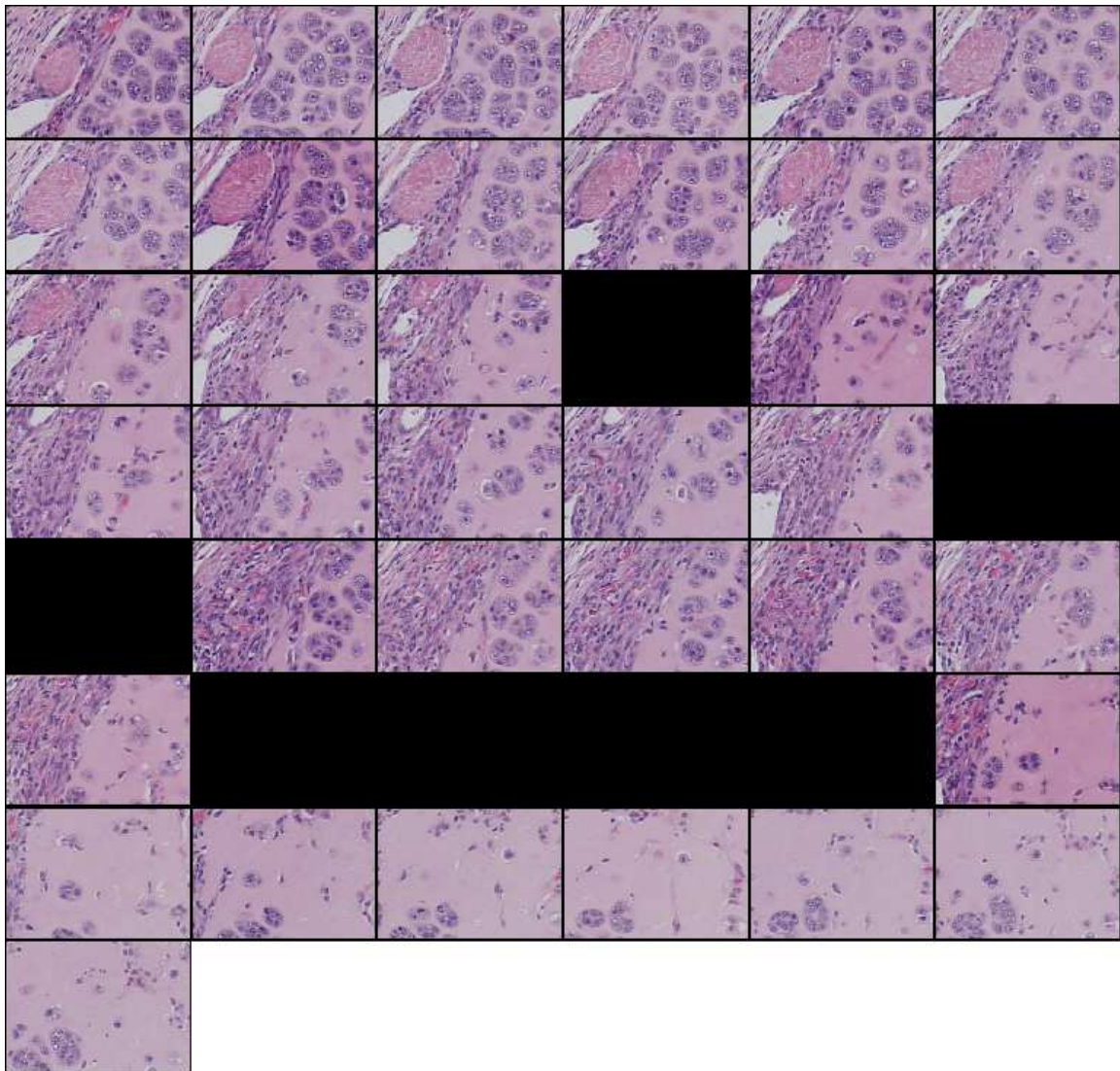


Figure 3.16 Forty-three-section dataset from the EHS dataset. Sections are of size $218 \times 156 \mu\text{m}$ (i.e., 350×250 pixels). Sections are subimages of size $218 \times 156 \mu\text{m}$ (i.e., 350×250 pixels) of the original $400 \times 300 \mu\text{m}$ EHS sections. Subimages were extracted from the same location in each of the 43 original EHS sections. The sections were consecutive from left to right and top to bottom. Black fields symbolize missing sections.

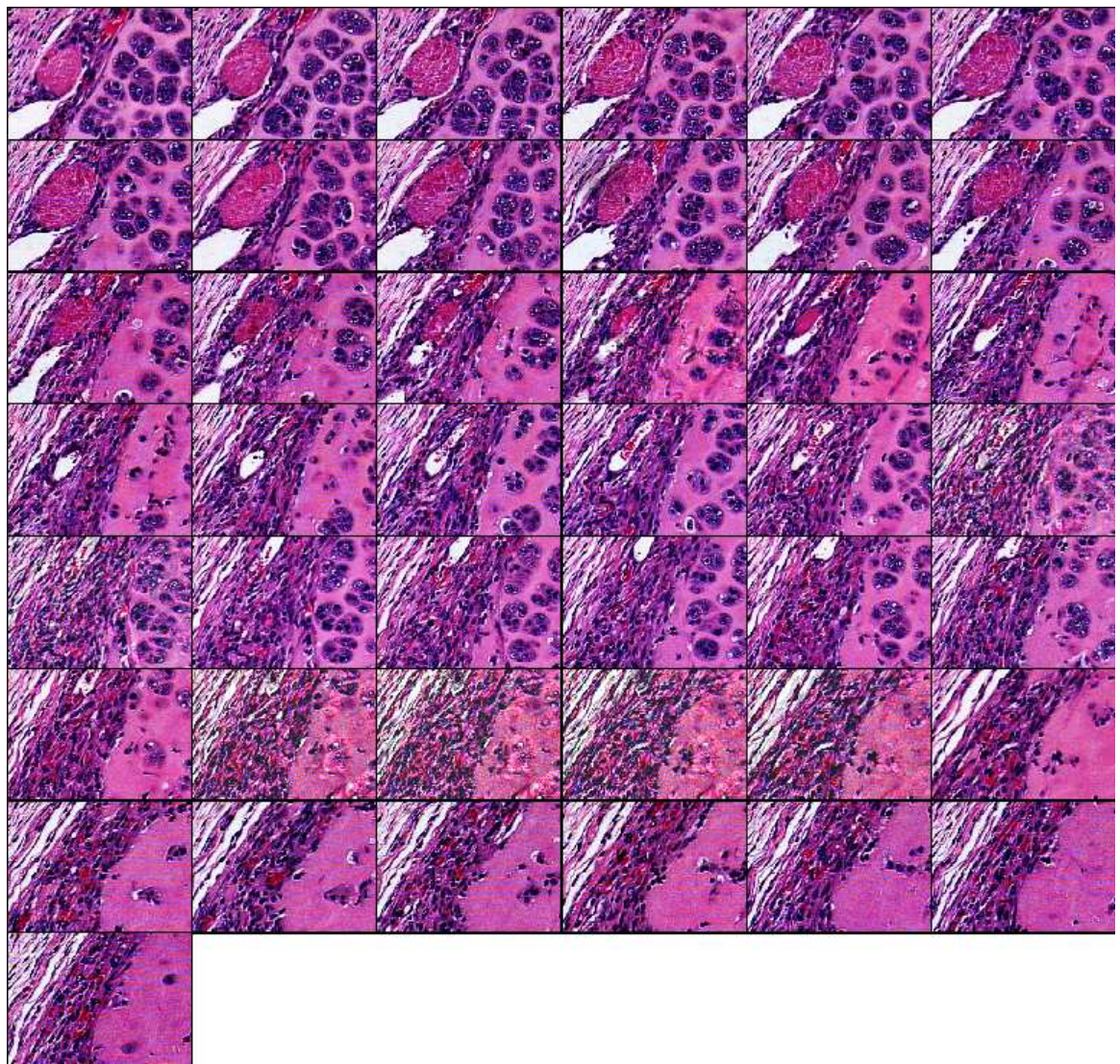


Figure 3.17 Reconstruction of the 43-section EHS dataset of Figure 3.16. The contrast of the available sections was equalized. Each section was affine-registered with the next available section. Missing sections were Hermite-interpolated.

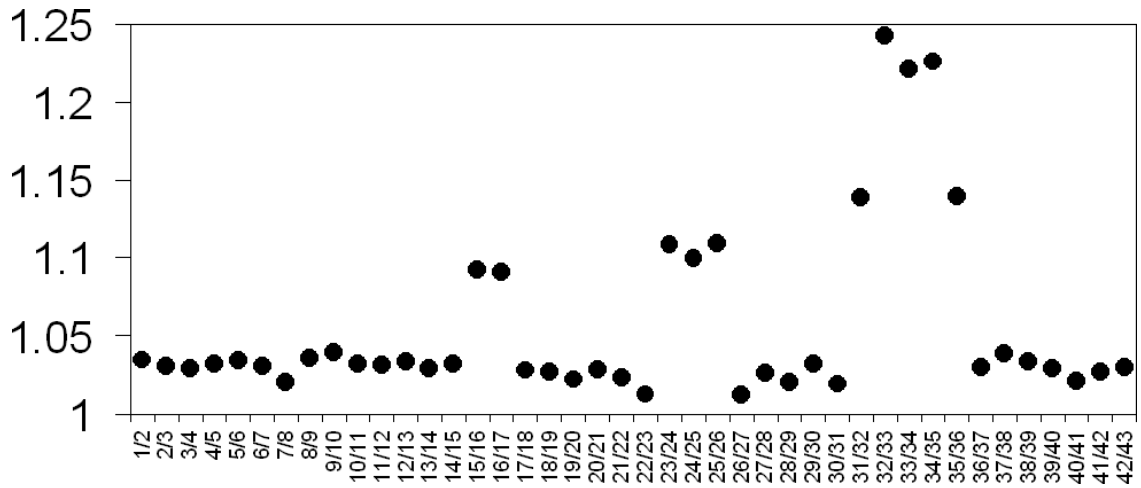


Figure 3.18 NMI values between consecutive sections of the reconstructed 43-section EHS dataset (Figure 3.17). On the x -axis n/m represents the alignment between sections n and m . NMI values are significantly smaller than those reported in Figure 3.15.

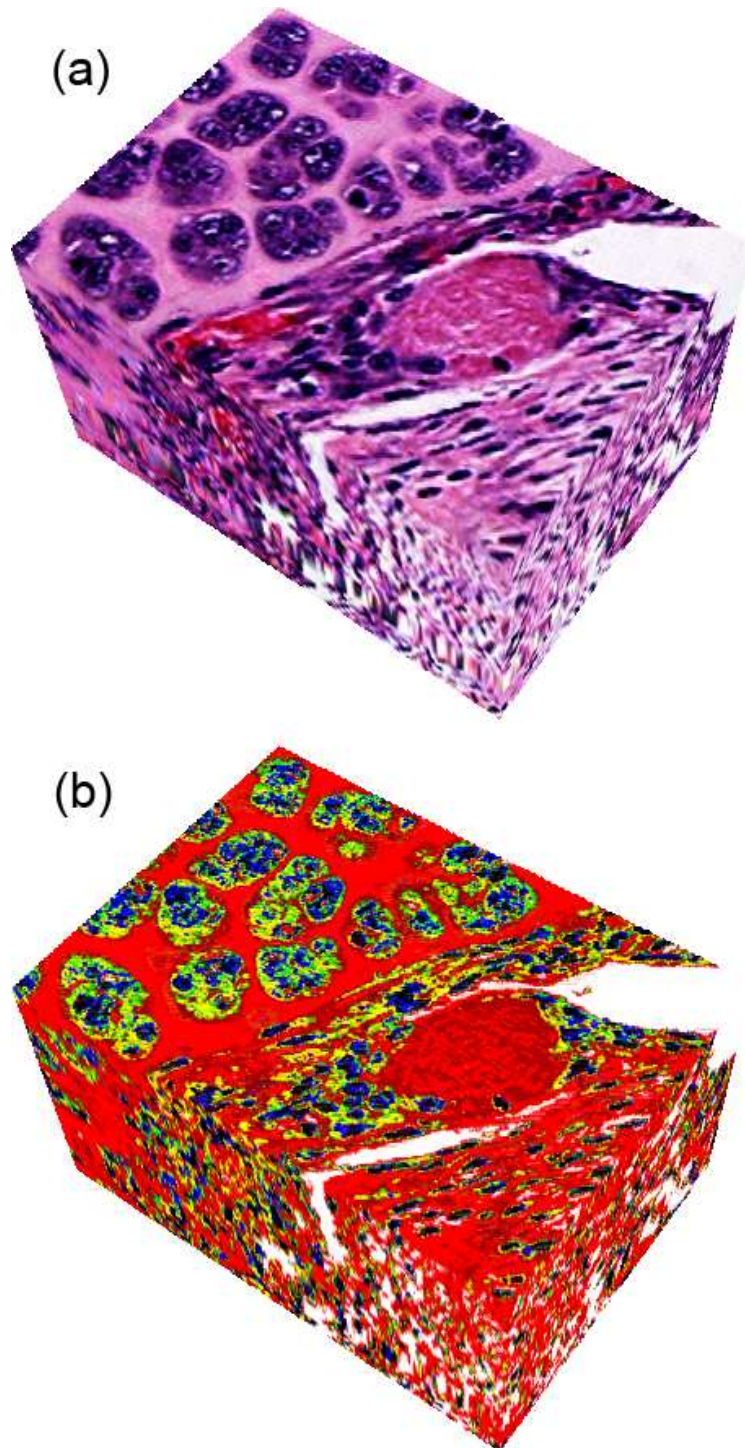


Figure 3.19 (a) Three-dimensional rendering from the 43-section dataset (Figure 3.17). (b) Derived 3D impedance map. The volumes shown in (a) and (b) are of size $218 \times 156 \times 129 \mu\text{m}$ (depth).

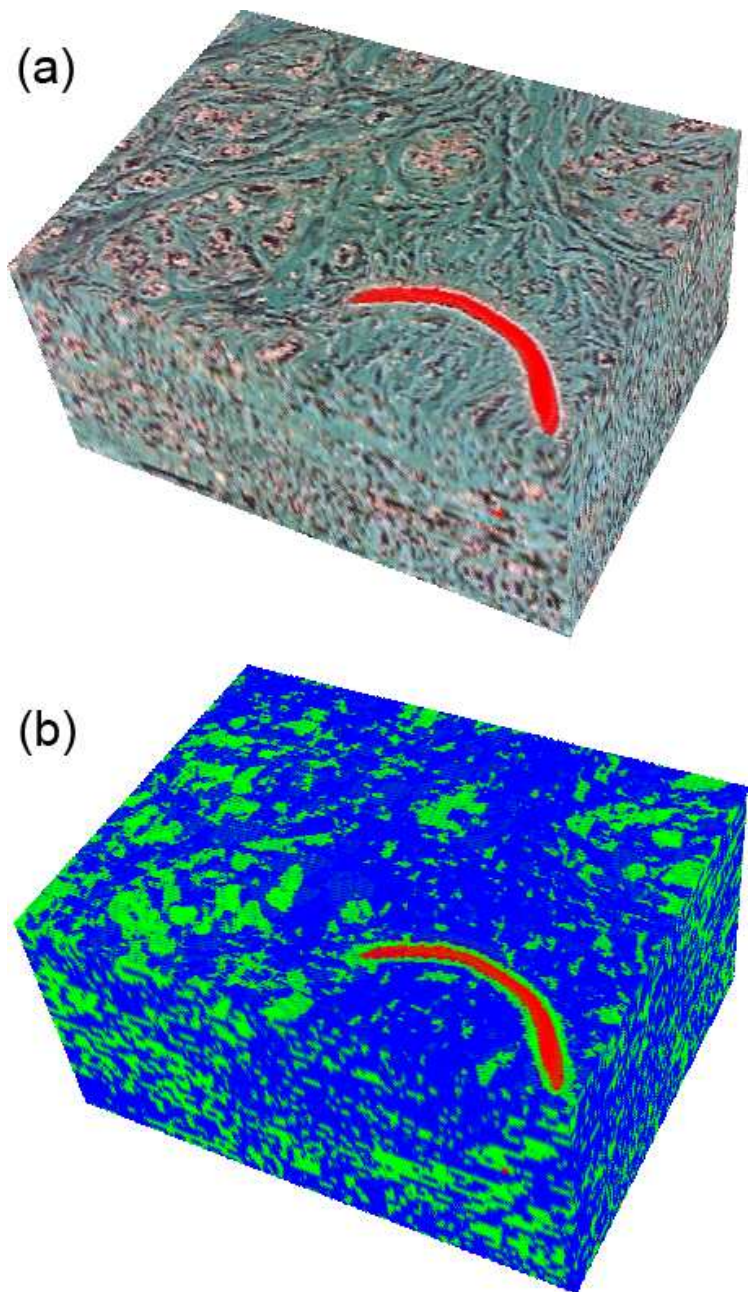


Figure 3.20 (a) Three-dimensional H&E-stained histology of a fibroadenoma. (b) Derived 3D impedance map. The volumes shown in (a) and (b) are of size $800 \times 600 \times 390 \mu\text{m}$.

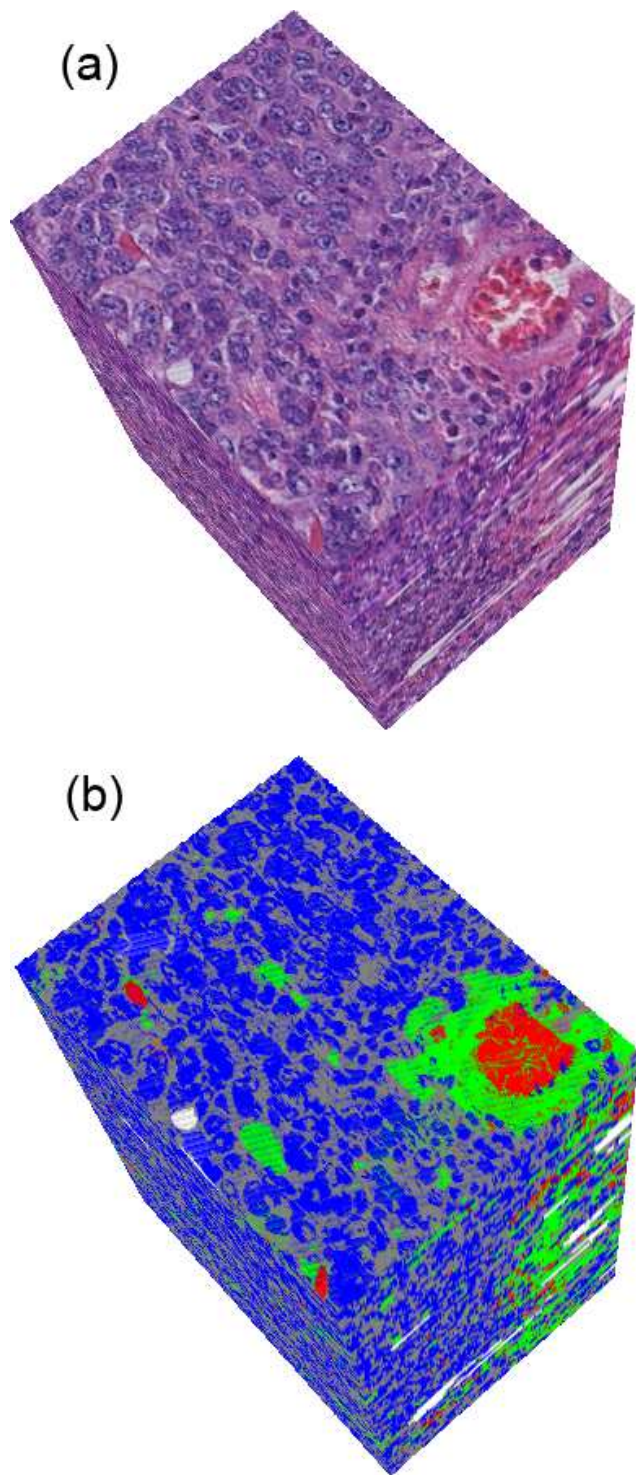


Figure 3.21 (a) Three-dimensional H&E-stained histology of a 4T1 mouse mammary carcinoma. (b) Derived 3D impedance map. The volumes shown in (a) and (b) are of size $200 \times 150 \times 330 \mu\text{m}$.

CHAPTER 4

TISSUE CHARACTERIZATION METHODOLOGIES

Three-dimensional impedance maps allow for the development of novel methodologies. Some may specifically lead to improved QUS techniques, while others may more generally help in the understanding of the fundamentals of how ultrasonic waves interact with biological media. Thus, this Chapter presents how the 3DZMs can be used for ultrasonic tissue characterization.

F3DZMs can yield ultrasonic descriptions of tissue microstructures. In particular, scatterer property estimates (scatterer size and acoustic concentration) can be obtained from any assumed FF over virtually any frequency range. The frequency-independent estimation scheme may hence reveal ultrasonic scatterer populations of different size distribution, for example.

Because 3DZMs were constructed from optical micrographs, they are essentially 3D volume representations of tissue volumes (Chapter 3). Thus, it is reasonable to think that they can be used to devise new FFs that would be realistic tissue-specific ultrasonic scattering models. 3DZM-deduced FF may lead to two main improvements of the QUS techniques. First, estimates using the 3DZM-deduced FF should be more accurate than those obtained using another FF, thus leading to improved contrast in the QUS images. Second, the duality between FF and the spatial autocorrelation function (Section 2.3) could be used to identify the anatomical structures responsible for ultrasonic scattering from the 3DZM-deduced FF.

4.1 Estimation Technique

This section presents the methodology used to obtain estimates from the power spectrum of a 3DZM. First, the 3DZM is divided into smaller volumes called regions of interest (ROIs). By dividing the 3DZM into smaller volumes, statistics about the estimates can be calculated from the different ROIs to show the precision of the estimation scheme. The scatterer size and acoustic concentration are then

estimated for each ROI by an estimation routine that fits the Gaussian FF to the power spectrum. The Gaussian FF was used so that results obtained herein could be compared with published experimental ultrasound estimates [23] that used the Gaussian FF. However, the estimation technique could be used the same way with any FF. Estimates are obtained by minimizing the mean squared error between the log of the normalized power spectrum ($S(2k)$; Eq. (2.26)) and the log of the Gaussian FF (Eq. (2.27)) over the radius a , that is,

$$a^* = \operatorname{argmin} \left[\int_{k_{min}}^{k_{max}} [\log(S(2k)) - \log(F_a^1(2k))]^2 dk \right]. \quad (4.1)$$

The value of a that gives the smallest mean squared error is the scatterer radius estimate (a^*). Because the log of the Gaussian FF is $-0.827(ka)^2$, that is, a linear function of $(ka)^2$, the complexity of the minimization routine is reduced and allows for an efficient least squares solution.

However, it is not always possible to accurately obtain the normalized power spectrum ($S(2k)$; Eq. (2.26)) directly from the power spectrum ($S'(2k)$; Eq. (2.26)), because the computed $S'(0)$ might be very inaccurate. When $k = 0$ the phase terms due to the random locations of scatterers add up instead of canceling each other like it is for the case when $k > 0$ (Appendix C provides further details by deriving a power spectra step by step). This fact makes the computed value of $S'(0)$ very different from its theoretical value (Eq. (2.26)). Thus, Eq. (4.1) is slightly modified to include a gain parameter G_a , so that $S'(2k)$ can be used directly instead of $S(2k)$. The gain parameter G_a is obtained from

$$\log(G_a) = \sqrt{\frac{1}{k_{max} - k_{min}} \int_{k_{min}}^{k_{max}} |\log(S'(2k)) - \log(F_a^1(2k))|^2 dk}. \quad (4.2)$$

Equation (4.2) is one of the choices to estimate a coefficient of proportionality between two functions. In particular, in the idealistic case where S' and F_a^1 are proportional ($S' = \Gamma F_a^1$, where Γ is a proportionality constant), Eq. (4.2) yields $G_a = \Gamma$.

The gain parameter G_a is dependent upon a and can also be related to the acoustic concentration;

$$C = n \left[\frac{z - z_0}{z_0} \right]^2, \quad (4.3)$$

where n is the number density of scatterers, $\frac{z-z_0}{z_0}$ is the relative impedance mismatch between the scatterers and the background impedance, and z_0 is the background impedance. G_a and C are then related by

$$C = G_a / V_s^2, \quad (4.4)$$

where V_s is the volume of a single scatterer [19]. V_s is equal to $\frac{4}{3}\pi a^3$ for the fluid sphere and the spherical shell. V_s is also equal to $\frac{4}{3}\pi a^3$ for the Gaussian sphere [7, 19].

Incorporating the gain parameter G_a , Eq. (4.1) becomes

$$a^* = \operatorname{argmin} \left[\int_{k_{min}}^{k_{max}} [\log(S'(2k)) - \log(G_a F_a^1(2k))]^2 dk \right], \quad (4.5)$$

in which $S(2k)$ has also been replaced with $S'(2k)$. Equation (4.5) is now easier to solve because $S'(2k)$ is simple to compute from the 3DZM. $S'(2k)$ is the magnitude squared of the Fourier transform of the 3D impedance map. Also from a^* , we can compute G_{a^*} and therefore estimate the acoustic concentration C^* from Eq. (4.4).

In order to solve Eq. (4.5), it is necessary to properly select the optimization range, k_{min} and k_{max} . An optimal ka^* range has been defined to be between 0.5 and 1.2 for the case of glass beads [7]. However, for the case of smoother FF (like the Gaussian FF) only the lower limit is the most important. For this work the ka range was chosen to be 0.5-2.0. For $ka^* < 0.5$, FFs are usually flat (their derivative vanishes as ka^* approaches 0) which leads to large inaccuracies in the estimates: estimates are found to be close to the lower bound of the estimation range (usually below 3–5 μm). For $ka^* > 2.0$, FF amplitudes are usually very low (e.g., –15 dB for the Gaussian FF) and noise can be dominant (backscattered signal amplitudes are already around –60 dB or less [7]). Table 4.1 shows the frequency ranges for scatterers of radii 10, 50, and 100 μm deduced from $ka = 0.5$ and $ka = 2.0$. A speed of sound of 1540 m/s was assumed.

The challenge for defining the optimal ka^* range is that it depends upon the estimated radius that is unknown. One approach could be to choose an average radius and then deduce from the optimal ka range values for k_{min} and k_{max} . However, computational trials using this approach have shown a bias in the estimates: all estimates were found to be within a few percent of the average radius chosen.

An alternate approach was used to define k_{min} and k_{max} . The goal of this approach was to obtain estimates that were not biased by the selected frequency range. Two

new parameters k_{start} and Δk , were defined where $k_{start} = k_{min}$ and $\Delta k = k_{max} - k_{min}$. An error function for the radius a is computed from

$$Err(a) = \text{Max} \{E(a, k_{start}, \Delta k), \text{ for every } k_{start} \text{ and } \Delta k\}, \quad (4.6)$$

where

$$E(a, k_{start}, \Delta k) = \frac{1}{\Delta k} \left[\int_{k_{start}}^{k_{start} + \Delta k} [\log(S''(2k)) - \log(G_a F_a^1(2k))]^2 dk \right], \quad (4.7)$$

and where the Err function is defined by the maximum of the mean squared errors over every frequency range. The optimal ka range is hence enforced by setting $E(a, k_{start}, \Delta k) = 0$ if $k_{start}a < 0.5$ or $(k_{start} + \Delta k)a > 2.0$.

Finally, a^* was defined as the argument of the absolute minimum of Err . This scheme has no built-in bias, because it evaluates every scatterer radius size over every frequency range while enforcing the optimal ka range. In particular, no specific frequency range has to be enforced. Thus, the strategy may possess the ability to find different populations of scatterers (different size, shape, impedance distribution etc). Populations of scatterers may be revealed by determining the different local minima of the Err function.

An alternate choice of the Err function could be

$$Err'(a) = \text{Min} \{E(a, k_{start}, \Delta k), \text{ for every } k_{start} \text{ and } \Delta k\}, \quad (4.8)$$

as replacement for Eq. (4.6) (also, enforcing optimal ka range would be accomplished by requiring $E(a, k_{start}, \Delta k) \rightarrow \infty$ if $k_{start}a < 0.5$ or $(k_{start} + \Delta k)a > 2.0$). However, applying Eq. (4.6) leads to better results because the Err' function curves are usually very flat and their minima are impossible to differentiate from noise. Err function curves usually show steep minima that are clearly distinct from noise.

4.2 Form Factor and Uniqueness of Estimation Results

It is obvious from Eqs. (4.6) and (4.7) that using different FFs will lead to different estimates. This remark raises the question of assessing the uniqueness of the results because different size estimates would be obtained from the same data (i.e., 3DZM). However, the results should be unique; that is, the size estimates should be equal to the size of the actual scattering sites. However, scattering sites are still undetermined, which makes it impossible to obtain an actual FF for a given scattering medium.

Nevertheless, if the actual and exact FF were known, then the estimation results would be unique.

Figure 4.1 illustrates how using a wrong FF can lead to inaccurate (i.e., biased) results. Figure 4.1 displays the fluid-filled sphere FF (Eq. (2.27)) along with a stretched version of the spherical shell FF (Eq. (2.29)). Specifically, the stretched spherical shell (SSS) FF is given by:

$$F_a^{3s}(2k) = [j_0(2[1.33ka])]^2, \quad (4.9)$$

where the superscript s means stretched. Equation (4.9) shows that F_a^{3s} is a 33% stretched version of F_a^3 . Figure 4.1 demonstrates that the fluid-filled sphere FF and the SSS FF are very similar up to a ka value of 2.2. Thus, if the SSS FF were used to estimate scatterer size of a medium containing fluid filled spherical scatterers, the mean size estimates obtained would be overestimated by about 33%. Thus, different estimates would be obtained even though the medium (i.e., 3DZM) and the scattering structures are the same.

4.3 Comparison of the 3DZM and Ultrasound Estimation Techniques

The 3DZM approach is a powerful tool to obtain statistical descriptions of tissue microstructure. The 3DZM approach is a tissue-based capability to compute the power spectrum (and the spatial autocorrelation function, SAF) of the medium in a very straightforward way through the Fourier transform (Section 2.2). To improve the power spectrum obtained from ultrasound, the ultrasonic techniques need to compensate for the experimental setting and the attenuation. Normalization removes dependence upon the experimental equipment [53] and attenuation compensation is used to mitigate the effects of attenuation [54]. If attenuation is not accounted for, estimates might become unreliable because attenuation is frequency dependent.

The power spectrum derived from ultrasonic measurements is only valid over the bandwidth of the transducer. Once the power spectrum is obtained, the optimization step in the ultrasonic technique is very similar to Eq. (4.1), except that k_{min} and k_{max} are fixed by the bandwidth of the transducer. The 3DZM approach has the advantage over the ultrasonic technique to obtain a power spectrum valid for a broader range

of frequencies. The only limitation of the 3DZM approach is the absolute size of the tissue volume and the voxel size.

4.4 3DZM-Deduced Form Factor

This section investigates the possibility to extract tissue-specific FF from 3DZMs. The theoretical model is first introduced, then the methodologies and finally the computer implementation.

4.4.1 Theory

Let us assume that a given 3DZM contains a single type of scatterer but with variations in size and in local number density. Nevertheless, one would want to be able to derive a FF from the available 3DZM that would be an accurate scattering model for this assumed single type of scatterer.

Henceforth, let us assume that the 3DZM is divided into N ROIs. Each ROI therefore contains a random number (i.e., a random acoustic concentration) of random sized scatterers of the same type for which the FF needs to be deduced.

Let us now focus on the power spectrum of the l^{th} ROI denoted by PS_l (where $1 \leq l \leq N$). Assume, to simplify notations, that the scatterers are isotropic and described by the sought after form factor $F^*(ka)$ and that the l^{th} ROI contains n_l scatterers randomly located within this ROI. The scatterers are assumed to have an acoustic impedance of z and the background impedance is z_0 . Basic Fourier transform properties lead to

$$PS_l(k) = E \left[\left| \sum_{p=1}^{n_l} \frac{z - z_0}{z_0} V_s(a_p) \sqrt{F^*(ka_p)} \exp(i[k_x x_p + k_y y_p + k_z z_p]) \right|^2 \right], \quad (4.10)$$

where $E[\bullet]$ symbolizes taking the expected value, a_p and $V_s(a_p)$ are the radius and the volume of the p^{th} scatterer in the l^{th} ROI, respectively; x_p , y_p , and z_p describes the random location of the p^{th} scatterer in the l^{th} ROI; and k_x , k_y , and k_z are the frequency variables of the 3D Fourier transform ($k = \sqrt{k_x^2 + k_y^2 + k_z^2}$). The term inside the absolute value bars is the 3D Fourier transform of the the l^{th} ROI. To expand and simplify this term, assume that the scatterer radii inside the l^{th} ROI have a narrow distribution, i.e., $\forall p a_p \approx \langle a \rangle_l$, where $\langle a \rangle_l$ symbolizes the mean radius of the scatterers

contained in the l^{th} ROI. This approximation also yields $\forall p V_s(a_p) \approx V_s(\langle a \rangle_l)$. Thus, Eq. (4.10) reduces to

$$PS_l(k) \approx \left[V_s(\langle a \rangle_l) \frac{z - z_0}{z_0} \right]^2 F^*(k \langle a \rangle_l) E \left[\sum_{p,q=1}^{n_l} e^{i[k_x(x_p - x_q) + k_y(y_p - y_q) + k_z(z_p - z_q)]} \right], \quad (4.11)$$

where the double sum term can be further reduced to

$$n_l + 2 \sum_{p>q} \cos [k_x(x_p - x_q) + k_y(y_p - y_q) + k_z(z_p - z_q)], \quad (4.12)$$

where $\sum_{p,q=1}^{n_l} = \sum_{p=q} + \sum_{p \neq q}$ was used. The imaginary part of Eq. (4.11) drops out because sine is an odd function and the coefficient 2 appears because cosine is an even function. Finally, the expected value of the second term of Eq. (4.12) is zero, because the sum of cosines is a random process with a zero expected value when $k > 0$. However, at zero frequency (i.e., $k = 0$), it is $n_l(n_l - 1)$. Thus, away from $k = 0$, Eq. (4.10) finally reduces to

$$PS_l(k) \approx n_l \left[V_s(\langle a \rangle_l) \frac{z - z_0}{z_0} \right]^2 F^*(k \langle a \rangle_l). \quad (4.13)$$

Equation (4.13) shows that PS_l can be approximated by the sought after FF of the unknown variable $k \langle a \rangle_l$ scaled by the unknown factor $n_l \left[V_s(\langle a \rangle_l) \frac{z - z_0}{z_0} \right]^2$.

4.4.2 Methodology

The next step is to estimate the function F^* from the 3DZM only. Let us assume that the 3DZM is divided into N ROIs for which the assumptions of Section 4.4.1 are true over a certain frequency range defined by $k_1 - k_2$. The goal is hence to retrieve F^* from the knowledge of PS_l for every l ($1 \leq l \leq N$).

The rationale comes from the remark below Eq. (4.13). Each PS_l will be transformed to $T_l(PS_l)$ using a transformation (T_l) with two DOFs (magnitude scaling and frequency axis scaling) to account for the two unknowns $n_l \left[V_s(\langle a \rangle_l) \frac{z - z_0}{z_0} \right]^2$ and $k \langle a \rangle_l$. The idea is that in the ideal case where Eq. (4.13) is valid, it should then be possible to find a set of N transforms such that the transformed power spectra are all the same. F^* will then be deduced by normalizing the common power spectrum to value 1 when $k = 0$ as it should be.

Obviously, it is unrealistic to expect that the transformed power spectra will fit perfectly because of the strong assumptions made in Section 4.4.1. Therefore, a

fitting criteria is introduced to quantify with a single number the similarity of the N transformed power spectra. This criterion is the mean standard deviation (MSTD) of the transformed power spectra over the chosen frequency range. Visually, the quantity that needs to be minimized is

$$\text{MSTD} = \frac{1}{k_2 - k_1} \int_{k_1}^{k_2} \frac{1}{N} \sqrt{\sum_{l=1}^N [T_l(PS_l)(k) - \langle T(PS)(k) \rangle]^2 dk}, \quad (4.14)$$

where $\langle T(PS)(k) \rangle$ is the mean of the transformed power spectra and is defined by

$$\langle T(PS)(k) \rangle = \frac{1}{N} \sum_{l=1}^N T_l(PS_l)(k). \quad (4.15)$$

The algorithm finishes when the N transforms (i.e., T_1, \dots, T_N) that minimize the MSTD (Eq. (4.14)) have been found.

4.4.3 Implementation

The implementation is not straightforward because the fitting algorithm is essentially trying to optimize simultaneously $2N$ unknowns. To reduce the number of unknowns, the power spectra are first transformed into a log scale. It is obvious that taking the log of Eq. (4.13) will transform the magnitude scaling term ($n_l \left[V_s(\langle a \rangle_l) \frac{z-z_0}{z_0} \right]^2$) in a magnitude shift ($\log \left(n_l \left[V_s(\langle a \rangle_l) \frac{z-z_0}{z_0} \right]^2 \right)$). This magnitude shift is removed by matching the means of the power spectra over the chosen frequency-range. Specifically, each log power spectra is modified according to the following:

$$\log [PS'_l] = \log [PS_l] - \frac{1}{k_2 - k_1} \int_{k_1}^{k_2} \log [PS_l(k)] dk. \quad (4.16)$$

Thus, matching the means reduces the optimization degrees of freedom to the N frequency scaling coefficients which are defined by $T_l(PS_l)(k) = PS_l(k\alpha_l)$. Furthermore, it is obvious from Eq. (4.13) that if $\{\alpha_l, \text{ for } 1 \leq l \leq N\}$ is a set of optimal scaling parameters then so is $\{\chi\alpha_l, \text{ for } 1 \leq l \leq N\}$ for χ arbitrary. This simple remark allowed for the further reduction of the degrees of freedom by enforcing a mean value of 1 for the set of scaling coefficients. This $N-1$ parameter optimization problem was finally implemented using the simplex algorithm [48].

Once the MSTD is minimized $\langle T^*(PS)(k) \rangle$ (the asterisk symbolizes the optimal transforms) should be a scaled version of the sought after FF F^* over the chosen

frequency range. However, to obtain the actual FF one also needs to transform $\langle T^*(PS) \rangle$ that is a function of k into a function of ka . The question is hence how to chose a ; an heuristic way of doing this would consist for example of picking a such that:

$$\frac{k_1 + k_2}{2}a = 1. \quad (4.17)$$

An alternate approach would be to assume that the chosen frequency range is such that $k_2 = 4k_1$, thus leading to a value of a such that the ka range is 0.5–2.0. Specifically, a would be deduced from $k_1 a = 0.5$ or equivalently $k_2 a = 2.0$. Nevertheless, unless prior information is known regarding the average size of the scattering structures, no perfect way exists to chose a .

Let's denote by $F(ka) = \langle T^*(PS)(k) \rangle$ the resulting function. This function of ka is now a magnitude-scaled estimate of $F^*(ka)$, that is, $F(ka) \approx BF^*(ka)$ for some unknown constant B .

However, it is normal to expect $F(ka)$ not to be a smooth curve, because it is a mean of N random processes (the N transformed power spectra). To deduce a usable FF from F there are several possible approaches. The simplest one would consist of keeping $F(ka)$ as it is, even though noisy, $F(ka)$ should be a curve with a fairly high signal-to-noise ratio (SNR) because it is the average of the transformed power spectra that minimizes the MSTD. The next option is to conduct a smoothing of F by either linear filtering (low-pass filtering) or nonlinear filtering (e.g., median filtering).

The problem with these filtering approaches is that the resulting estimate of F^* will be a function that is known only at the discrete locations where ka was sampled in the first place, which is a problem, for example, for the optimization step described in Section 4.1. Specifically, every time a new radius value a' is used to compute Eq. (4.7), the deduced form factor needs to be interpolated over the new ka' range. This is not an overwhelming problem but it may considerably slow down the numerous evaluations of Eq. (4.7).

To discard the need for interpolation, the approach is to model F^* as a function, $P(ka)$, that has a certain number of degrees of freedom ($P_{(\phi_1, \dots, \phi_n)}(ka)$), and find the parameters that minimize the mean-squared error:

$$\text{MSE}(\phi_1, \dots, \phi_n) = \int_{k_1}^{k_2} [F(ka) - P_{(\phi_1, \dots, \phi_n)}(ka)]^2 dk. \quad (4.18)$$

Because the expression for the function P is closed-form, it can be evaluated at any frequency exactly without the need for interpolation. Common choices for P would include polynomials of degree M ($M + 1$ DOF), or more advanced function like Fourier series of a certain order. However, because the ultimate goal is to fit this deduced FF to the available spectra, an advantageous model would be one that allows for fast optimization. Therefore, following the remark below Eq. (4.1), an advantageous choice would be the 2-parameter exponential model:

$$P_{(\alpha,n)}(ka) = e^{-\alpha(ka)^n}, \quad (4.19)$$

Which is an extension of the Gaussian FF. In particular, the exponential model reduces to the Gaussian FF when $\alpha = 0.827$ and $n = 2$. This model has been previously used to model FF over a given frequency range [55].

4.5 Two-Parameter Exponential Model

This section briefly investigates how well the two-parameter exponential model fits to FFs introduced in Section 2.3 over a specific ka range. Optimal parameters (α and n) that minimized the mean-squared error (MSE) were found (Table 4.2). The ka range was chosen such that the MSE was always below 10^{-4} . Such an MSE value guarantees a fit of excellent quality, because FFs are functions that have values that vary between 0 and 1. Also, it is not reasonable to hope for a good fit of the exponential model for any FF over a frequency range that includes local extremum (e.g., spherical shell over the ka range 1–2.5, Figure 2.1), because the exponential model describes monotonic functions of frequency.

Table 4.2 indicates that over the specified ka range the MSE is always very small ($\leq 5.3 * 10^{-5}$) which demonstrates the good quality of the exponential model fit to these FFs. Values of α are always in the fairly narrow range 0.713–1.544, except for the Gaussian-Gaussian FF ($a = 16 \mu\text{m}$, $\sigma = 4 \mu\text{m}$) that has a much larger value of 6.095. The values for n are all greater than 2.32, except for the Gaussian FF ($n = 2$) and the two Gaussian-Gaussian FFs ($n = 1.571$ and $n = 0.752$ for $\sigma = 4 \mu\text{m}$ and $\sigma = 12 \mu\text{m}$, respectively).

Certainly the goodness of fit is of importance when using a simple fitting model like the two-parameter exponential model. However, it is possible that these two parameters may not be able to track complicated behavior. In particular, as

mentioned before, the two-parameter exponential model is not useful when confronted with a FF that is not monotonic. Thus, it would be possible to obtain very close optimal values for σ and n for two FFs that may be fairly different. Obviously, in that case, degrees of freedom may be added to the model in order to track the differences between these two FFs.

As shown on Table 4.2 all the fits are valid over the smaller ka range 0.5–1.2. Therefore, to assess if the two-parameter exponential model is capable of tracking the differences between the seven FFs, a feature plot was constructed (Figure 4.2). This plot assesses visually if there exists FFs that are similar near $ka = 1$, which is a ka value included in the ka range of each FF (Table 4.2). The value and the slope at $ka = 1$ are given by the following:

$$P_{(\alpha,n)}(1) = e^{-\alpha} \quad (4.20)$$

$$P'_{(\alpha,n)}(1) = -n\alpha e^{-\alpha}. \quad (4.21)$$

Figure 4.2 indicates that the Gaussian-Gaussian FFs have unique behavior near $ka = 1$. This is demonstrated by the large distance between the two Gaussian-Gaussian points and all the other points.

This figure also demonstrates that the glass sphere and the spherical shell FFs have similar behavior near $ka = 1$. This fact is surprising considering how the physical aspects of these two models are different. Hence, it could be possible that it is due to poor modeling of these FFs by the exponential model. A strong resemblance between the glass sphere and the spherical shell FF fact was noticed earlier [7]. Further, the spherical shell FF was recently used for ultrasonic characterization of phantoms filled with glass beads [56]. Nevertheless, an exact FF (from Faran theory) was used in some other studies to characterize similar phantoms for which the diameter of the beads was unknown [57, 58]. The unknown bead diameter makes it impossible to know whether the curve fitting is conducted over the ka range where the glass bead FF is correctly estimated by the spherical shell FF.

The fluid-filled sphere and the fat sphere also have a similar behavior near $ka = 1$, which is expected because the fat sphere is essentially a fluid-filled sphere because it does not support significant shear waves. The Gaussian FF behavior is also similar to that of the fluid-filled sphere FF; this was already visible from the plots of these two FFs on Figure 2.1.

To summarize the results presented on Table 4.2 and Figure 4.2, the two-

parameter exponential FF model was capable of tracking the differences (and also the similarity) between the seven FFs. In particular, the FFs that the model may confuse are those that were already similar to begin with (i.e., glass sphere and spherical shell, fluid-filled sphere and Gaussian, and fluid-filled sphere and fat sphere).

4.6 Tables and Figures

Table 4.1 Frequency ranges deduced from $ka = 0.5$ and $ka = 2.0$ ($c = 1540$ m/s).

Scatterer radius (a)	Frequency range
10 μm	12.3–49.0 MHz
50 μm	2.45–9.80 MHz
100 μm	1.23–4.90 MHz

Table 4.2 Exponential models fit to seven distinct FFs. The table shows the ka range and the parameters α and n that minimized the mean-squared error (MSE).

Form factor considered	ka range	α	n	MSE
Gaussian	any	0.827	2	0
Fluid-filled	0.5–1.5	0.792	2.348	$5.98 \cdot 10^{-6}$
Spherical shell	0.4–1.2	1.485	2.618	$2.72 \cdot 10^{-5}$
Glass sphere	0.3–1.5	1.431	2.320	$1.10 \cdot 10^{-5}$
Fat sphere	0.4–1.5	0.713	2.531	$2.06 \cdot 10^{-5}$
Gaussian-Gaussian ($a = 16 \mu\text{m}$, $\sigma = 4 \mu\text{m}$)	0.5–2.0	1.544	1.571	$2.30 \cdot 10^{-6}$
Gaussian-Gaussian ($a = 16 \mu\text{m}$, $\sigma = 12 \mu\text{m}$)	0.5–2.0	6.095	0.752	$3.32 \cdot 10^{-5}$

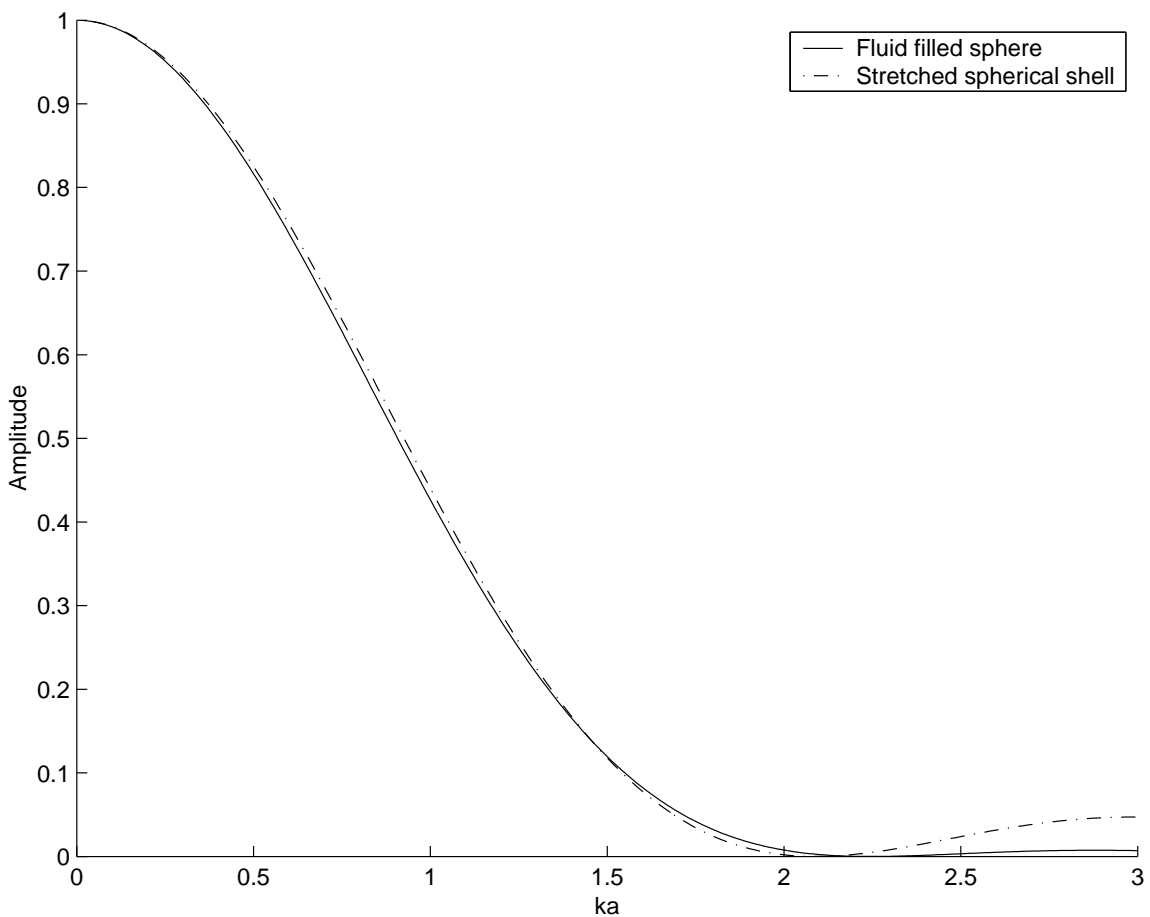


Figure 4.1 Plots of the fluid-filled sphere and the stretched spherical shell form factors. The plots are displayed as a function of ka over the range $0 \leq ka \leq 3$.

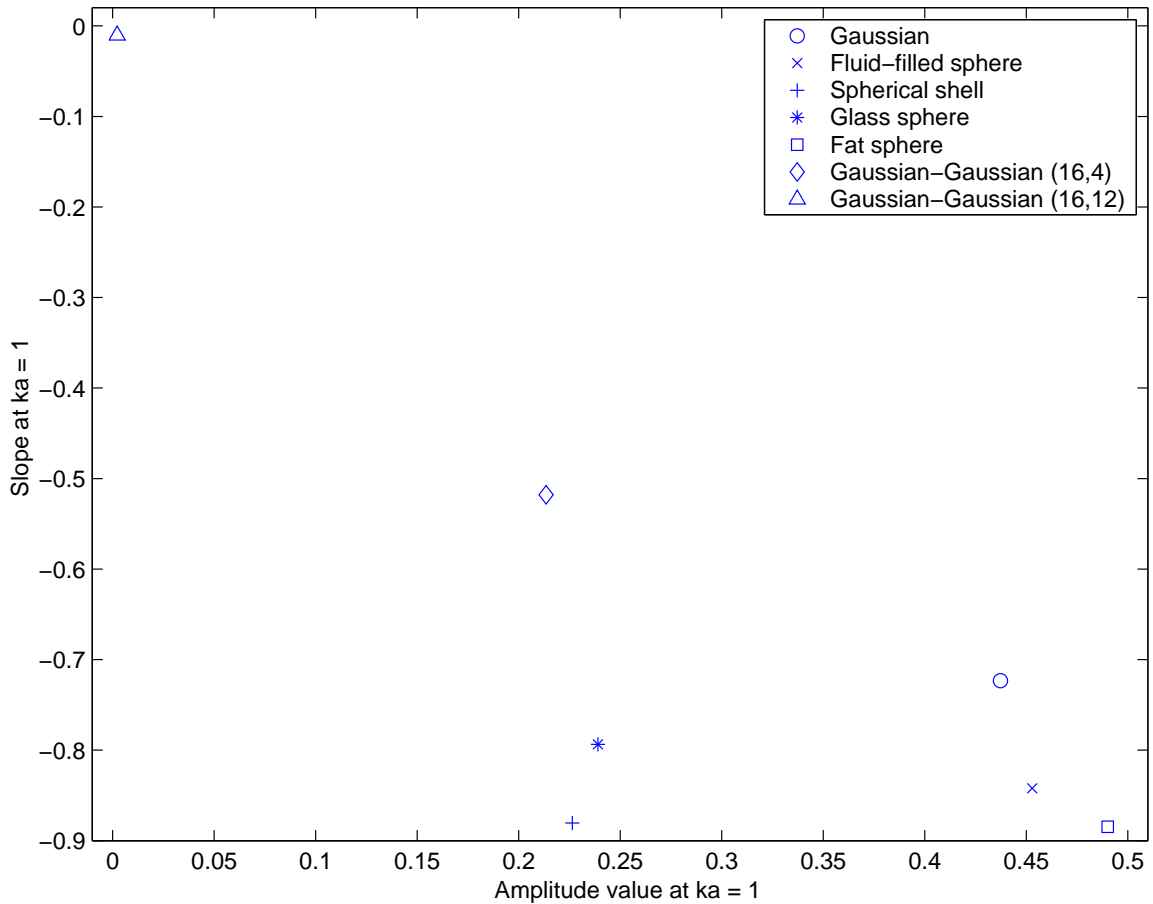


Figure 4.2 Features plot deduced from the optimal parameters of the exponential model fit for seven FFs. For each FF, the feature plot displays the value and the slope of the exponential model fit at $ka = 1$. For the Gaussian-Gaussian FFs, the numbers between parentheses are the values used for a and σ , respectively, in Eq. (2.33) in micrometer.

CHAPTER 5

TISSUE CHARACTERIZATION RESULTS

This chapter gathers the characterization results obtained using the methodologies of Chapter 4. In particular, estimates for scatterer size and acoustic concentration were obtained for simulated 3DZMs to validate the characterization methodologies (estimation and FF extraction). For the simulated 3DZMs the quality of the estimates can be quantitatively assessed because the actual values are known. Then, estimates were obtained from a rat fibroadenoma, a 4T1 mouse mammary carcinoma and an EHS sarcoma. For the tumors, estimates were obtained with two different FFs. The Gaussian FF was first used to allow for comparison with the ultrasonic measurements conducted on the same tumor tissue. The second FF was a 3DZM-deduced FF specific to each tumor.

5.1 Simulations

Simulated 3DZMs of different complexity were constructed. First, 3DZMs containing a single population, then two, then finally a distribution of size. In particular, the FF extraction methodology was also evaluated on simulated 3DZMs divided into ROIs containing different distributions of scatterers.

5.1.1 Single-population simulations

The first two simulated media were 3DZMs of the same size ($256 \times 256 \times 256 \mu\text{m}$) containing 15 fluid sphere-like scatterers of the same diameter. The scatterer diameters were $40 \mu\text{m}$ for medium A and $80 \mu\text{m}$ for medium B. The background had an impedance of 1.50 Mrayl and the spheres had an impedance of 1.51 Mrayl. The acoustic concentration was the same for both media (same number density of scatterers and same impedance difference between scatterer and background), that

is,

$$C = \frac{15}{(256 * 10^{-6})^3} \left[\frac{1.51 - 1.50}{1.50} \right]^2 \\ = 0.0397 \text{ mm}^{-3}.$$

Acoustic concentration values may have a large dynamic range from one ROI to another. Therefore, acoustic concentration is expressed as: $C_{dB} = 10 \log(C)$ (and not $20 \log(C)$, because C is directly related to the amplitude of the power spectrum and is hence a second order quantity). For the two simulated media $C_{dB} = -14.01 \text{ dB mm}^{-3}$. For the simulations, in Eq. (4.5), F_a^1 was replaced by the FF for a fluid sphere case F_a^2 , and each voxel in the 3DZM was represented by a cube of side length $1 \mu\text{m}$.

For both simulated media, the power spectra from 10 random realizations of the 3DZMs were averaged to limit the noise due to the spatial variations of the locations of the spheres. Fifty 10-realization spectra were computed for each medium. From the 50 spectra, 50 size (diameter) and acoustic concentration estimates were obtained (Table 5.1). For both media the average estimates were close to the actual values (relative errors less than 3% for all four average estimates). The $\log(Err)$ plots as a function of the scatterer diameter for realizations of media A and B showed that absolute minima were located very close to the actual scatterer diameters (Figure 5.1), that is, $40.8 \mu\text{m}$ for medium A and $81.0 \mu\text{m}$ for medium B. The values of Err at the minima were also very close for media A and B curves ($\log(Err)$ values were around -1.8 for both curves). Thus, the single population simulation studies validated the 3DZM methodology as a means to obtain accurate estimates for a single population of scatterers.

Figure 5.1 shows that diameters between $20 \mu\text{m}$ and $160 \mu\text{m}$ were tested. Because the ka range chosen for optimization was $0.5\text{--}2.0$, one can deduce that the optimization scheme evaluated any frequency range included in the interval [1.53 MHz–49.0 MHz].

Both curves (Figure 5.1) showed sawtooth-like behavior for large scatterer diameters. Equation (4.6) should yield a smooth curve if an infinite number of frequency ranges were evaluated. However, because a finite number of frequency ranges were evaluated, the sawtooth-like behavior resulted. Also, the sawtooth-like behavior was more likely to occur for large scatterer diameters because fewer

frequency ranges were available from which to select, and because enforcing the upper bound of the ka range limited the number of frequency ranges available for large a . This sawtooth-like phenomenon could be removed artificially by low-pass filtering the error curves or by increasing the zero padding when computing the spectra so that more frequency ranges were available.

5.1.2 Two-population simulations

The next simulations evaluated the feasibility of identifying two population sizes of scatterers buried in a single medium. Seven media were simulated and the impedance mismatches were the same for both populations: 1.51 Mrayl for the spheres and 1.50 Mrayl for the background (Figure 5.2). The acoustic concentration of the 40- μm scatterers was constant at $-14.01 \text{ dB mm}^{-3}$ (same value as for media A and B). The acoustic concentrations of the 80- μm scatterers were (from top to bottom at the horizontal axis location of about 40 μm): -9.01 , -14.01 , -17.01 , -20.01 , -23.01 , -26.01 , and $-29.01 \text{ dB mm}^{-3}$. These seven media were the same size as media A and B (cube with side length of 256 μm), and each voxel was represented by a cube of side length 1 μm .

As the acoustic concentration of the 80- μm scatterers increased, the topologies of the curves could be classified in three categories: (1) single clear minimum around 40 μm (for 80- μm scatterer acoustic concentration of -29.01 and $-26.01 \text{ dB mm}^{-3}$), (2) two clear minima around 40 μm and in the range 75-80 μm (for 80- μm scatterer acoustic concentration of -23.01 and $-20.01 \text{ dB mm}^{-3}$), and (3) single clear minimum near 80 μm (for 80- μm scatterer acoustic concentration of -17.01 , -14.01 and -9.01 dB mm^{-3}). Hence, for the small scatterer population to be the only one detected (i.e., category (1)) a much higher acoustic concentration of small scatterers than large scatterers was necessary (a small scatterer acoustic concentration at least 12 dB mm^{-3} higher than that of the large scatterers). However, the large scatterer population is the only one detected (i.e., category (3)) when the small population acoustic concentration is at the most 3 dB mm^{-3} higher than that of the large population. Finally, in between (i.e., category (2)), the curves tend to show two minima, one for each population.

A similar two-population study was also conducted where this time the number density was kept the same for the 40- μm and 80- μm populations. However, the impedance values of the 80- μm scatterers were varied. The impedance values chosen

were such that the 80- μm acoustic concentration had the same seven values as in the previous simulations (-9.01 , -14.01 , -17.01 , -20.01 , -23.01 , -26.01 , and $-29.01 \text{ dB mm}^{-3}$). Like before, the 40- μm acoustic concentration was kept constant at $-14.01 \text{ dB mm}^{-3}$. The error curves obtained were extremely similar to those of Figure 5.2.

These simulations showed that with a factor of two in size and under certain conditions (in particular concentration), it was possible to resolve the two populations using the 3DZM optimization scheme. However, it seems difficult to assess the resolution of the scheme based on this first set of two-population simulations.

The set of simulations showed that the 3DZM approach has the potential to resolve populations of different sized scatterers. Resolving different populations of scatterer size was possible only when the smaller sized scatterers' acoustic concentration was greater than that of the larger sized scatterers. The difficulty of resolving two scatterer size populations arises from the relative contribution of each population to the overall power spectrum. The power spectrum of a single population is proportional to Ca^6 , where a and C are the scatterer radius and acoustic concentration, respectively. Therefore, if the acoustic concentrations are equal, the contribution of the smaller sized scatterers to the overall magnitude of the power spectrum will be much less than the contribution of the larger sized scatterers because the spectrum is proportional to the radius to the 6th power.

These two 2-population studies demonstrated that the power spectrum is sensitive to the acoustic concentration, but not individually on the number density or the impedance values of the different scatterers. This is in accordance with ultrasonic scattering theory and was clearly pointed out by Insana et al. [7]. Therefore, in order to resolve smaller scatterers in a two-population medium, either the number density of smaller scatterers must be much larger than that of the larger scatterers or the impedance mismatch for the smaller scatterers must be much larger than that for the larger scatterers.

5.1.3 Gaussian size distribution simulations

This set of simulations involved 3DZMs containing a single population of Gaussian scatterers whose sizes followed a Gaussian distribution with variable mean and standard deviation. The theoretical FF is Gaussian-Gaussian and was derived in closed-form in Section 2.3.4.

For these simulations also, the scatterers had an impedance of 1.51 Mrayl and a background of 1.50 Mrayl. The Gaussian scatterers had sizes following a Gaussian distribution with a mean diameter of $40 \mu\text{m}$, and the standard deviation (STD) was varied from $2 \mu\text{m}$ to $20 \mu\text{m}$ by $1 \mu\text{m}$ increments.

Three sets of estimations were conducted on these 3DZMs. First, the Gaussian FF was used to estimate scatterer sizes. This simulation was meant to assess further how the presence of large scatterers bias the estimates. Second, the Gaussian-Gaussian FF was used and σ was assumed to be known. Third, the Gaussian-Gaussian FF was used but nothing was assumed about the value of σ . For all three cases and each STD value, diameter estimates were computed for 64 random realizations of the same 3DZM.

Estimates using the Gaussian FF. The Gaussian FF is often used to estimate scattering sizes in tissues; however, it is unlikely that scattering structures in tissues have all the same sizes. Thus, this study gives a sense of how the quality of the Gaussian estimates degrades as the STD of the scatterer size distribution increases while keeping the mean size the same.

Estimates are shown on Figure 5.3. This figure indicates that the larger scatterers make the estimation scheme overestimate the scatterer sizes. This is shown by the increasing mean diameter estimate as a function of the STD. When the STD is large there is a greater variation around the mean ($40 \mu\text{m}$) of the diameter distribution leading to in particular larger scatterers than for a smaller STD. When the $\text{STD} = 2 \mu\text{m}$ the diameter estimate is slightly overestimated ($40.3 \pm 0.36 \mu\text{m}$), when the $\text{STD} = 10 \mu\text{m}$ the diameter estimate is overestimated by $5.4 \mu\text{m}$ ($45.4 \pm 0.33 \mu\text{m}$), and when the $\text{STD} = 20 \mu\text{m}$ the diameter estimate is overestimated by more than $10 \mu\text{m}$ ($52.2 \pm 0.33 \mu\text{m}$). This study showed that with a continuous distribution of sizes in the 3DZM, average scatterer size estimates were biased larger than the actual mean size.

Figure 5.3 demonstrates that even though biased the Gaussian estimates are very precise because the standard deviation of the estimates is always extremely small (below $0.5 \mu\text{m}$). The bias of the estimates is a problem when one is looking for absolute (average) sizes of structures. However, if one is only looking for image contrast, it is fine if all the estimates are biased the same. For example, if in each ROI the size estimates are overestimated by the same percentage, then the contrast

in the reconstructed QUS will be satisfactory (i.e., ROIs that contain different size scatterers will be differentiated). In particular, if the size estimates were displayed on a log scale, then the QUS image obtained will be exactly the same as the QUS image that would have been obtained if all the estimates were accurate.

Furthermore, Figure 5.3 also demonstrates that the Gaussian estimates were capable of tracking the changes when the STD was changed. The Gaussian estimates were different for each STD. Thus, a QUS image constructed based on these estimates would show contrast between two ROIs containing scatterers of the same type but with a different size distribution. This contrast is of course a desired property.

QUS image contrast is important for potential diagnostic application. However, the fact that the Gaussian size estimates do not represent the average size of the actual scattering structures contained in a given ROI is a serious problem if one is trying to identify scattering structures. Specifically, a way to come up with *tentative* ultrasonic scatterers is to find the structures in the tissue sample that have a size similar to the size estimates. Thus, the overestimated Gaussian estimates would lead to wrongly selected larger structures.

Estimates using a Gaussian-Gaussian FF with actual σ value. For the second estimates, the exact FF (Gaussian-Gaussian with the value of σ known) was used for each 64 realizations of the same ROI. Thus, accurate results were expected because the FF was used with the optimal value for the STD of the size distribution. This simulation was meant to quantify if the use of the actual but advanced FF lead to a great improvement of the estimate accuracy. Also, this simulation can be seen as a sanity check of the derivation of the Gaussian-Gaussian FF, Eq. (2.33).

The results (Figure 5.4) are presented in the same format as Figure 5.3. Also, to allow easy comparison the scales of the plots were the same. Figure 5.4 demonstrates that the estimates are very accurate and independent of the STD value. The mean estimates are all in the very narrow range 39.9–40.1 μm . The STD of the estimates (over the 64 realizations for each STD value) is also very small, always below 0.9 μm . The STD shows a slight increasing trend with the STD value (from 0.37 μm to 0.89 μm for STD values of 2 and 20 μm , respectively). This slight increase can be explained by the fact that when the STD increases, a larger number of scatterer would be necessary to make the size distribution look Gaussian, whereas when the distribution is fairly narrow, it does not really matter how many scatterers are present

because they all have very similar sizes.

This simulation proved the validity of the derived Gaussian-Gaussian FF and also showed that when the actual FF is known and used, accurate results can be obtained even with a complicated FF such as Eq. (2.33).

Estimates using a Gaussian-Gaussian FF with unknown σ value. Obviously, when trying to characterize a tissue sample, it is unlikely that an accurate value for the STD of the size distribution of the scattering structures may be known beforehand. Thus, in the third estimates, the Gaussian-Gaussian FF was used but the STD was unknown. Specifically, Eq. (4.7) was computed for a range of values of the STD σ , using $FF_{a,\sigma}^{GG}$ as the FF. Then, the values for σ and a that minimized the Err-function were chosen to be the estimates.

This simulation is interesting because it leads to two estimates: the mean diameter and the STD of the size distribution. In particular, the σ estimate is a new parameter that may carry an interesting property for constructing new QUS images. Obviously, the two-parameter optimization leads to a better fit than would the Gaussian FF (that depends only on a) because when $\sigma \rightarrow 0$ then the Gaussian-Gaussian FF reduces to the Gaussian FF. Thus, in the case where the actual tissue structures follow a narrow size distribution, the Gaussian-Gaussian FF should be able to track it just as well as the Gaussian FF would. However, when there are variations in sizes, the Gaussian-Gaussian FF should lead to improved results (i.e., accurate size estimates without overestimation) and also yield a new quantitative parameter (σ) which can be used to create new QUS images.

The size estimates are shown on Figure 5.5. The estimates are very accurate, all in the range 39.3–40.2 μm . The estimates are slightly underestimating the actual average size (40 μm) with a mean estimate value of 39.7 μm . The STDs of the size estimates are larger than those of Figure 5.4. All the STDs are in the range 1.0–3.5 μm . The larger STDs probably come from the greater difficulty to estimate two parameters from a single random (i.e., noisy) curve. Also, the STD of the estimates increased as a function of STD, just like as shown in Figure 5.4.

The σ estimates are shown on Figure 5.6. The mean values of σ are fairly accurate with a mean error of 1.5%. The STD of the σ estimates are all in the narrow range 1.56–2.20 μm . This range is narrow but error may be quite significant when the actual STD values are small (like for example when STD = 2 μm). This maybe

explained by the fact that the Gaussian-Gaussian FF does not change as much for neighboring values of σ as it does for neighboring values of a .

Nevertheless, the results presented in Figures 5.5 and 5.6 are better than those presented in Figure 5.3. First, the mean size estimates is retrieved accurately, and secondly a fairly good estimate of σ comes for free. In particular, these simulations showed that the Gaussian-Gaussian FF is a valuable extension of the Gaussian FF, because the former converges to the later when $\sigma \rightarrow 0$ and is capable of accurately modeling scattering when $\sigma \neq 0$. Thus, using the Gaussian-Gaussian FF is an advantageous extension of the Gaussian FF. In particular, simulations demonstrated that the Gaussian FF would come up with the same size estimates for an ROI containing a narrow distribution of Gaussian scatterers of size $52 \mu\text{m}$ and for an ROI containing Gaussian scatterers whose size follow a Gaussian distribution of mean $40 \mu\text{m}$ and standard deviation $20 \mu\text{m}$. However, using the Gaussian-Gaussian FF is more computationally extensive because of the computation of Eq. (2.33) whereas the simple form of the Gaussian FF allows for efficient estimation schemes.

5.2 Validation of the 3DZM-FF Extraction

Before deducing FF from 3DZMs as complicated as those obtained for the three tumors, simulations were conducted in order to assess the quality of the methodology to extract a FF from a 3DZM. Simulated 3DZMs were constructed that were divided into N ROIs; N was less than a hundred to limit the computational load of the optimization step of the FF-extraction methodology (Section 4.4).

Each ROI was populated by a random number of Gaussian scatterers following a Gaussian distribution of sizes. Both the average radius a and the standard deviation σ of the size distribution were randomized for each ROI. Each scatterer had an acoustic impedance of 1.51 Mrayl and the background was of 1.50 Mrayl. Also, for all simulations the frequency band was chosen to be 7.66–30.7 MHz which was deduced by computing the frequency from $ka = 0.5$ and $ka = 2$ when $c = 1540 \text{ m/s}$ and for a scatterer radius $a = 16 \mu\text{m}$.

Each set of simulations consisted of a 3-step process. First, N random ROIs following prescribed distributions were generated. Second, a 3DZM-deduced FF was extracted from the N ROIs' power spectra using the methodology presented in Section 4.4. In particular, the extracted FF was confined to the 2-parameter

exponential law $e^{-\alpha(ka)^n}$. Thus, the second step led to values for α and n . Third, the extracted FF was then used with the N available power spectra to obtain estimates following the methodology presented in Section 4.1. Estimates using the Gaussian FF were also conducted. This allowed comparison of the accuracy of the estimates between the deduced FF and the Gaussian FF often used for QUS [32]. Five different simulations were conducted to assess quantitatively the FF-extraction methodology.

The first simulation consisted of 25 ROIs containing a random number of randomly located scatterers. The scatterers within all the ROIs had the same size of $32 \mu\text{m}$ (i.e., $a = 16 \mu\text{m}$). This simulation was meant to test the methodology because in this case the optimal FF is the Gaussian FF. Figure 5.7 shows the actual sizes, the Gaussian size estimates, and the size estimates obtained with deduced FF for each of the 25 ROIs. This figure shows that the accuracy of the estimates is really good; all the size estimates (Gaussian FF and deduced FF) are in the range 29–35 μm (i.e., within 10%). There is no visible difference of quality between the Gaussian estimates and the deduced FF estimates. Some Gaussian estimates are better and some are worse than the deduced FF estimates. The mean errors were $0.81 \mu\text{m}$ and $0.77 \mu\text{m}$ for the Gaussian and deduced FFs, respectively. These results tend to prove that for this simple simulation the FF-extraction algorithm was capable of deriving an accurate FF. Specifically, the α and n parameters found by the FF-extraction algorithm were $\alpha = 0.796$ and $n = 2.08$, which are very near (within 4%) the actual Gaussian values ($\alpha = 0.827$ and $n = 2$).

In the second simulation, the 25 ROIs were random realizations of the same distribution of scatterers, Gaussian scatterers with a Gaussian distribution of size with mean size $32 \mu\text{m}$ (i.e., $a = 16 \mu\text{m}$) and standard deviation $8 \mu\text{m}$. For this case, the theoretical FF is Gaussian-Gaussian with $a = 16 \mu\text{m}$ and $\sigma = \frac{8}{2} = 4 \mu\text{m}$ and is plotted on Figure 2.3. The Gaussian estimates are expected to overestimate the mean size because of the non-zero standard deviation. Estimation results are displayed in Figure 5.8. The Gaussian estimates are greater than the actual mean scatterer size; the mean Gaussian error is $4.8 \mu\text{m}$ (15% error). The deduced FF estimates do not show any bias, some of the estimates are slightly above and some are slightly below $32 \mu\text{m}$. The deduced FF mean error is $0.77 \mu\text{m}$ (less than 3%). The FF-extraction algorithm estimated $\alpha = 1.46$ and $n = 1.66$. These values are within 7% of the values shown in Table 4.2 ($\alpha = 1.54$ and $n = 1.57$) for the Gaussian-Gaussian FF with a

$= 16 \mu\text{m}$ and $\sigma = 4 \mu\text{m}$. This agreement tends to demonstrate the ability of the algorithm to extract the correct FF.

In the third simulation, the 25 ROIs contained scatterers of different random radii but with the same radius within the same ROI (i.e., $\sigma = 0$ for each ROI). This simulation was meant to test the ability of the algorithm to find the correct frequency axis scaling coefficients. In addition, $\sigma = 0$ (for each ROI) makes the assumptions of Section 4.4 valid (e.g., the transition from Eq. (4.10) to Eq. (4.11)). Also, the optimal FF for this simulation is the Gaussian FF because there is no variance in the size of the scatterers within a given ROI. The results are shown in Figure 5.9. For this case also, both FFs led to very accurate estimates even though the actual diameters were randomly selected in the large range $16\text{-}48 \mu\text{m}$. The mean errors were $1.02 \mu\text{m}$ and $1.12 \mu\text{m}$ for the Gaussian and deduced FFs, respectively. Also, the FF-extraction algorithm led to $\alpha = 0.796$ and $n = 2.07$ for this simulation. These values are also within 4% of the actual Gaussian values. Thus, this simulation demonstrated the ability of the FF-extraction algorithm to determine accurate frequency scaling coefficients.

In the fourth simulation, each of the 25 ROIs contained a Gaussian distribution of size where the mean radius was random but the STD σ was 75% of the mean radius. Radii were randomly selected in the large range $8\text{-}24 \mu\text{m}$ (i.e., diameter randomly selected in the range $16\text{-}48 \mu\text{m}$). The goal of this simulation was to test the FF-extraction algorithm in a more challenging case (than the second simulation) where it is known that the Gaussian FF is not a correct model. Theoretically, the FF corresponding to such a distribution was derived in Section 2.3.4 and is not Gaussian. The theoretical FF for this simulation is Gaussian-Gaussian with $a = 16 \mu\text{m}$ and $\sigma = 0.75*16 = 12 \mu\text{m}$ and was plotted in Figure 2.3. For this simulation, it is normal to expect the Gaussian FF to perform poorly and to greatly overestimate the scatterer diameters because of the standard deviation effect. The results are shown in Figure 5.10. For this simulation the Gaussian estimates are always greater than the actual values, i.e., the Gaussian estimates are biased. The mean Gaussian estimate bias (same as error for this case) is $+9.2 \mu\text{m}$ (+29%). On the contrary, the deduced FF estimates seem to have no bias (some estimates are greater and some are less than the actual value) and to be accurate. The mean error for the deduced FF estimates is $1.99 \mu\text{m}$. This mean error is greater than those of the previous three simulations

but is still acceptable (less than 5% mean relative error). Also, the FF-extraction algorithm led to $\alpha = 6.09$ and $n = 0.702$ for this simulation. These numbers are far from the Gaussian FF values, which is normal because the larger standard deviation makes the Gaussian FF an inaccurate model. However, these values are very close (within 7%) to those reported in Table 4.2 for the Gaussian-Gaussian FF when $a = 16 \mu\text{m}$ and $\sigma = 12 \mu\text{m}$ ($\alpha = 6.095$ and $n = 0.752$). Thus, this simulation demonstrated that even in this more challenging case, the FF-extraction algorithm is still capable of performing accurately.

Finally, in the fifth simulation, each of the 25 ROIs contained Gaussian scatterers with a Gaussian size distribution for which both the mean radius and the standard deviation were randomized and independent from one ROI to the next. This is an even more extreme case than that of the fourth simulation because everything is randomized independently. The 25 mean radii were random realizations from a uniform law over the range $8\text{--}24 \mu\text{m}$. The 25 STDs were random realizations from a uniform law between zero and the mean radius for the same ROI. This simulation was meant to assess if the FF-extraction algorithm would be capable of extracting a FF from 25 ROIs that have different size distributions but contain the same scatterers. For this simulation, the Gaussian estimates should be over the actual values, with a bias that depends on the STD of each ROI. The results are shown in Figure 5.11. The Gaussian estimates are greater than the actual values in all except one ROI. The deduced FF estimates are sometimes greater and sometimes smaller than the actual values. The mean errors were $6.29 \mu\text{m}$ and $5.09 \mu\text{m}$ for the Gaussian and deduced FF, respectively. These larger errors (greater than 15%) tend to demonstrate that neither of the two FFs are accurate scattering models. Also, the FF-extraction algorithm led to $\alpha = 3.24$ and $n = 1.04$ for this simulation. The fact that the Gaussian FF produces inaccurate estimates was expected. However, the fact that the deduced FF produces inaccurate estimates was unexpected. The problem may be due to the two-parameter exponential model that is incapable of tracking the three degrees of freedom of the fifth simulation: the random mean radius, the random standard deviation, and the random ROIs. One possible way to mitigate this problem would be to fit the extracted form factor to a model with three or more degrees of freedom. A 3-parameter FF could be derived theoretically by extending further the theory of Section 2.3.4.

These five simulations demonstrated the ability of the FF-extraction algorithm to accurately model complicated scattering media. In particular the 3DZM-deduced FF greatly outperformed the Gaussian FF for these advanced media even though the media were only filled by Gaussian scatterers. This methodology will hence be used on more complicated 3DZMs such as those obtained from tumors.

5.3 Tumor Tissue Characterization Using the Gaussian FF

The first characterization studies involving the 3DZMs deduced from the three tumors consisted of obtaining estimates for the scatterer diameter and the acoustic concentration using the Gaussian FF. The Gaussian FF is a logical choice because it allows for comparison of the 3DZM estimates (i.e., size and acoustic concentration) with the ultrasonic estimates. The ultrasonic estimates were obtained prior to the tumor tissue preparation and are thus independent from those obtained from the 3DZM. The 3DZMs were obtained following a complex set of methodologies including tissue preparation and signal and image processing (Chapter 3). Thus, a way to assess quantitatively the accuracy of the 3DZMs is the comparison of the estimates using the same FF (i.e., Gaussian FF) between the two independent estimation methodologies (3DZM and ultrasound). Therefore, if the 3DZM-derived estimates are similar to the ultrasound estimates this would be an indication of correctness of the 3DZMs.

5.3.1 Rat fibroadenoma results

The 3DZM of the fibroadenoma of size $800 \times 600 \times 190 \mu\text{m}$ was divided into four ROIs, each of size $400 \times 300 \times 390 \mu\text{m}$ (Figure 5.12(b)). Figure 5.12(c) shows the scatterer size estimates and Figure 5.12(d) shows the acoustic concentration estimates for the 4 ROIs obtained using the Gaussian FF. The mammary duct (in red on Figure 5.12(b)) is present in two of the four ROIs, and appears in red in the bottom-right ROI. Also, the top-right ROI contains the mammary duct; however, it cannot be seen in Figure 5.12(b) because it is not contained in the top section. The estimates obtained are very similar for the 2 ROIs that do not contain the mammary duct as well as the bottom-right ROI. The top-right size estimate is the smallest and the top-right concentration is the greatest. This might be due to the presence of the mammary duct. However, a similar effect was not observed in the estimates of the other ROI containing the mammary duct.

The error function (Figure 5.13) contained a few distinct local minima (generally between 1 and 3 depending on the ROI). The estimates were obtained by selecting a minimum that was in the frequency range that was used for the same tumor when evaluated experimentally with ultrasound (-6 dB bandwidth 5-12 MHz) [23].

5.3.2 4T1 mouse mammary carcinoma results

The 3DZM of the 4T1 mouse mammary carcinoma of size $200 \times 150 \times 330 \mu\text{m}$ was divided into four ROIs each of size $100 \times 75 \times 330 \mu\text{m}$ (Figure 5.14(b)). Figure 5.14(c) shows the scatterer size estimates and Figure 5.14(d) shows the acoustic concentration estimates obtained using the Gaussian FF. The estimates are consistent among the four ROIs. However, the top-right ROI has the greatest acoustic concentration (even though it does not have the smallest size estimate). This might be due to the presence of the red blood cells (in red on Figure 5.14(b)) in this ROI.

Here also, the error function (Figure 5.15) contained a few distinct local minima. The estimates were obtained by selecting a minimum that was in the frequency range that was used for the same tumor when evaluated experimentally with ultrasound (-6 dB bandwidth 10-25 MHz) [23]. The top plot shows only one minimum, but the bottom plot shows 4 clear minima. However, for these two ROIs the selected size estimates were $32 \mu\text{m}$ and $34 \mu\text{m}$, respectively.

5.3.3 EHS mouse sarcoma results

The 3DZM of the EHS mouse sarcoma of size $218 \times 156 \times 129 \mu\text{m}$ was divided into four ROIs, each of size $109 \times 78 \times 129 \mu\text{m}$ (Figure 5.16(b)). Figure 5.16(c) shows the scatterer size estimates and Figure 5.16(d) shows the acoustic concentration estimates obtained using the Gaussian FF. The top-right ROI has the smallest estimated diameter ($21 \mu\text{m}$) and the largest acoustic concentration (3.7 dB mm^{-3}). The other three ROIs have similar diameter estimates (near $35 \mu\text{m}$). Surprisingly, the top-right ROI that has a much smaller concentration than the other ROIs, and might be due to the presence of a large vessel in the ROI (white on Figure 5.16(a)), thus leading to a smaller number of scatterers within the ROI. For this tumor also, the estimates were obtained by selecting a minimum in the error function plot (Figure 5.17) that was in the frequency range that was used for the same tumor when evaluated experimentally with ultrasound (-6 dB bandwidth 10-25 MHz) [26].

5.3.4 Comparison with ultrasonic results

The estimates obtained using the 3DZM methodology for the three tumor types were compared to the values obtained ultrasonically [23–26] (Table 5.2). The experimentally derived estimates represent an independent measure from that of the 3DZM estimates. The average scatterer size and acoustic concentration estimates (Table 5.2) were obtained by computing the mean and standard deviation of the estimates over the four ROIs for each of the three tumors. Results show a good agreement (difference less than 10%) for size estimates of all three tumors. However, the acoustic concentration values are significantly different (difference greater than 6 dB mm⁻³).

The 3DZM technique estimates of acoustic concentration were significantly smaller than those obtained ultrasonically (6.3 dB for the rat fibroadenoma, 11 dB for the 4T1 mouse mammary carcinoma, and 10.5 dB for the EHS mouse sarcoma). The difference in estimates might be due to several factors. First, more accurate impedance values may need to be assigned to a wider range of anatomic structures. In particular, a change in the background impedance value (z_0) will significantly modify the acoustic concentration estimates. Second, the internal distribution of acoustic properties (impedance) within the scattering structures will affect the estimates. Third, a small error in the estimate of the scatterer size can lead to a much larger error in the estimate of the acoustic concentration [23]. For example, a relative error of +5% of the scatterer size estimate will lead to a relative error of -27% of the acoustic concentration estimate.

It is encouraging that the scatterer size estimates obtained with the two independent techniques were directly comparable, because the scatterer size depends only on the variation of the power spectrum with frequency. However, the acoustic concentration depends upon the estimated scatterer size and the absolute amplitude value of the power spectrum [23]. The published acoustic concentration estimates determined ultrasonically were used only in a relative comparison. Absolute values for the acoustic concentration estimates were inaccurate because physical reflection losses (skin layer) were uncompensated. The physical reflection losses mostly change the absolute values of the power spectrum but not necessarily its variation with frequency. Therefore, acoustic concentration estimates found using the 3DZM may not be comparable to estimates obtained ultrasonically. The discrepancies

between the ultrasonic and 3DZM acoustic concentration estimates need to be further investigated.

Some of the *Err* curves (e.g., Figures 5.13 and 5.15) showed multiple local minima. The way the scatterer size estimate was selected among the multiple local minima was somewhat empirical. The minimum was selected in the frequency range that was used for the same tumor when evaluated ultrasonically and it is in part why the sizes agreed very well between the 3DZM and ultrasonic estimates. However, these *Err* curves (e.g., Figures 5.13 and 5.15) all tended to have a local minima near the value found ultrasonically demonstrating agreement between the two independent techniques.

To assist with the understanding of the multiple local *Err* minima in the 3DZM-acquired curves, a next step would be to ultrasonically scan tissues over a wider range of frequencies, possibly with multiple transducers. Specifically, multiple minima may correspond to populations of scatterers with different sizes.

5.3.5 Gaussian FF limitations

The size estimates obtained for the three tumors do not allow for statistical distinction between the mouse carcinoma and the mouse sarcoma (Table 5.2). However, the three tumors that were investigated were chosen because they contained very clearly distinct histopathologic features (Figure 5.18). These histologic features are those used by pathologists to diagnose diseases. It is thus disappointing that the ultrasonic tissue characterization (i.e., scatterer size obtained from ultrasound or 3DZM) was unable of clearly distinguishing between the two tumors.

The main explanation for this may be that the Gaussian FF is a poor scattering model that is unable to track the specific ultrasonic scattering properties expected from these two (or three) different tumors. Improved FFs may yield greater sensitivities to the differences between the carcinoma and sarcoma using characterization techniques. Thus, the next logical step in the study was to deduce a tissue-specific FF from each 3DZM and then obtain estimates from these new 3DZM-based FFs. It is reasonable to hypothesize that realistic FFs can be extracted from each of the three 3DZMs that are specific to each tumor, because 3DZMs are acoustic representations of tissue microstructures. Specificity of the FF may then transcribe into statistical differences in the estimates obtained for each tumor.

5.4 Tissue Characterization Using 3DZM-Deduced FF

The first step of the next study consisted in extracting a FF from each of the three 3DZMs. FF-extraction was accomplished following the methodologies of Section 4.4 that were validated by the simulations of Section 5.2. The tissue characterization study conducted using the Gaussian FF showed that it was difficult to differentiate between the carcinoma and sarcoma using the estimates. Thus, one goal of the following study was to assess whether using the 3DZM-deduced FF would allow for distinguishing between the different tumors.

The FF extraction methodology was conducted using 25 ROIs of the same size as the four ROIs used previously for the same tumors (Figures 5.12(b), 5.14(b), and 5.16(b)). Thus, any given two ROIs would have an overlap of less or equal to 75%. The size of each ROI was kept the same for consistency, and 25 ROIs were used because the simulation studies showed that the FF extraction scheme was capable of performing well with 25 ROIs.

For the rat fibroadenoma, the frequency range chosen for the FF extraction was 0.5–15 MHz. For the carcinoma and the sarcoma, the frequency range was chosen to be 1–25 MHz. The frequency ranges were chosen such that they included the bandwidths of the transducer used for ultrasonic evaluation of the same tumor. Also, larger frequencies could be included for the carcinoma and the sarcoma, because the decreased section thickness (5 μm and 3 μm for the carcinoma and the sarcoma, respectively, compared to 10 μm for the fibroadenoma) allowed for more accurate spectra at higher frequencies. Furthermore, one goal of this study was to see if the 3DZM approach could successfully discriminate between the carcinoma and sarcoma; thus, the same frequency range was chosen for both tumor lines.

The FF extraction led to values for the optimal exponential fit (α and n) over the prescribed frequency range (Table 5.3). The values shown for the exponential fit parameters tend to demonstrate that each tumor has a specific FF that is different from that of the other two tumors. Figure 5.19 shows the same feature plot as Figure 4.2 augmented by the three data points corresponding to the three tumors. This figure demonstrates that not only the three 3DZM-deduced FF have different behavior near $ka = 1$ but also that they are different from the other seven FFs introduced in Chapter 2. Thus, it is natural to expect differences in the computed values for the average size and acoustic concentration: the estimation routine was

conducted using the new deduced FF for each tumor.

5.4.1 Rat fibroadenoma results

For the rat fibroadenoma the FF-extraction methodology led to an exponential FF fit with $\alpha = 1.501$ and $n = 0.6145$. Figure 5.12(e) shows the scatterer size estimates and Figure 5.12(f) shows the acoustic concentration estimates obtained using the deduced FF. Estimates were compared to those obtained using the Gaussian FF (Figure 5.12(c) and (d)). For the fibroadenoma the size estimates did not change much when using the deduced FF except for the top right ROI whose size estimate significantly increased from $57 \mu\text{m}$ to $91 \mu\text{m}$. Consequently, the acoustic impedance of the top-right ROI significantly decreased from -13.1 dB mm^{-3} to -19.3 dB mm^{-3} . The change in the estimates shown for the top-right ROI may be due to the presence of the mammary duct in that ROI and how it is tracked by the deduced FF. The only other remarkable change is the increase in acoustic impedance in the bottom left ROI from -23.3 dB mm^{-3} to -16.3 dB mm^{-3} . This increase may be a consequence of the decrease in size estimate for the same ROI (from $95 \mu\text{m}$ to $80 \mu\text{m}$). Nevertheless, the estimates obtained using the deduced FF are not statistically different from those obtained using the Gaussian FF (Table 5.2).

5.4.2 4T1 mouse mammary carcinoma results

For the carcinoma the FF-extraction methodology led to an exponential FF fit with $\alpha = 2.3591$ and $n = 0.4054$. Figure 5.14(e) shows the scatterer size estimates and Figure 5.14(f) shows the acoustic concentration estimates obtained using the deduced FF. Estimates were compared to those obtained using the Gaussian FF (Figure 5.14(c) and (d)). The size estimates obtained are much larger than those obtained using the Gaussian FF except for the top-right ROI whose scatterer size slightly decreased from $32 \mu\text{m}$ to $31 \mu\text{m}$. Consequently all the acoustic concentration values decreased except for the top-right ROI which significantly increased from -7.6 dB mm^{-3} to 0.9 dB mm^{-3} . This global increase in size estimates may indicate that the deduced FF is describing structures larger than the Gaussian FF was. Finally, it is worth mentioning that the new size estimates are statistically different from those obtained using the Gaussian FF (Table 5.2). However, the large standard deviation obtained for the estimates may be due to the model being specific to a certain structures that may not exist in one of the ROI, thus leading to an inaccurate

size estimate.

5.4.3 EHS mouse sarcoma results

For the sarcoma the FF-extraction methodology led to an exponential FF fit with $\alpha = 1.0697$ and $n = 1.5797$. Figure 5.16(e) shows the scatterer size estimates and Figure 5.16(f) shows the acoustic concentration estimates obtained using the deduced FF. Estimates were compared to those obtained using the Gaussian FF (Figure 5.16(c) and (d)). The estimates all changed but stayed very similar on average. For the top-left ROI the size estimates doubled, while for the bottom ROIs it only increased by a few micrometers. For the top-right ROI is significantly decreased from $34 \mu\text{m}$ to $20 \mu\text{m}$. Logically, the acoustic concentration estimates follow the opposite trend. However, the mean estimates are very similar to those obtained with the Gaussian FF (Table 5.2). It may mean that the deduced FF is tracking different structures because the estimates of all the ROIs changed but were of similar size because the average estimates are similar.

5.4.4 Ultrasonic characterization

The deduced FF study led to very interesting results. First, the exponential fit FFs deduced using the FF extraction methodology are different for each tumor. This difference may mean that each tumor has its own ultrasonic scattering signature. Thus, there exists hope that this tumor-specific signature may be used to characterize, distinguish and possibly diagnose disease with quantitative ultrasonic techniques.

Another property demonstrated by the results is that using the deduced FF the average diameter estimate is now statistically specific for each of the three tumors (Table 5.2). The specificities of the estimates are obviously interesting for diagnosis of tissue pathology without the need for an invasive procedure (i.e., biopsy).

However, even though we were capable of extracting tissue-specific FFs that led to statistical differences between the estimates obtained for each tumor, there still exists some limitations to the potential clinical use of these QUS methodologies. For example, it seems possible to design a look up table of tissue-specific FF which could be saved in the memory of a clinical scanner. But, if the goal is a diagnosis of breast tumor, then no indication would be available to decide which FF should be used clinically. An approach would consist in trying several tissue-specific (or disease-specific) FFs and assess the goodness of fit to decide which of these is the most

accurate scattering model. This would provide an indication of a potential diagnosis because the selected FF is an ultrasonic scattering model specific to a certain disease. Furthermore, estimates could then be obtained using this FF and maybe advancement and seriousness of the disease could be assessed using the estimates. Thus, QUS methodologies may become a significant adjunct to conventional methodologies for detection, diagnosis and monitoring of diseases as serious as breast cancer.

5.5 Tables and Figures

Table 5.1 Simulation estimates.

	Medium A	Medium B
Diameter in μm (% error)	41.1 ± 2.9 (2.8%)	81.1 ± 6.1 (1.4%)
Concentration in dB mm^{-3} (% error)	-14.28 ± 1.1 (2%)	-13.88 ± 1.2 (0.8%)

Table 5.2 Three-dimensional impedance map and ultrasound estimates. Ultrasound (US) estimates were obtain using the Gaussian FF. 3DZM estimates were obtained using the Gaussian (G.) and the 3DZM-deduced (D.) FF.

	Rat fibroadenoma		Mouse carcinoma		Mouse sarcoma	
	Diameter μm	Conc. dB mm^{-3}	Diameter μm	Conc. dB mm^{-3}	Diameter μm	Conc. dB mm^{-3}
US	105 ± 25	-15.6 ± 5	30.0 ± 9.6	10.6 ± 6.9	33.0 ± 8.0	9.9 ± 5.3
3DZM G.	91.5 ± 25	-21.9 ± 6.1	31.5 ± 2.5	-1.4 ± 6.1	32.9 ± 6.1	-0.59 ± 4.3
3DZM D.	96.5 ± 14	-21.8 ± 5.1	56.0 ± 19	-6.9 ± 7.2	37.0 ± 12	0.46 ± 5.5

Table 5.3 Parameters and frequency range of the exponential fit obtained using the FF extraction methodology. Exponential fit parameters were extracted from the 3DZMs displayed on Figures 5.12(b), 5.14(b), and 5.16(b).

	Frequency range (MHz)	α	n
Rat fibroadenoma	0.5–15	1.501	0.6145
Mouse carcinoma	1–25	2.359	0.4054
Mouse sarcoma	1–25	1.070	1.580

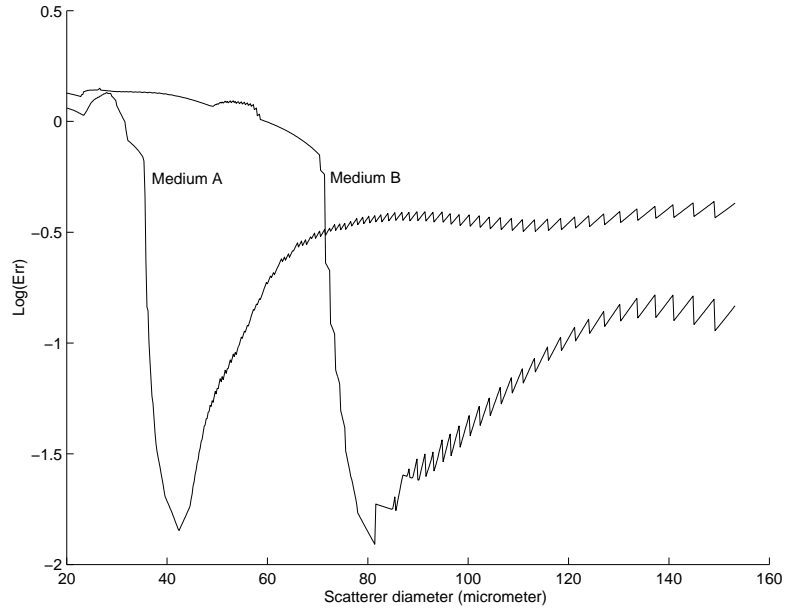


Figure 5.1 $\text{Log}(Err)$ versus scatterer diameter for realizations of media A and B.

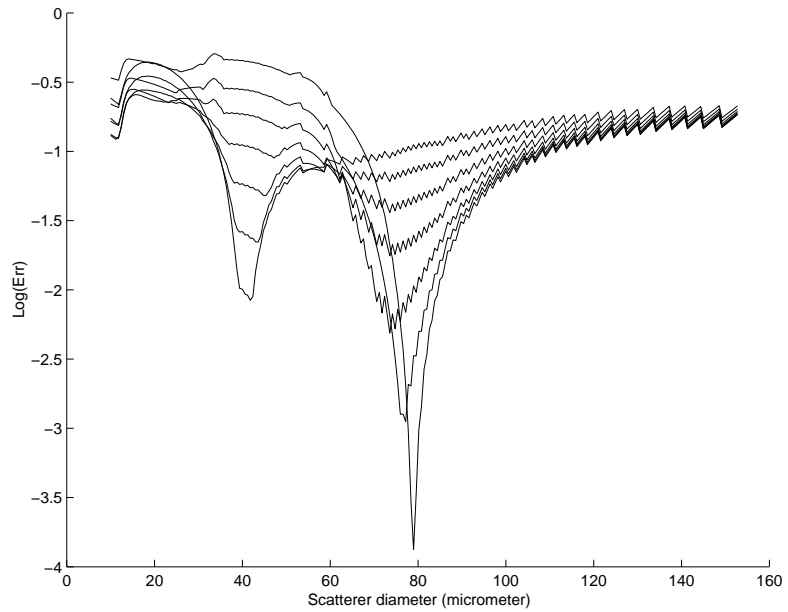


Figure 5.2 $\text{Log}(Err)$ versus scatterer diameter for realizations of two-population media. The acoustic concentration of the 40- μm scatterers was constant at $-14.01 \text{ dB mm}^{-3}$. The acoustic concentrations of the 80- μm scatterers were (from top to bottom at the horizontal axis location of about 40 μm): $-9.01, -14.01, -17.01, -20.01, -23.01, -26.01$, and $-29.01 \text{ dB mm}^{-3}$.

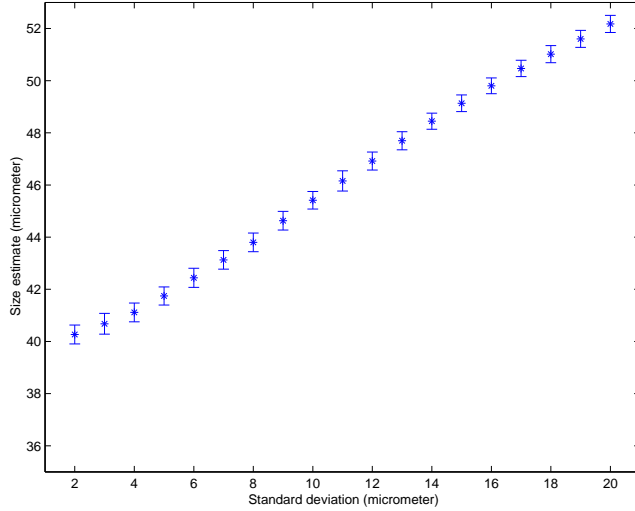


Figure 5.3 Size estimates obtained using a Gaussian FF. The simulated 3DZM contained Gaussian scatterers whose size distribution was Gaussian with a mean of $40 \mu\text{m}$. The STD of the size distribution varied from $2 \mu\text{m}$ to $20 \mu\text{m}$ by $1 \mu\text{m}$ increments. For each STD value, 64 3DZMs were generated. Error bars represent STDs of estimates.

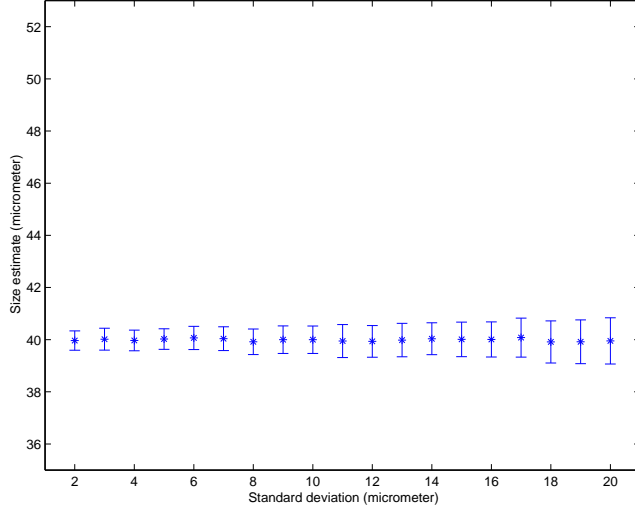


Figure 5.4 Size estimates obtained using a Gaussian-Gaussian FF assuming σ is known. The simulated 3DZM contained Gaussian scatterers whose size distribution was Gaussian with a mean of $40 \mu\text{m}$. The STD of the size distribution varied from $2 \mu\text{m}$ to $20 \mu\text{m}$ by $1 \mu\text{m}$ increments. For each STD value, 64 3DZMs were generated. Error bars represent STDs of estimates.

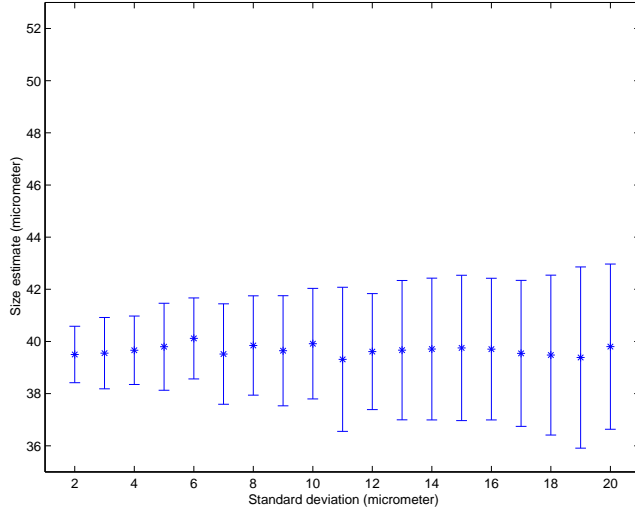


Figure 5.5 Size estimates obtained using a Gaussian-Gaussian FF. The simulated 3DZM contained Gaussian scatterers whose size distribution was Gaussian with a mean of $40 \mu\text{m}$. The STD of the size distribution varied from $2 \mu\text{m}$ to $20 \mu\text{m}$ by $1 \mu\text{m}$ increments. For each STD value, 64 3DZMs were generated. Error bars represent STDs of estimates.

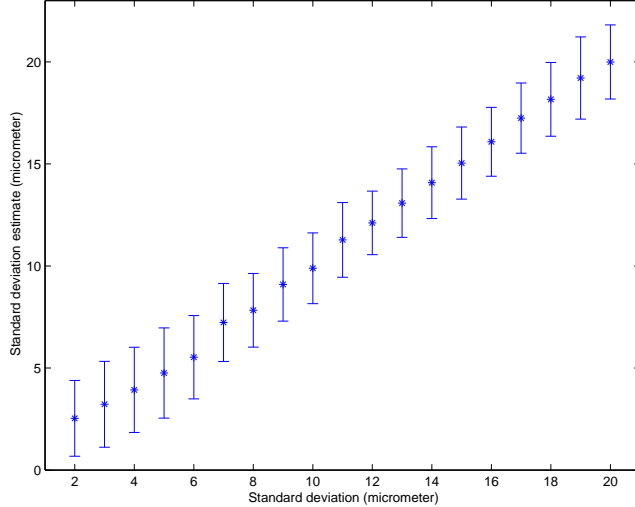


Figure 5.6 Standard deviation estimates obtained using a Gaussian-Gaussian FF. The simulated 3DZM contained Gaussian scatterers whose size distribution was Gaussian with a mean of $40 \mu\text{m}$. The STD of the size distribution varied from $2 \mu\text{m}$ to $20 \mu\text{m}$ by $1 \mu\text{m}$ increments. For each STD value, 64 3DZMs were generated. Error bars represent STDs of estimates.

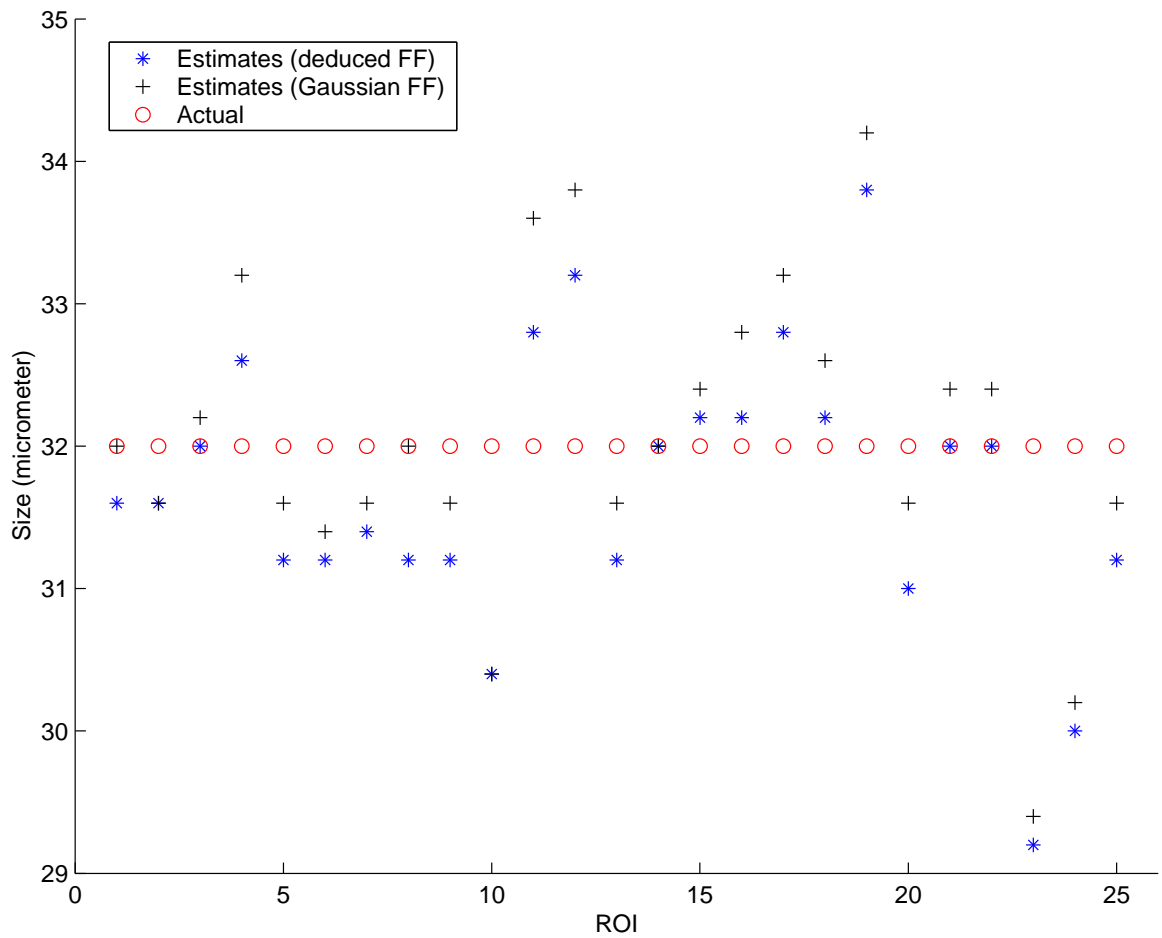


Figure 5.7 Estimates obtained from 25 ROIs using the Gaussian and the 3DZM-deduced FF. Each ROI was filled with a random number of randomly located Gaussian scatterers. Each ROI contained scatterers of diameter $32 \mu\text{m}$.

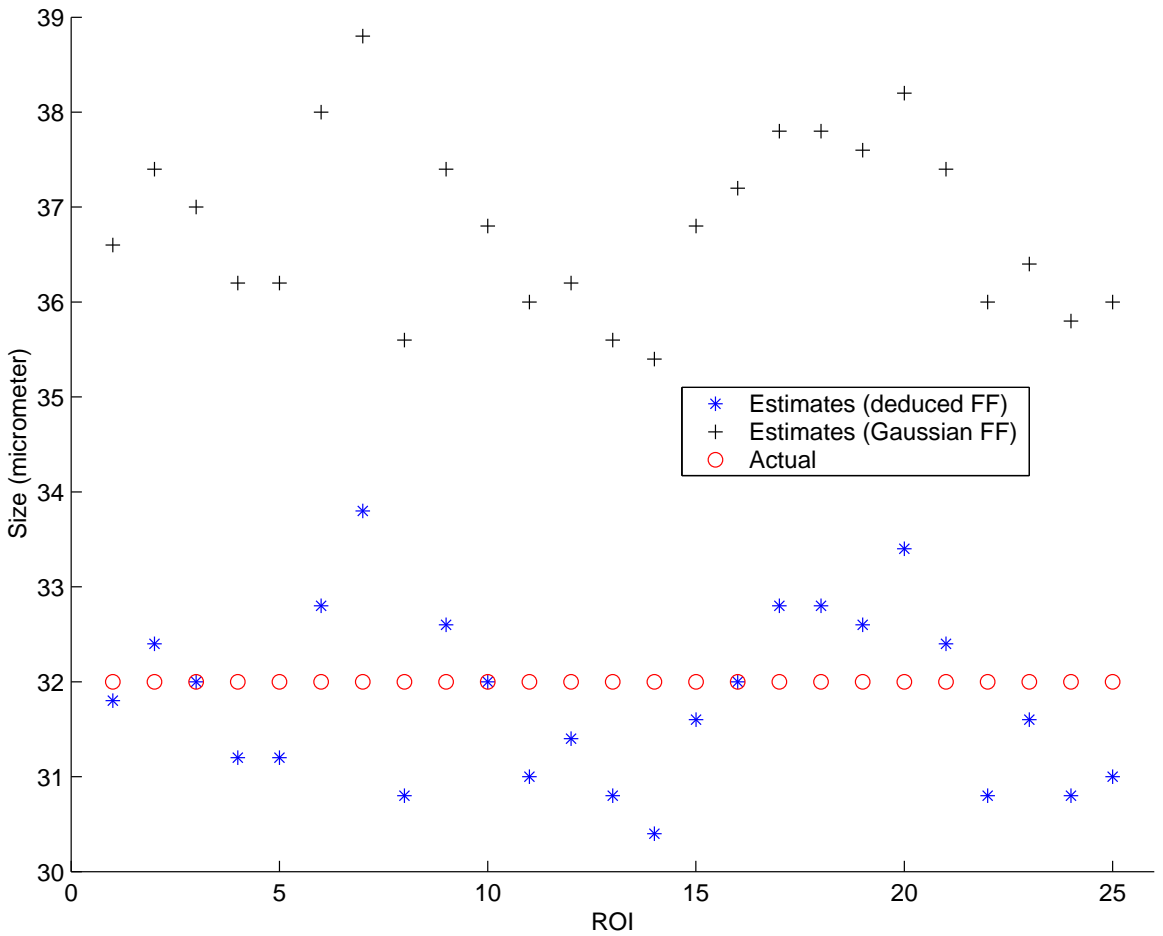


Figure 5.8 Estimates obtained from 25 ROIs using the Gaussian and the 3DZM-deduced FF. Each ROI was filled with a random number of randomly located Gaussian scatterers. Each ROI contained scatterers following a Gaussian size distribution with mean diameter of $32 \mu\text{m}$ and standard deviation of $8 \mu\text{m}$.

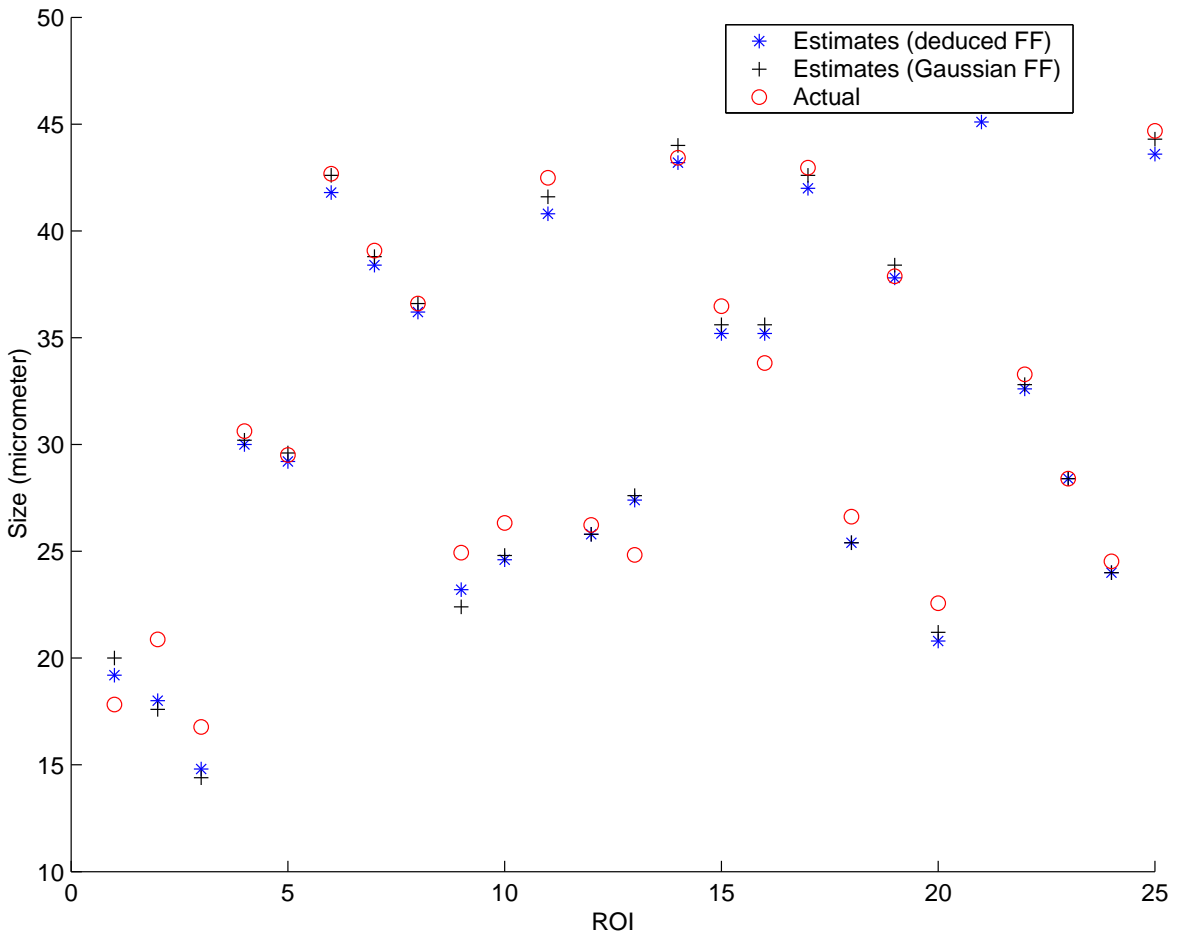


Figure 5.9 Estimates obtained from 25 ROIs using the Gaussian and the 3DZM-deduced FF. Each ROI was filled with a random number of randomly located Gaussian scatterers. Each ROI contained scatterers of the same size. For each ROI, the scatterers diameter was chosen randomly in the range 16–48 μm .

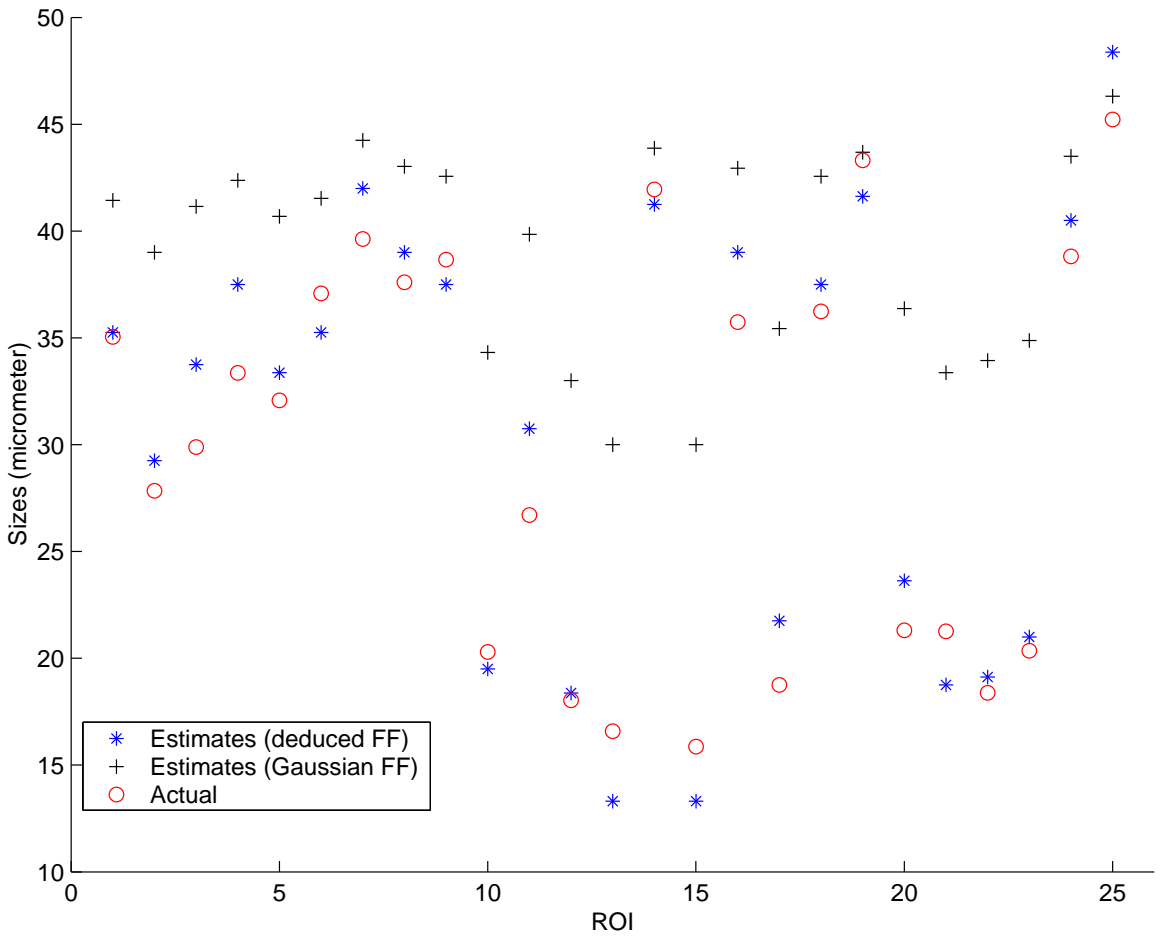


Figure 5.10 Estimates obtained from 25 ROIs using the Gaussian and the 3DZM-deduced FF. Each ROI was filled with a random number of randomly located Gaussian scatterers. Each ROI contained scatterers following a Gaussian size distribution. For each ROI, the scatterers mean diameter was chosen randomly in the range 16–48 μm and the standard deviation was 75% of the mean diameter.

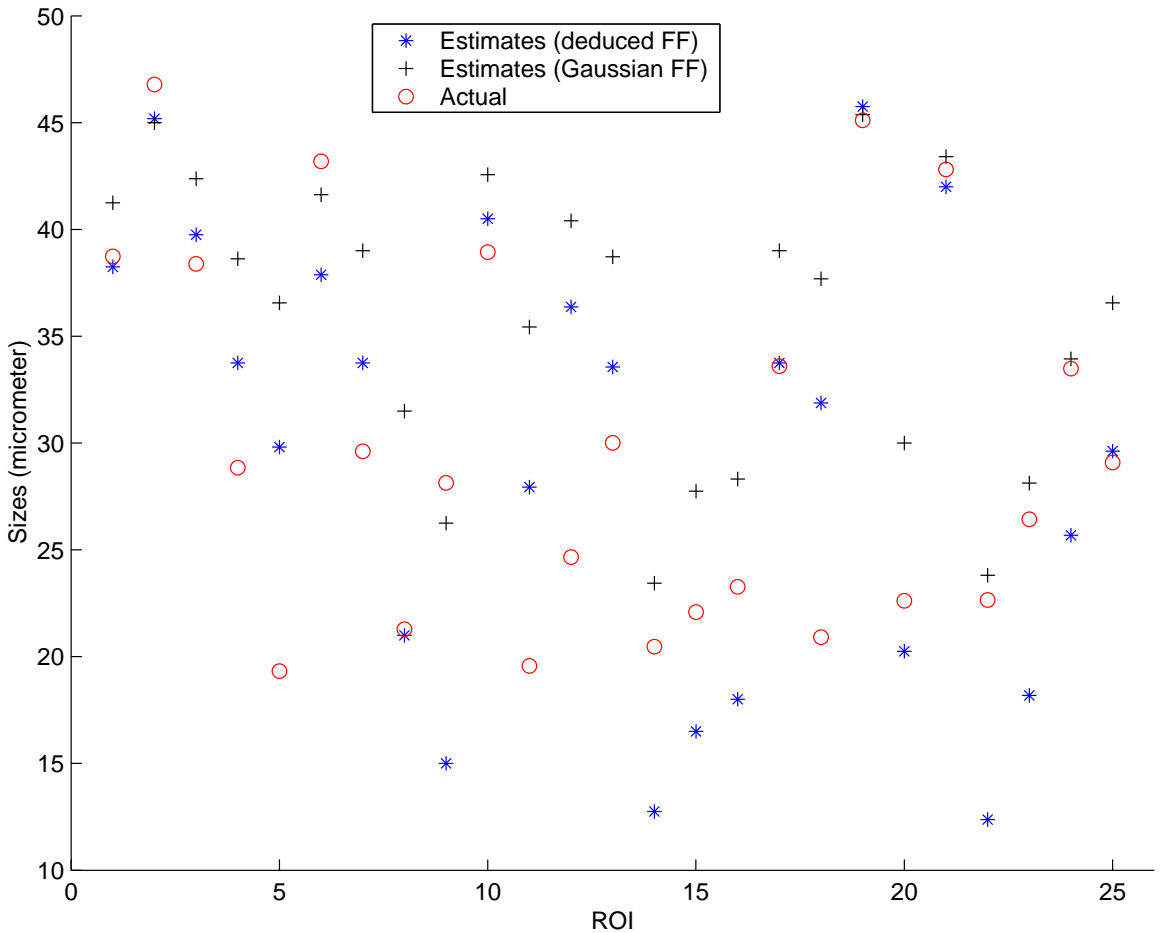


Figure 5.11 Estimates obtained from 25 ROIs using the Gaussian and the 3DZM-deduced FF. Each ROI was filled with a random number of randomly located Gaussian scatterers. Each ROI contained scatterers following a Gaussian size distribution. For each ROI, the scatterers mean diameter was chosen randomly in the range 16–48 μm . The standard deviation was randomly chosen of between 0 and the mean diameter.

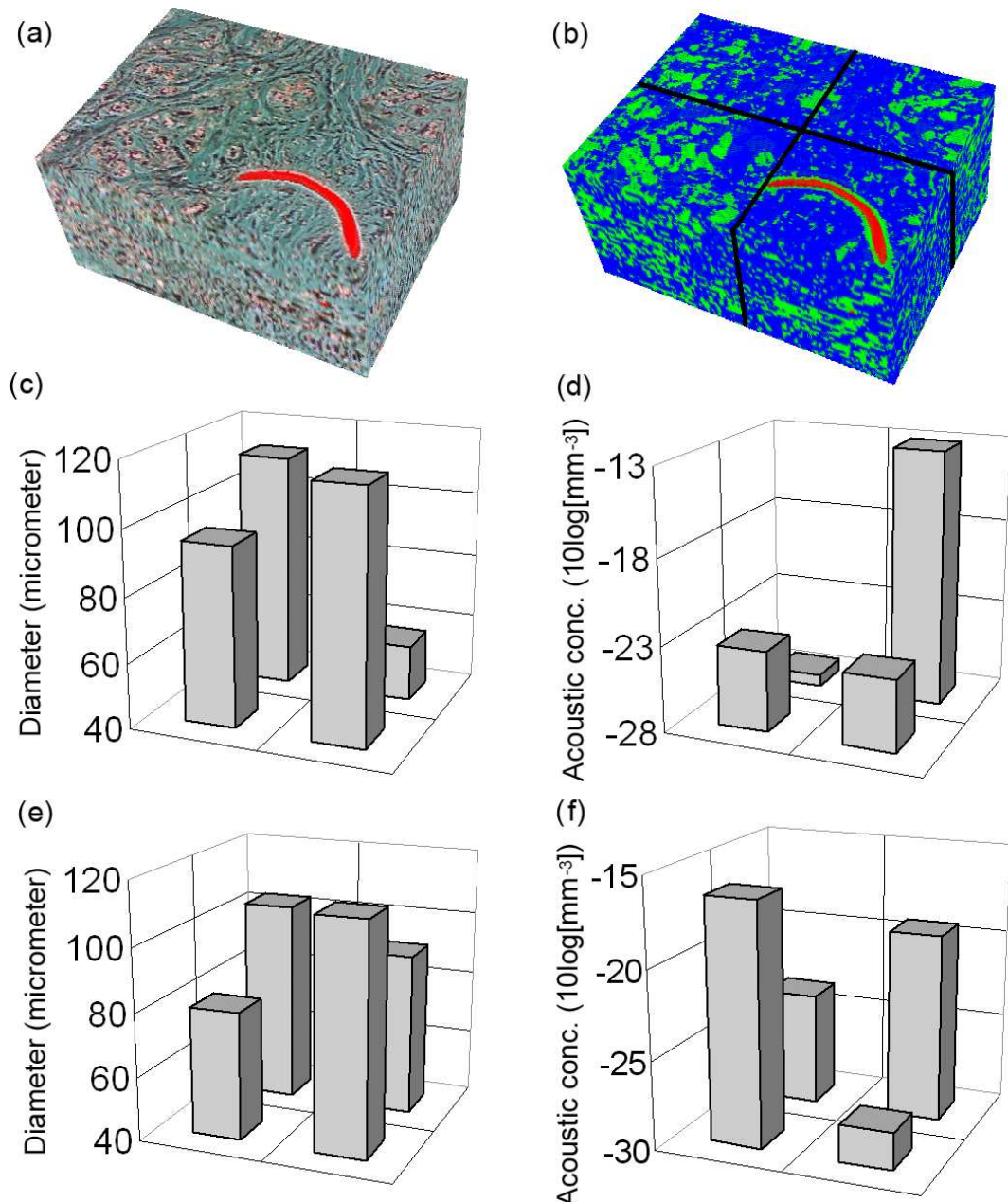


Figure 5.12 (a) Three-dimensional H&E-stained histology of a fibroadenoma. (b) Derived 3D impedance map; black lines show the four ROIs. (c) Estimated scatterer diameter using the Gaussian FF. (d) Estimated acoustic concentration using the Gaussian FF. (e) Estimated scatterer diameter using the 3DZM-deduced FF. (f) Estimated acoustic concentration using the 3DZM-deduced FF. The volumes shown in (a) and (b) are of size $800 \times 600 \times 390 \mu\text{m}$.

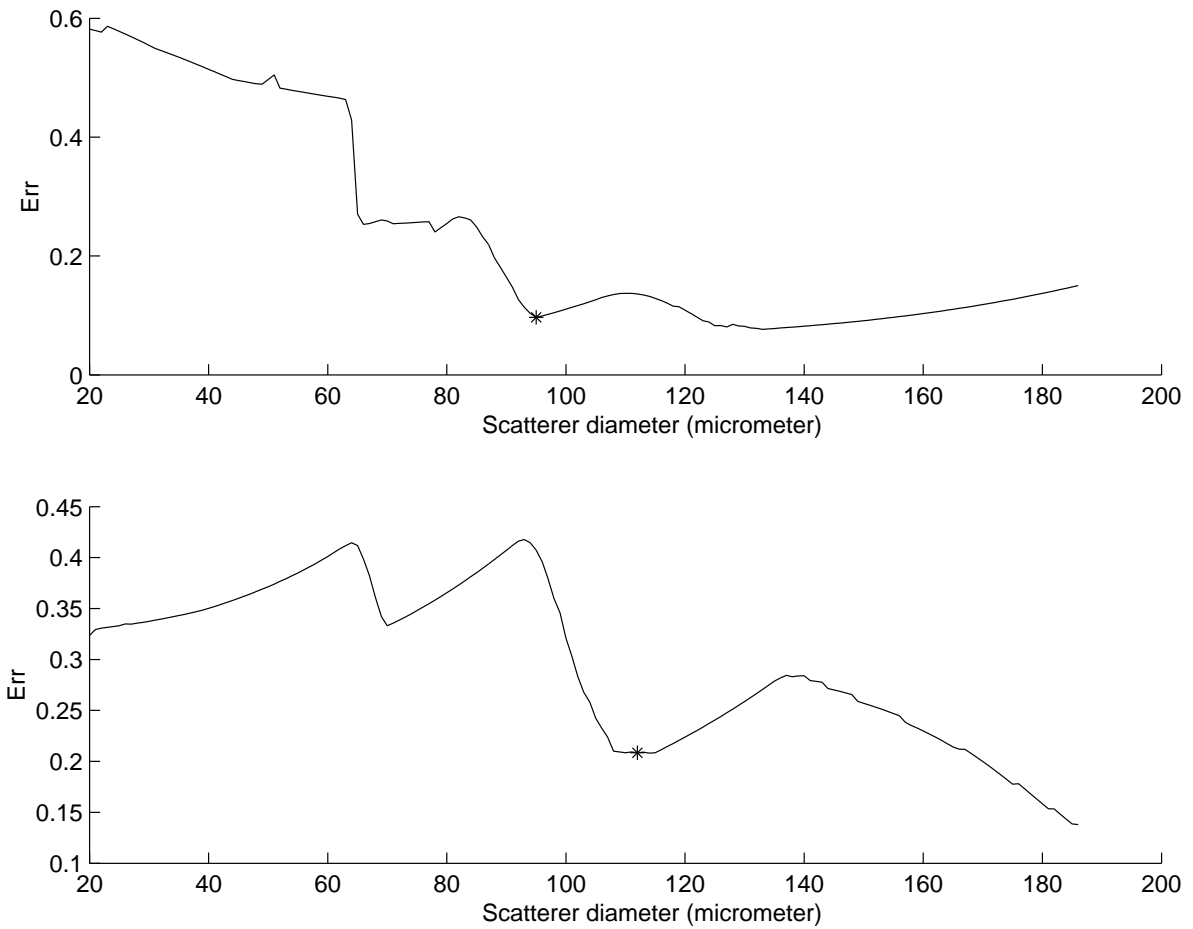


Figure 5.13 Err function versus scatterer diameter obtained from two different ROIs of the rat fibroadenoma. Top curve was obtained from the top-left ROI of Figure 5.12(b) and bottom curve was obtained from the top-right ROI of Figure 5.12(b). The asterisk shows the selected minimum for each ROI.

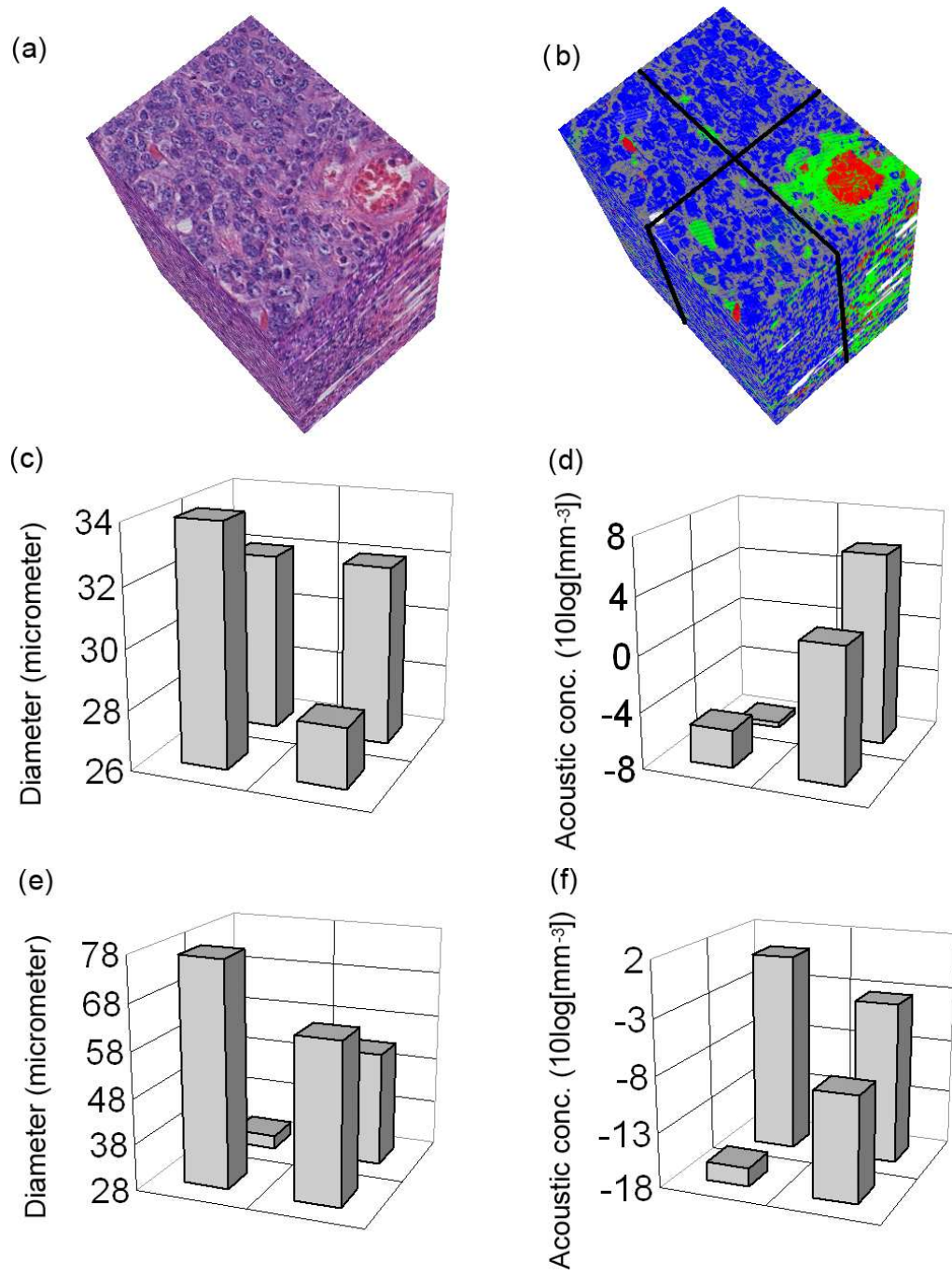


Figure 5.14 (a) Three-dimensional H&E-stained histology of a 4T1 mouse mammary carcinoma. (b) Derived 3D impedance map; black lines show the four ROIs. (c) Estimated scatterer diameter using the Gaussian FF. (d) Estimated acoustic concentration using the Gaussian FF. (e) Estimated scatterer diameter using the 3DZM-deduced FF. (f) Estimated acoustic concentration using the 3DZM-deduced FF. The volumes shown in (a) and (c) are of size $200 \times 150 \times 330 \mu\text{m}$.

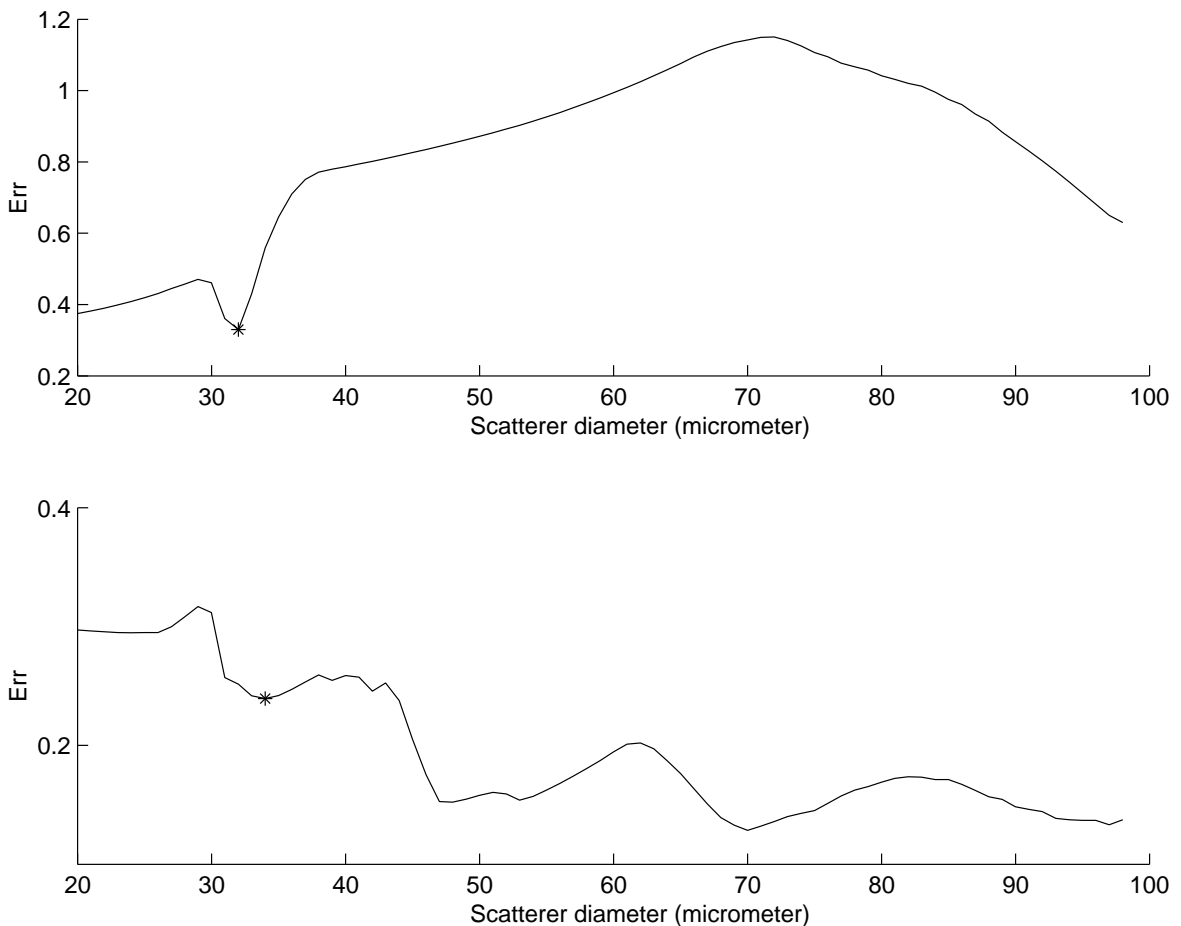


Figure 5.15 Err function versus scatterer diameter obtained from two different ROIs of the 4T1 mouse mammary carcinoma. Top curve was obtained from the top-left ROI of Figure 5.14(b) and bottom curve was obtained from the bottom-left ROI of Figure 5.14(b). The asterisk shows the selected minimum for each ROI.

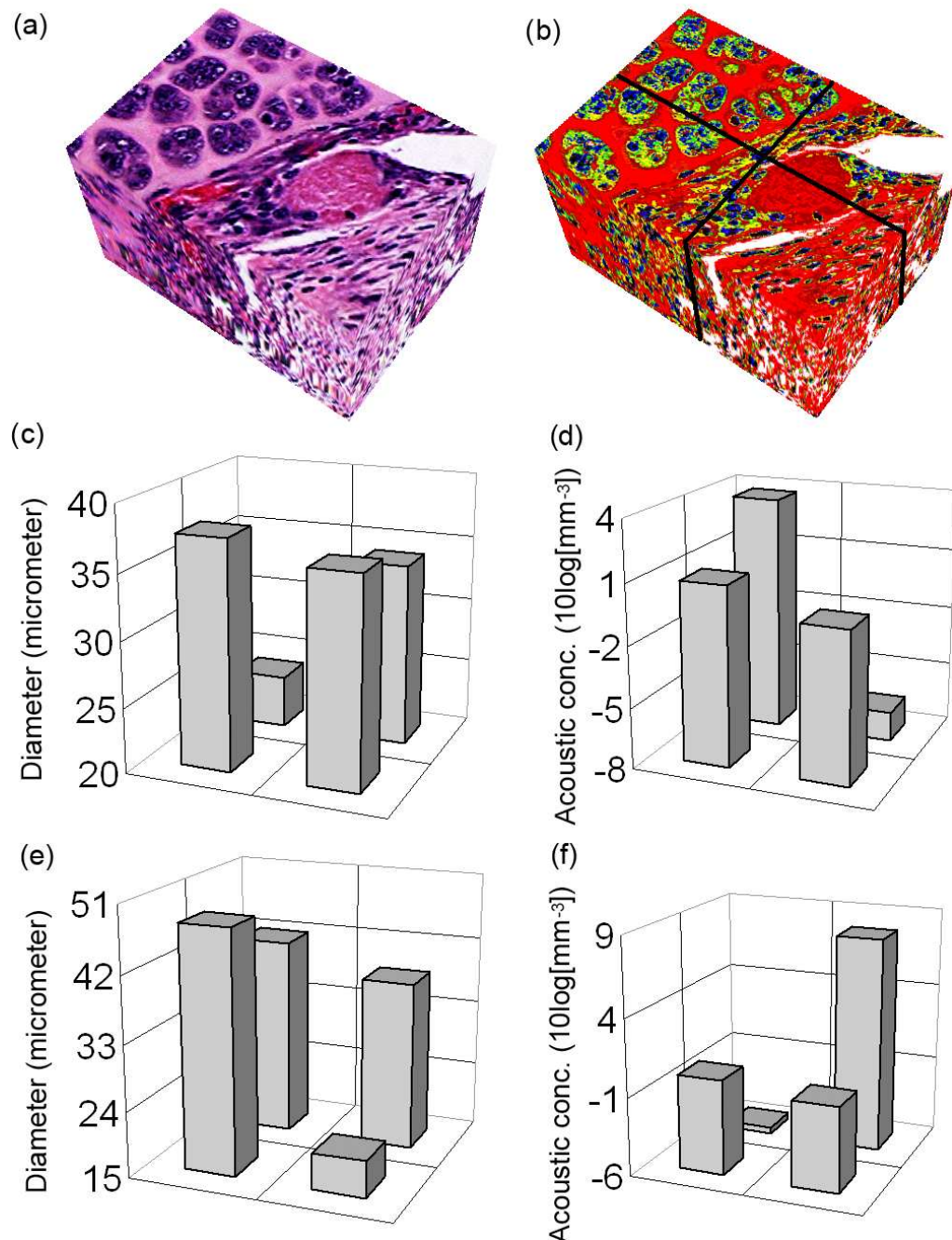


Figure 5.16 (a) Three-dimensional H&E-stained histology of an EHS mouse sarcoma. (b) Derived 3D impedance map; black lines show the four ROIs. (c) Estimated scatterer diameter using the Gaussian FF. (d) Estimated acoustic concentration using the Gaussian FF. (e) Estimated scatterer diameter using the 3DZM-deduced FF. (f) Estimated acoustic concentration using the 3DZM-deduced FF. The volumes shown in (a) and (b) are of size $218 \times 156 \times 129 \mu\text{m}$.

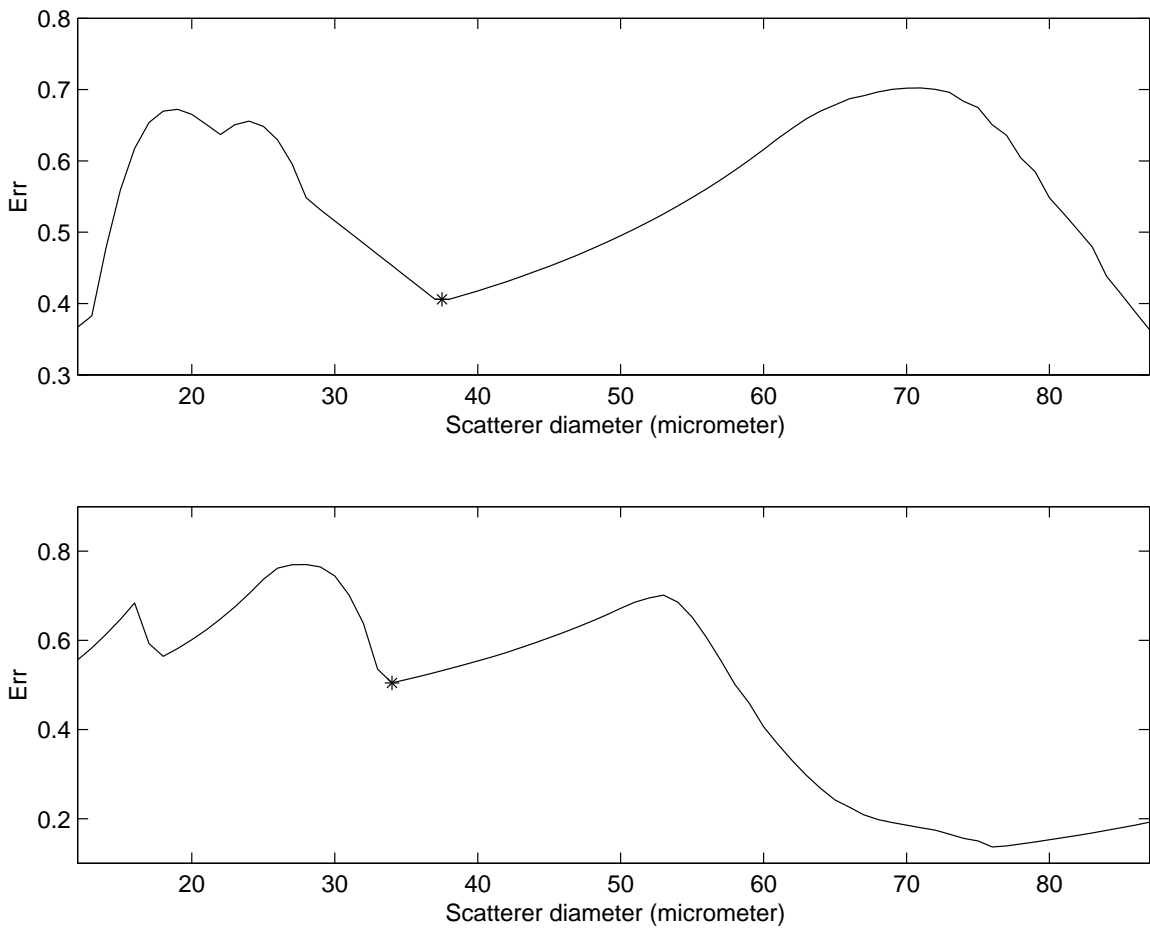


Figure 5.17 Err function versus scatterer diameter obtained from two different ROIs of the EHS mouse sarcoma. Top curve was obtained from the top-right ROI of Figure 5.16(b) and bottom curve was obtained from the bottom-left ROI of Figure 5.16(b). The asterisk shows the selected minimum for each ROI.

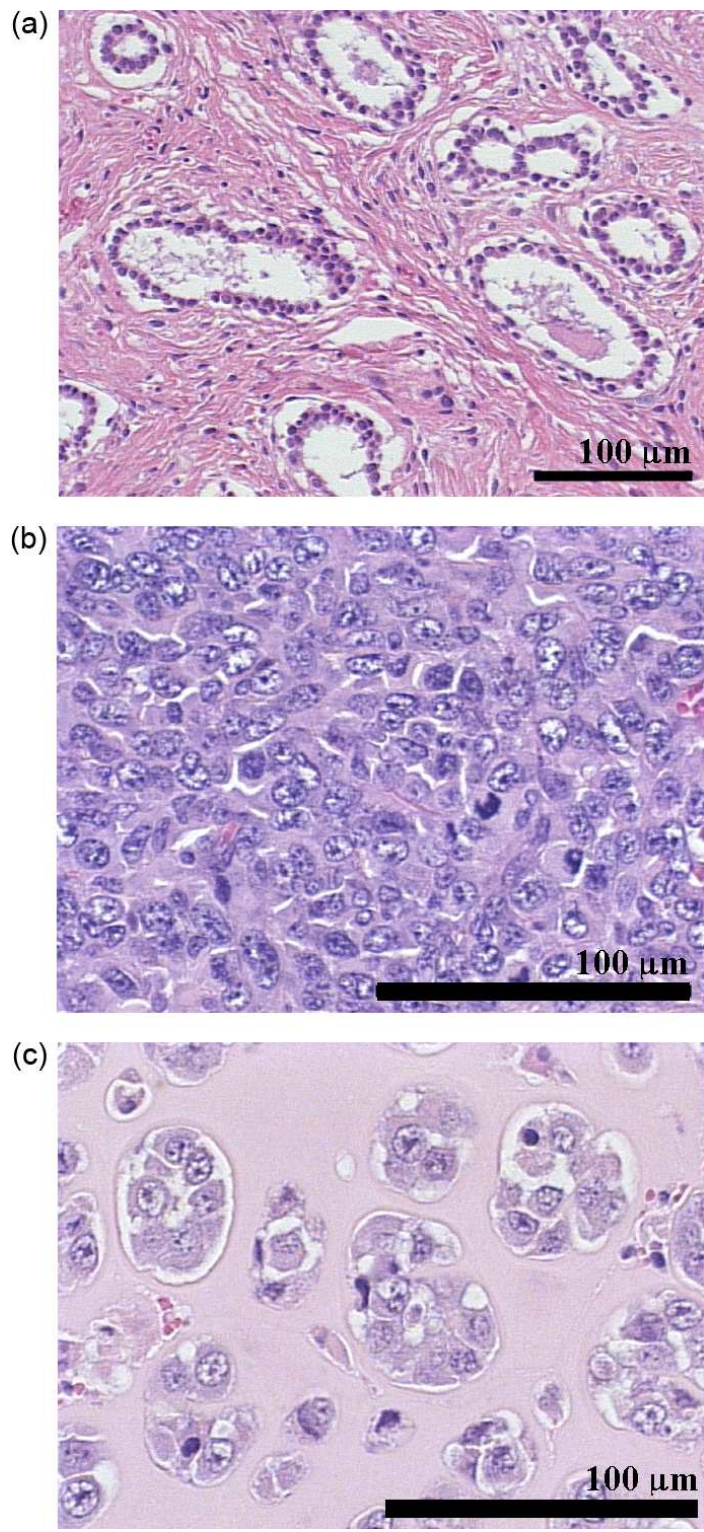


Figure 5.18 Typical H&E stained tissue sections for a rat fibroadenoma (a), a 4T1 mouse mammary carcinoma (b), and a EHS mouse sarcoma (c). This figure demonstrates that the histopathologic properties of the tumor tissue investigated are very different.

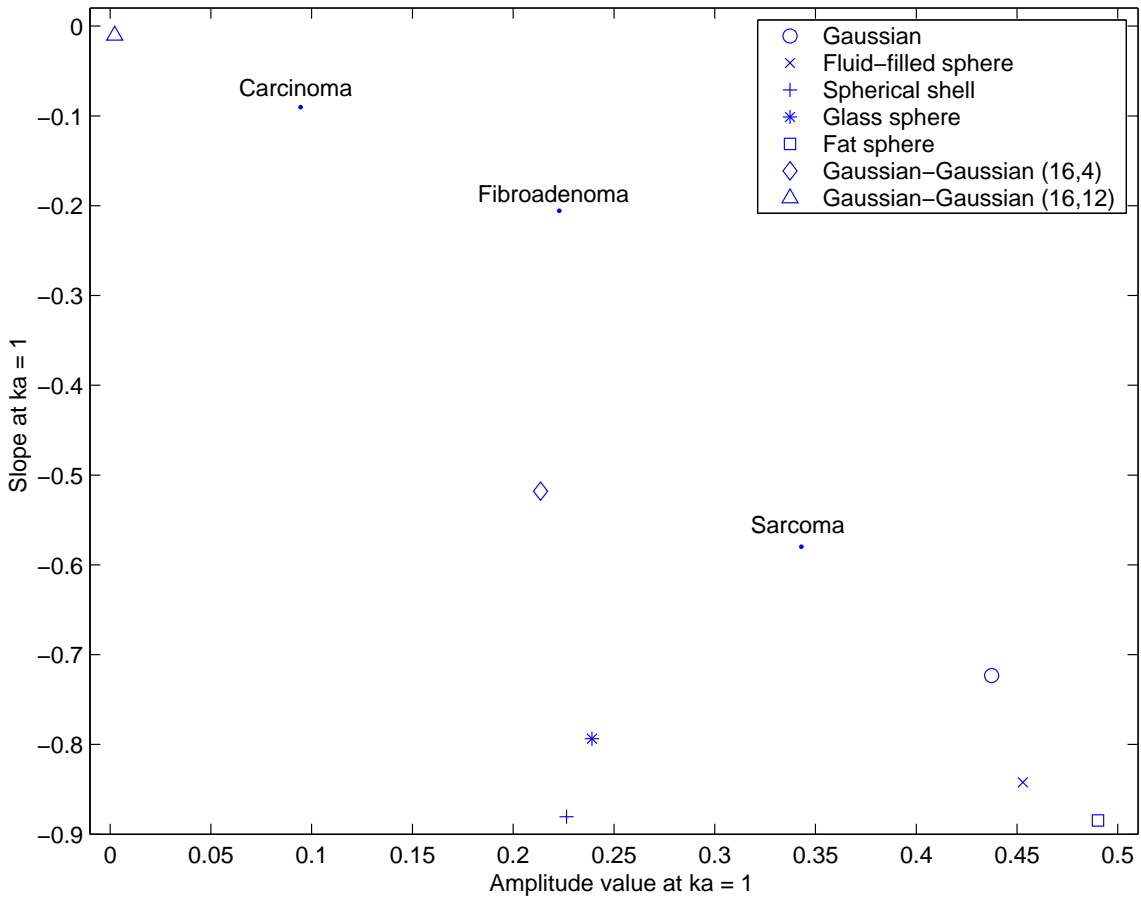


Figure 5.19 Feature plot deduced from the optimal parameters of the exponential model fit for the seven FFs introduced in Chapter 2 and the three 3DZM-deduced FF. For each FF, the feature plot displays the value and the slope of exponential model fit at $ka = 1$. For the Gaussian-Gaussian FFs, the numbers between parentheses are the values used for a and σ in Eq. (2.33) in micrometer.

CHAPTER 6

CONCLUSIONS AND FUTURE WORK

During the course of this dissertation research work, several strategies were developed to obtain and use 3D acoustic tissue models to help in the development of new ultrasonic tissue characterization techniques. In this final chapter, the conclusions derived are summarized and possible future extensions are presented.

6.1 Three-Dimensional Modeling Strategies

Chapter 3 demonstrated the possibility to reconstruct in an automated manner 3D histologic volumes and 3DZM from a stack of 2D histologic sections. Reconstruction strategies were developed in order to compensate for the imperfections expected in the 2D histology stack.

6.1.1 Improvement of the modeling strategies

The modeling strategies are sufficiently general that they can be adapted to reconstruct 3D volumes from other 2D imaging modalities. Thus, each signal/image processing step of the 3D reconstruction could be adapted towards application-specific goals. For example, computational efficiency was not considered critical in this study because the 3D reconstruction needed to be performed only once for each tumor. However, if numerous 3D reconstructions were needed to be obtained in a timely manner, computational efficiency would need to be addressed and improved. In particular, transformations during registration could be done faster by considering spectral methods for fast rotations, translations and scaling [59]. Interpolation speed during registration could also be increased by using Fourier transform methods [60]. On the other hand, if the quality of the reconstruction was critical, then the interpolation methodologies used for registration and to interpolate the missing sections could be improved. For example, higher-order kernel or different cubic kernels could be used for interpolation during registration [49]. Missing section interpolation could also be improved by not transforming the available dataset in several 1D signals.

This will allow the pixels of a missing section or sections to be interpolated not only based on the same pixel from the previous and following sections but also on neighboring pixels [61, 62].

Furthermore, the similarity measure can be engineered to be application specific. Many similarity criteria are available, like the mean-squared difference, the mean absolute difference, the correlation or more advanced measures like the ratio image uniformity [37, 63] or the robust correlation coefficients [64]. Some of these measures are faster to compute and also may track changes in images differently than the NMI, leading to task-specific or tissue-specific measures.

However, none of these techniques are perfect and all have their advantages and disadvantages. Appropriate evaluation would need to be conducted in order to determine which technique is the best for a given task. Specifically, 2D sections may originate from many different modalities leading to different types of artifacts. Therefore, it is natural to assume that the 3D reconstruction techniques that would provide the best results are task specific.

6.1.2 Extensions of the modeling strategies

The 3D modeling methodologies presented in Chapter 3 can be used in numerous fields for diverse applications. Images of 3D renderings are of interest for display and visualization because they clearly show relationships between cells and tissues and the vascular system on a 3D basis. At present, 3D renderings are not used by pathologists, and 2D stained histologic sections are usually considered as the gold standard for diagnosis. However, 3D visualization of tumor expansion and invasion and how such processes occur at the margins of “normal” tissue are invaluable in establishing a histopathologic diagnosis of the tumor and in understanding the basic experimental mechanisms of tumor growth and metastasis.

An additional significant benefit of 3D histologic volumes occurs because they represent 3D volumes of data that can be used as computational phantoms. For example, from 3D histologic volumes, quantitative analyses may be conducted that are not possible from individual 2D sections. The possibility to measure length, area and volume of structures accurately is a valuable diagnostic adjunct to the 2D sections. Pathologists assess diseases on specific criteria, some of which include absolute size of structures (e.g., tumors). Tumor volumes are difficult to estimate from a 2D section or even several consecutive 2D sections. However, 3D

segmentation algorithms could be applied to extract the tumor volume. Thus, accurate tissue registration and 3D histological volume reconstruction are critical for quantitative histopathology. A study recently demonstrated the usefulness of 3D histological volumes for cancer diagnosis [65]. Furthermore, the possibility, for example, of extracting an oblique section from a 3D histologic volume is illustrated in Appendix D. Oblique sections are new 2D histologic sections that can be readily evaluated by pathologists.

Tissue registration and reconstruction of a 3D histological volume are also a necessity for the biological intelligence community. For example, developmental biology tries to elucidate the mechanisms that are responsible for form and function. Thus, an accurate 3D morphological model for the developing embryo might yield new insights. To achieve this challenging goal, it is in part necessary to carefully account for misalignment and distortion of the adjacent 2D images. Accounting for these may be done by adapting the methodologies presented in Chapter 3 for the specificities of this task. The inherent problems of these datasets (i.e., misalignment and distortion) are very similar to those seen in the sarcoma dataset. A recent contribution showed that it may be possible to mitigate these issues by conducting fluorescence imaging of the tissue volume prior to sectioning [66]. Furthermore, developmental biology is interested in the possibility to extract oblique sections from these 3D volumes. Oblique sections allow the use of an optimal view to follow the growth of a specific embryo's organ. The possibility to easily extract oblique sections from a reconstructed 3D volume was demonstrated (Appendix D), and can thus be helpful to the developmental biology community.

The image registration strategies could also be helpful for disease monitoring. For example, even though 3D MRI (or CT) datasets are already registered, it is often of interest to image the same patient over time to monitor progression of a disease or the effects of treatment. Obviously, MRI (or CT) datasets acquired over time are not registered because it is impossible to image exactly the same volume during different scans. Nevertheless, it is critical to register the sections from one dataset with those of the next dataset to monitor disease. Direct comparison (i.e., without registration) of 2D images would be misleading because it would be impossible to distinguish between changes due to misalignment and those due to the actual change in pathology. Correct alignment between datasets acquired over time is an important

challenge for brain tumor monitoring with MRI [67]. The registration methodologies that were introduced in this contribution can be used and adapted to register the images of MRI datasets acquired over time.

Registration is also becoming a necessity for ultrasound imaging. Specifically, constructing 3D ultrasound images usually necessitates alignment of several 2D images [68, 69] because motions (breathing, heartbeat, etc.) create artifacts. For this imaging modality, it may be possible to reconstruct (registered) 3D volumes from these 2D images in real time while the ultrasonic scan is being conducted. These 3D images may help in early detection/diagnostics of some diseases. Further, 3D images acquired in real time contain a lot of orientation information that might be helpful during complicated surgery.

Finally, the reconstructed 3D histologic volumes can be used as 3D computational phantoms for different wave propagation simulations and as imaging algorithm development tools. Several numerical techniques are now available to solve wave equations that need accurate models of the propagating media. For example, if the 3D histologic volumes could be converted to different 3D acoustic models by assigning acoustic properties to every voxel (i.e, speed of sound, density, attenuation, etc.), then computational algorithms could be used to solve acoustic wave equations [70] to study wave propagation phenomena in tissue.

6.2 Three-Dimensional Impedance Maps and Tissue Characterization

Chapters 4 and 5 demonstrated how it is possible to use 3DZMs for tissue characterization. Simulated 3DZMs were used to validate the estimation and FF-extraction strategies. Average size estimates obtained using the Gaussian FF showed excellent agreement with the independent ultrasound measurements. However, the Gaussian size estimates did not allow for distinction between the carcinoma and the sarcoma, whereas the 3DZM-deduced FFs allowed for statistical distinction between the three tumors.

6.2.1 Assignment of acoustic impedance

One of the critical and yet challenging steps of the 3DZM construction is the assignment of acoustic impedance values. The first 3DZM reconstructed used only

three different colors (rat fibroadenoma), then the scheme was refined to use five colors (mouse carcinoma) and finally seven (mouse sarcoma). Furthermore, for the 3DZM of the sarcoma, the differential staining was used to allow two different impedance values for the same tissue structures (Table 3.1).

Certainly, more improvement could be obtained by increasing the accuracy and the number of impedance values assigned to the different tissue structures. In some cases, it is difficult to measure acoustic properties of tissue microstructure, thus making the assignment of impedance values to different structures more challenging. However, an alternate technique might be used to deduce acoustic values by iteration. 3DZMs could be used as computational phantoms to simulate backscattered signals received by a given transducer. Then, comparison between simulation and ultrasonic experiments could be used to optimize the impedance values. At each step, the 3DZM would be updated until the simulated backscattered signals matched the signals obtained by ultrasonic measurements.

6.2.2 Resolution

Resolution of the 3DZM could be improved. In particular, the section thickness could be reduced in order to have a similar pixel resolution in all three dimensions (isotropic 3DZM). Reducing the section thickness would also increase the similarities between two consecutive sections. Thus, smaller section thickness would have the advantage to increase the efficiency and robustness of the registration algorithms.

6.2.3 Biological phantoms

One of the important challenges of the work presented in this dissertation is the validation of the 3DZMs as an accurate acoustic tissue model. It is obvious that if proven accurate, confidence in deducing FFs from 3DZMs would be tremendously increased, leading to many potential improvements of QUS methodologies. The only confidence at this point comes from the very similar scatterer size estimates obtained using the Gaussian FF (Table 5.2). This excellent agreement is obviously not enough to confidently state that the 3DZMs presented in this dissertation are accurate.

To validate further the 3DZMs, one approach would consist in being able to construct models of biological materials in a much more controlled way. These biological phantoms would contain a single type of biological scatterer (e.g., caviar eggs, frog eggs, sepharose beads, etc.) with a narrow and known size distribution

embedded in agar. The advantages of such phantoms are (1) they are weak scatterers that are similar to tissue, and (2) they can be used to validate (a basis for “truth”) both QUS and 3DZM methodologies. The biological phantoms allow volumes interrogated with QUS to be constructed into 3DZMs from serial slices (the soft scatterers can be sectioned). Further, a broad range of acoustic frequencies (1-70 MHz) can be used to deduce the impedance properties of the eggs or sepharose beads in the phantoms for evaluation of the 3DZM over a correspondingly broad range of spatial scales.

6.3 Identification of the Ultrasonic Scattering Sites

The initial motivation in the development of the 3DZMs was that they represent accurate morphological models of tissue microstructure which can aid in discovering scattering sites in tissue. Identifying the ultrasonic scattering sites would lead to great improvement of the diagnostic capabilities of QUS. Parameters estimated could then be chosen that actually describe histology of tissue microstructures. Then clinicians might be able to provide a diagnosis that is based on the ultrasonically obtained measurements of physical properties of tissue microstructure. Therefore, identifying the ultrasonic scattering sites may result in the possibility to develop novel and noninvasive diagnosis capabilities that are based on quantitative ultrasound strategies.

6.3.1 Identification using size estimates

One approach to come up with “tentative” scatterers consists of identifying tissue structures that have sizes similar to that of the size estimates. However, the simulation studies showed that using an inaccurate FF (e.g., Gaussian FF) may be misleading. In particular, mean scatterer size estimates were found in some case to be much larger ($> 25\%$) than the actual mean scatterer size.

Using the results displayed in Table 5.2, it may be possible to name potential scattering structures for each tumor. For the fibroadenoma, all the size estimates are near $100 \mu\text{m}$. The circular white structures, acini with neighboring epithelial cells, have diameters near $100 \mu\text{m}$ (Figure 5.18(a)). Thus, it is likely that for the fibroadenoma the anatomic structures responsible for scattering are the acini.

The carcinoma size estimates obtained with either the Gaussian or the deduced

FF (Table 5.2) do not correspond to any specific structures contained within the tissue. The histology is very dense with a lot of tumor cells (around $10 \mu\text{m}$ in diameter) and very little ECM (Figure 5.18(b)). Thus, the estimates probably indicate that the Gaussian FF and the deduced FF are not good scattering models for this tumor tissue. A recent study also demonstrated that carcinoma cells in pellet had the same ultrasonic sizes estimates (than in-vivo) using a Gaussian FF [26]. Thus, it is likely that individual cells combined with their inner constituents (e.g., cytoplasm, nuclei,...) are responsible for ultrasonic scattering.

For the sarcoma tumor, all the size estimates shown in Table 5.2 are in the range $30\text{-}40 \mu\text{m}$. This range is consistent with the diameters of the islands of tumor cells shown on Figure 5.18(c). Furthermore, the ECM background is really uniform, which adds confidence to state that the anatomic structures responsible for scattering may be the islands of tumor cells. Also, the individual tumor cells are too small (around $8 \mu\text{m}$ in diameter) for being individually responsible for scattering at the ultrasonic frequency considered ($-6 \text{ dB bandwidth } 10\text{-}25 \text{ MHz}$) because $ka = 0.33$ (with $a = 8/2 = 4 \mu\text{m}$, a frequency of 20 MHz and a speed of sound of 1540 m/s).

6.3.2 Identification using form factors

Another interesting approach to identify scattering structures would consist in using 3DZM-deduced FFs. Specifically, 3DZM-deduced FFs could be compared to ultrasound backscatter signatures from the same tissues. When the ultrasound measurements would converge with the 3DZM-deduced FFs, the FF-SAF duality (Section 2.3) would help to identify the scattering sources. Further, from the inverse Fourier transform of the 3DZM-deduced FF, a 3D acoustic model of the SAF of a scattering structure can be determined. Then, it might be possible to identify the scattering sites by comparison of the SAF characteristics with the histology. Validation of this strategy may come from biological phantoms where the position and structural make-up are controlled. The biological phantoms contain structures (e.g., caviar eggs, frog eggs, sepharose beads, etc.) with controlled sizes and number densities. Thus, it may be possible to deduce a theoretical FF from Faran's theory and compare it with the FF extracted from a 3DZM of the biological phantom.

6.4 Clinical Implementations

The long-term goal of this research work is the development of new imaging modalities for tumor diagnosis using ultrasound. A good thing is that clinical implementation of the QUS methodologies is not an overwhelming task. Modern clinical scanners can be connected to a personal computer allowing for a lot of storage and fast processing. Thus, real-time display of QUS images could easily become a reality.

Implementation of the QUS algorithms is not an overly computer-extensive task. For example, ultrasonic flow imaging that is now implemented in real-time on medical scanners is certainly more computationally extensive. Furthermore, if the QUS approaches were extended to human subjects, disease-specific FFs obtained for diverse types of human breast cancers could be stored in look-up tables allowing for fast processing (i.e., QUS image reconstruction) during the scanning.

One of the immediate limitations of clinical QUS would probably be the necessity of training clinicians to correctly interpret QUS images. Like any other imaging modality, clinicians would need to follow a training procedure in order to be able to understand what is displayed on the screen of the clinical scanner.

Another limitation of QUS scanners for human breast characterization is the depth of penetration of ultrasonic waves. As ultrasound attenuation increases with frequency, to go deep in tissue a lower frequency needs to be used. Using lower frequencies will lead to a lower resolution of the B-mode image. Furthermore, QUS techniques are also affected by frequency. The size of the statistical microstructures descriptions obtained using QUS methodologies are usually near $ka = 1$, where k is the wavenumber and a is a typical “radius” (i.e., half of a typical dimension) of the object. Thus, the QUS methodologies would tune into being sensitive to larger structures whose sizes would be greater than those of histologic features used by pathologists for diagnosis (Appendix A).

Attenuation along the propagation path is also a concern. For example, fat is a more attenuating medium than most other soft tissues. Thus, if a breast tumor is located behind a fat layer, it might be more challenging to detect it because of the important attenuation. Further, if attenuation is not estimated and compensated for, QUS results may be misleading. QUS characterizations may be inaccurate because attenuation is frequency-dependent which will lead to distorted backscattered power

spectra; QUS techniques rely on power spectra to characterize tissue microstructures. However, methodologies were developed to estimate acoustic attenuation along the propagation path of the ultrasonic wave [55] and to compensate for it [54].

Another clinical QUS application would consist in monitoring of disease. The 3DZM-derived FFs represent new tools to monitor healing or progress of a disease. Specifically, it seems reasonable to expect that QUS estimates would change with the pathological stage of a tumor because QUS methodologies are sensitive to change in microstructure and tumor microstructure evolves with diseases progression. Thus, making QUS methodologies available to trained clinicians may have great potential to follow how a disease is reacting to a specific treatment without the need for repetitive biopsies.

APPENDIX A

HISTOPATHOLOGIC FEATURES

This appendix briefly lists the histopathologic features used by pathologist to diagnose tissue. Features are assessed on stained histologic sections obtained from biopsies and are usually observed under light microscopy at the appropriate magnification factor (i.e, 10X, 20X, etc.). The list of features is presented below along with typical sizes (within parentheses):

- Overall growth pattern (millimeters)
- Capsule around the tumor (100s of μm)
- Organization of cells within tumor (20-40 μm)
- Penetration of cells through membrane, into connective tissue, and/or invasion into blood/lymph stream (20-40 μm)
- Morphology of cells within tumor (nucleus, nucleolus, cytoplasm) (5-10 μm)
- Presence of mitotic figures, abnormal mitotic figures or abnormally nucleated cells (5-10 μm)

For comparison purposes, Table A.1 lists wavelength of ultrasound for different frequencies assuming a propagation speed of 1540 m/s. Table A.1 demonstrates that even at high frequencies (e.g., 15 MHz) most of the histopathologic features are smaller than the ultrasound wavelength.

A.1 Table

Table A.1 Wavelength of ultrasound at typical clinical ultrasound frequencies assuming a propagation speed of 1540 m/s.

Frequency	Wavelength
1 MHz	1540 μm
2 MHz	770 μm
5 MHz	308 μm
10 MHz	154 μm
15 MHz	103 μm

APPENDIX B

DERIVATION OF THE GAUSSIAN-GAUSSIAN FF

This section provides the necessary details to integrate Eq. (2.31). The computation of Eq. (2.31) starts by remarking that

$$F_{a,\sigma}^{GG}(2k) = \Gamma I, \quad (\text{B.1})$$

where

$$\Gamma = \frac{1}{\sigma A} \frac{16\pi^{\frac{3}{2}}}{9\sqrt{2}}, \quad (\text{B.2})$$

and

$$I = \int_{-\infty}^{\infty} x^6 e^{-dk^2 x^2} e^{-\frac{1}{2} \left(\frac{x-a}{\sigma} \right)^2} dx, \quad (\text{B.3})$$

where $d = 0.827$. I is then rewritten as:

$$I = e^{-\frac{a^2}{2\sigma^2}} \int_{-\infty}^{\infty} x^6 e^{-x^2 \left[dk^2 + \frac{1}{2\sigma^2} \right] + x \frac{a}{\sigma}} dx. \quad (\text{B.4})$$

Using Eqs. (2.35) and (2.36), Eq. (B.4) reduces to

$$I = e^{-\frac{a^2}{2\sigma^2}} \int_{-\infty}^{\infty} x^6 e^{-B(k)x^2 + Cx} dx. \quad (\text{B.5})$$

Then, algebraic manipulations lead to

$$I = e^{-\frac{a^2}{2\sigma^2}} e^{\frac{C^2}{4B(k)}} \int_{-\infty}^{\infty} x^6 e^{-B(k) \left[x - \frac{C}{2B(k)} \right]^2} dx. \quad (\text{B.6})$$

Equation (B.6) can be rewritten to make the sixth moment of a new Gaussian distribution appear for which the mean, μ' , and the standard deviation, σ' are defined by

$$\mu' = \frac{C}{2B(k)}, \quad (\text{B.7})$$

$$\sigma'^2 = \frac{1}{2B(k)}. \quad (\text{B.8})$$

Then,

$$I = \frac{\sqrt{\pi} e^{-\frac{a^2}{2\sigma'^2} + \frac{C^2}{4B(k)}}}{\sqrt{B}} \left[\frac{1}{\sqrt{2\pi\sigma'^2}} \int_{-\infty}^{\infty} x^6 e^{-\frac{1}{2}\left(\frac{x-\mu'}{\sigma'}\right)^2} dx \right], \quad (\text{B.9})$$

where the term between brackets is the sixth moment of Gaussian probability distribution which is a tabulated quantity:

$$I = \frac{\sqrt{\pi} e^{-\frac{a^2}{2\sigma'^2} + \frac{C^2}{4B(k)}}}{\sqrt{B}} [\mu'^6 + 15\mu'^4\sigma'^2 + 45\mu'^2\sigma'^4 + 15\sigma'^6]. \quad (\text{B.10})$$

Inserting the value of μ' and σ' in Eq. (B.10) leads to:

$$I = \frac{\sqrt{\pi} e^{-\frac{a^2}{2\sigma'^2} + \frac{C^2}{4B(k)}}}{\sqrt{B}} \left[\frac{C^6}{64B^6(k)} + \frac{15C^4}{32B^5(k)} + \frac{45C^2}{16B^4(k)} + \frac{15}{64B^6(k)} \right]. \quad (\text{B.11})$$

Equations (2.33) and (2.34) are then easily obtained by using Eq. (B.11) in Eqs. (B.1) and (B.2).

APPENDIX C

DERIVATION OF A POWER SPECTRUM

This appendix derives a power spectrum step by step to demonstrate that the power spectra is discontinuous at zero frequency (i.e., $k = 0$). To simplify notation, the scatterers are assumed isotropic and described by the form factor, $FF(ka)$. The scattering volume considered contains n scatterers. Further, the n scatterers have the same radius a and have an acoustic impedance of z . The background impedance is z_0 . Basic Fourier transform properties lead to the following expression for the power spectrum $PS(k)$:

$$PS(k) = E \left[\left| \sum_{p=1}^n \frac{z - z_0}{z_0} \sqrt{FF(ka)} \exp(i [k_x x_p + k_y y_p + k_z z_p]) \right|^2 \right], \quad (C.1)$$

where $E[\bullet]$ symbolizes taking the expected value, and x_p , y_p , and z_p characterize the random location of the n^{th} scatterer within the scattering volume. The terms k_x , k_y , and k_z are the frequency variables of the 3D Fourier transform ($k = \sqrt{k_x^2 + k_y^2 + k_z^2}$). Expanding the squared term in Eq. (C.1) leads to

$$PS(k) = FF(ka) \Lambda^2 E \left[\sum_{p,q=1}^n \exp(i [k_x(x_p - x_q) + k_y(y_p - y_q) + k_z(z_p - z_q)]) \right], \quad (C.2)$$

where $\Lambda^2 = \left[\frac{z - z_0}{z_0} \right]^2$. Using $\sum_{p,q=1}^n = \sum_{p=q} + \sum_{p \neq q}$, Eq. (C.2) reduces to

$$PS(k) = FF(ka) \Lambda^2 E \left[n + \sum_{p \neq q} \exp(i [k_x(x_p - x_q) + k_y(y_p - y_q) + k_z(z_p - z_q)]) \right]. \quad (C.3)$$

The sum term is now symmetric with respect to p and q thus:

$$PS(k) = FF(ka) \Lambda^2 E \left[n + 2 \sum_{p > q} \cos [k_x(x_p - x_q) + k_y(y_p - y_q) + k_z(z_p - z_q)] \right]. \quad (C.4)$$

$$PS(k) = FF(ka)\Lambda^2 \left(n + 2E \left[\sum_{p>q} \cos [k_x(x_p - x_q) + k_y(y_p - y_q) + k_z(z_p - z_q)] \right] \right). \quad (C.5)$$

The term within the expected value is a sum of cosines of random numbers when $k > 0$; thus, its expected value is zero. However, when $k = 0$, the term within the expected value sign is deterministic and equal to $\sum_{p>q} 1 = \frac{n(n-1)}{2}$. Thus, the power spectrum is discontinuous at $k = 0$ and is equal to

$$PS(k) = \begin{cases} n \left[\frac{z-z_0}{z_0} \right]^2 FF(ka) & \text{if } k > 0 \\ n^2 \left[\frac{z-z_0}{z_0} \right]^2 FF(ka) & \text{if } k = 0 \end{cases}. \quad (C.6)$$

Thus, Eq. (C.6) demonstrates why it was stated in Section 4.1 that $S'(0)$ is not usable.

Another way to interpret Eq. (C.6) is obtained by taking the limit of $\frac{PS}{n}$ when $n \rightarrow \infty$:

$$\lim_{n \rightarrow \infty} \frac{PS(k)}{n} = \left[\frac{z-z_0}{z_0} \right]^2 FF(ka) [1 + \delta(k)], \quad (C.7)$$

where $\delta(k)$ is the delta dirac function. Equation (C.6) clearly demonstrates that the spectrum of a random 3DZM is discontinuous at $k = 0$. Thus, the value of the power spectrum at $k = 0$ cannot be used to retrieve the acoustic concentration and the gain factor G_a needs to be introduced as it is done in Section 4.1.

APPENDIX D

OBLIQUE CUT THROUGH A THREE-DIMENSIONAL HISTOLOGIC VOLUME

The possibility of extracting an oblique section from a reconstructed 3D histologic volume is illustrated by Figure D.1. Figure D.1(a) shows the same 3D rendering as Figure 3.19 in which the green lines were added to indicate the oblique cutting plane. Figure D.1(b) shows the 3D rendering after the oblique cut has been performed, and Figure D.1(c) shows the extracted oblique section whose longest dimensions are 230 μm by 165 μm . Figure D.1(c) is of interest to pathologists because it displays new information that was not available from the original individual 2D sections. To assess the quality of the oblique section, it was submitted to a board-certified pathologist under blind conditions who was able to recognize the histopathologic characteristics of the tissue that were diagnostically consistent with an EHS sarcoma such as the islands of tumor cells intermixed with ECM (right half of Figure 3.10(c)).

D.1 Figure

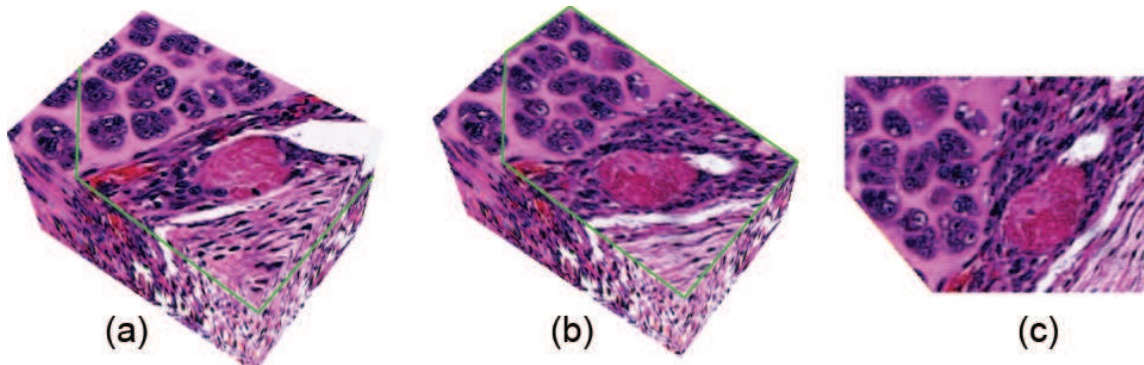


Figure D.1 Illustration of an oblique section. (a) 3D rendering from the EHS dataset (same as Figure 3.19), green lines shows an oblique cutting plane. (b) 3D rendering after an oblique cut through the volume. (c) 2D oblique section.

REFERENCES

- [1] A. Goldstein, *Medical Ultrasonic Diagnostics*. New York: Academic Press, 1999.
- [2] G. Muller, B. Chance, R. Alfano, S. Arridge, J. Beuthan, E. Gratton, M. Kaschke, B. Masters, S. Svanberg, and P. van der Zee, *Medical Optical Tomography: Functional Imaging and Monitoring*. Bellingham, WA: SPIE Press, 1993.
- [3] Z.-P. Liang and P. C. Lauterbur, *Principles of Magnetic Resonance Imaging: A Signal Processing Perspective*. Piscataway, NJ: IEEE Press, 1999.
- [4] “National Cancer Institute’s plans and priorities for cancer research fiscal year 2003,” National Cancer Institute, Tech. Rep., 2003.
- [5] C. P. McPherson, K. K. Swenson, G. Jolitz, and C. L. Murray, “Survival among women ages 40-49 years with breast carcinoma according to method of detection,” *Cancer*, vol. 79, pp. 1923–1932, 1997.
- [6] M. E. Costanza and K. L. Edmiston, “Breast cancer screening: Early recognition,” *Comp. Ther.*, vol. 23, pp. 7–12, 1996.
- [7] M. F. Insana, R. F. Wagner, and D. G. Brown, “Describing small-scale structure in random media using pulse-echo ultrasound,” *J. Acoust. Soc. Am.*, vol. 87, pp. 179–192, 1990.
- [8] J. E. Perez, J. G. Miller, B. Barzilai, S. Wickline, G. A. Mohr, K. Wear, Z. Vered, and B. E. Sobel, “Quantitative characterization of myocardium with ultrasonic imaging,” *J. Nucl. Med. Allied Sci.*, vol. 32, pp. 149–157, 1988.
- [9] F. L. Lizzi, M. Greenebaum, E. J. Feleppa, M. Elbaum, and D. J. Coleman, “Theoretical framework for spectrum analysis in ultrasonic tissue characterization,” *J. Acoust. Soc. Am.*, vol. 73, pp. 1366–1373, April 1983.
- [10] F. L. Lizzi, M. Ostromogilsky, E. J. Felepa, M. C. Rorke, and M. M. Yaremko, “Relationship of ultrasonic spectral parameters to features of tissue microstructure,” *IEEE Trans. Ulatrson. Ferroelectr. Freq. Control*, vol. 33, pp. 319–329, May 1986.
- [11] M. F. Insana, J. G. Wood, and T. J. Hall, “Identifying acoustic scattering sources in normal renal parenchyma in vivo by varying arterial and ureteral pressures,” *Ultrasound Med. Biol.*, vol. 17, pp. 613–626, 1991.

- [12] E. J. Feleppa, F. L. Lizzi, D. J. Coleman, and M. M. Yaremko, "Diagnostics spectrum analysis in ophthalmology: A physical perspective," *Ultrasound Med. Biol.*, vol. 12, pp. 623–631, 1986.
- [13] K. C. Balaji, W. R. Fair, E. J. Feleppa, C. R. Porter, H. Tsai, T. Liu, A. Kalisz, S. Urban, and J. Gillespie, "Role of advanced 2 and 3-dimensional ultrasound for detecting prostate cancer," *J. Urology*, vol. 168, pp. 2422–2425, 2002.
- [14] E. Feleppa, A. Kalisz, J. Sokil-Melgar, F. L. Lizzi, L. Tian, A. L. Rosado, M. C. Shao, W. R. Fair, W. Yu, M. S. Cookson, V. E. Reuter, and W. D. W. Heston, "Typing prostate tissue by ultrasonic spectrum analysis," *IEEE Trans. Ultrasound. Ferroelectr. Freq. Control*, vol. 43, pp. 609–619, 1996.
- [15] B. S. Garra, M. F. Insana, I. A. Sesterhenn, T. J. Hall, R. F. Wagner, C. Rotellar, J. Winchester, and R. K. Zeman, "Quantitative ultrasonic detection of parenchymal structural change in diffuse renal disease," *Inv. Radiology*, vol. 29, pp. 134–140, 1994.
- [16] M. F. Insana and T. J. Hall, "Parametric ultrasound imaging from backscatter coefficient measurements: Image formation and interpretation," *Ultrason. Imaging*, vol. 12, pp. 245–267, 1990.
- [17] T. J. Hall, M. F. Insana, L. A. Harrison, and G. G. Cox, "Ultrasonic measurement of glomerular diameters in normal adult humans," *Ultrasound Med. Biol.*, vol. 22, pp. 987–997, 1996.
- [18] M. F. Insana, T. J. Hall, J. G. Wood, and Z. Y. Yan, "Renal ultrasound using parametric imaging technique to detect changes in microstructure and function." *Inv. Radiology*, vol. 28, pp. 720–725, 1993.
- [19] K. K. Shung and G. A. Thieme, *Ultrasonic Scattering in Biological Tissues*. Boca Raton, FL: CRC Press, 1993.
- [20] F. Padilla, F. Peyrin, and P. Laugier, "Prediction of backscatter coefficient in trabecular bones using a numerical model of three-dimensional microstructure," *J. Acoust. Soc. Am.*, vol. 113, pp. 1122–1129, February 2003.
- [21] J. Mamou, M. L. Oelze, W. D. O'Brien, Jr., and J. F. Zachary, "Identifying ultrasonic scattering sites from three-dimensional impedance maps," *J. Acoust. Soc. Am.*, vol. 117, pp. 413–423, 2005.
- [22] J. Mamou, M. L. Oelze, J. F. Zachary, and W. D. O'Brien, Jr., "Ultrasound scatterer size estimation technique based on a 3D acoustic impedance map from histologic sections," in *Proceedings of the 2003 IEEE Ultrasonics Symposium*, 2003, pp. 1022–1025.

- [23] M. L. Oelze, J. F. Zachary, and W. D. O'Brien, Jr., "Parametric imaging of rat mammary tumors *in vivo* for the purposes of tissue characterization," *J. Ultrasound Med.*, vol. 21, pp. 1201–1210, 2002.
- [24] M. L. Oelze, W. D. O'Brien, Jr., and J. F. Zachary, "Differentiation and characterization of rat mammary fibroadenomas and 4T1 mouse carcinomas using quantitative ultrasound imaging," *Trans. Med. Im.*, vol. 23, pp. 764–771, 2004.
- [25] M. L. Oelze, J. F. Zachary, and W. D. O'Brien, Jr., "Differentiation of tumors types *in vivo* by scatterer property estimates and parametric images using ultrasound backscatter," in *Proceedings of the 2003 IEEE Ultrasonics Symposium*, 2003, pp. 1014–1017.
- [26] M. L. Oelze, W. D. O'Brien, Jr., and J. F. Zachary, "Characterization of solid tumors in mice using ultrasound backscatter over a broad range of frequencies (10 to 90 MHz)," presented at the 4th International Conference on Ultrasound Biomicroscopy, Arden House, New York, 2004.
- [27] J. J. Faran, "Sound scattering by solid cylinders and spheres," *J. Acoust. Soc. Am.*, vol. 23, pp. 405–418, 1951.
- [28] R. Hickling, "Analysis of echoes from a solid elastic sphere in water," *J. Acoust. Soc. Am.*, vol. 34, pp. 1582–1592, 1962.
- [29] V. C. Anderson, "Sound scattering from a fluid sphere," *J. Acoust. Soc. Am.*, vol. 22, pp. 426–431, 1950.
- [30] P. M. Morse and K. U. Ingard, *Theoretical Acoustics*. New York: McGraw-Hill, 1968.
- [31] A. V. Oppenheim, R. W. Schaffer, and J. R. Buck, *Discrete-Time Signal Processing*. Upper Saddle River, NJ: Prentice Hall, 1999.
- [32] M. L. Oelze, J. F. Zachary, and W. D. O'Brien, Jr., "Characterization of tissue microstructure using ultrasonic backscatter: Theory and technique for optimization using a Gaussian form factor," *J. Acoust. Soc. Am.*, vol. 112, pp. 1202–1211, 2002.
- [33] M. F. Insana, "Modeling acoustic backscatter from kidney microstructure using an anisotropic correlation function," *J. Acoust. Soc. Am.*, vol. 97, pp. 649–655, 1995.
- [34] L. A. Frizzell, E. L. Carstensen, and J. F. Dyro, "Shear properties of mammalian tissues at low megahertz frequencies," *J. Acoust. Soc. Am.*, vol. 60, pp. 1409–1411, 1976.

- [35] V. Caselles, J.-L. Lisani, J.-M. Morel, and G. Sapiro, “Shape preserving local histogram modification,” *Trans. Image Processing*, vol. 8, pp. 220–230, 1999.
- [36] M. Abramowitz and I. Stegun, *Handbook of Mathematical Functions with Formulas, Graphs, and Mathematical Tables*, 9th ed. New York: Dover, 1972.
- [37] J. V. Hajnal, D. L. G. Hill, and D. J. Hawkes, *Medical Image Registration*. Boca Raton, FL: CRC Press, 2001.
- [38] J. P. W. Pluim, J. B. A. Maintz, and M. A. Viergever, “Mutual-information-based registration of medical images: A survey,” *Trans. Med. Im.*, vol. 22, pp. 986–1004, 2003.
- [39] J. Kybic and M. Unser, “Fast parametric elastic image registration,” *Trans. Image Processing*, vol. 12, pp. 1427–1442, 2003.
- [40] C. W. Washington and M. I. Miga, “Modality independent elastography (MIE): A new approach to elasticity imaging,” *Trans. Med. Im.*, vol. 23, pp. 1117–1128, 2004.
- [41] G. P. Penney, J. Weese, J. A. Little, P. Desmedt, D. L. G. Hill, and D. J. Hawkes, “A comparison of similarity measures for use in 2D–3D medical image registration,” *Trans. Med. Im.*, vol. 17, pp. 586–595, 1998.
- [42] A. A. Cole-Rhodes, K. L. Johnson, J. LeMoigne, and I. Zavorin, “Multiresolution registration of remote sensing imagery by optimization of mutual information using a stochastic gradient,” *Trans. Image Processing*, vol. 12, pp. 1495–1511, 2003.
- [43] C. Studholme, D. L. G. Hill, and D. J. Hawkes, “An overlap invariant entropy measure of 3D medical image alignment,” *Pattern Recogn.*, vol. 32, pp. 71–86, 1999.
- [44] Y.-M. Zhu, “Volume image registration by cross-entropy optimization,” *Trans. Med. Im.*, vol. 21, pp. 174–180, 2002.
- [45] F. Maes, D. Vandermeulen, and P. Suetens, “Comparative evaluation of multiresolution optimization strategies for multimodality image registration by maximization of mutual information,” *Med. Image Anal.*, vol. 3, pp. 373–386, 1999.
- [46] M. J. D. Powell, “An efficient method for finding the minimum of a function of several variables without calculating derivatives,” *Computer J.*, vol. 7, pp. 155–162, 1964.

- [47] F. Maes, A. Collignon, D. Vandermeulen, G. Marchal, and P. Suetens, “Multimodality image registration by maximization of mutual information,” *Trans. Med. Im.*, vol. 16, pp. 187–198, 1997.
- [48] J. A. Nelder and R. Mead, “A simplex method for function minimization,” *Computer J.*, vol. 7, pp. 308–313, 1965.
- [49] N. A. Dodgson, “Quadratic interpolation for image resampling,” *Trans. Image Processing*, vol. 6, pp. 1322–1326, 1997.
- [50] S. A. Goss, R. L. Johnston, and F. Dunn, “Comprehensive compilation of empirical ultrasonic properties of mammalian tissues,” *J. Acoust. Soc. Am.*, vol. 64, pp. 423–457, 1978.
- [51] S. A. Goss, R. L. Johnston, and F. Dunn, “Comprehensive compilation of empirical ultrasonic properties of mammalian tissues II,” *J. Acoust. Soc. Am.*, vol. 68, pp. 93–108, 1980.
- [52] F. A. Duck, *Physical Properties of Tissue. A Comprehensive Reference Book*. New York: Academic Press, 1990.
- [53] E. L. Madsen, M. F. Insana, and J. A. Zagzebski, “Method of data reduction for accurate determination of acoustic backscatter coefficients,” *J. Acoust. Soc. Am.*, vol. 76, pp. 913–923, 1984.
- [54] M. L. Oelze and W. D. O’Brien, Jr., “Frequency-dependent attenuation-compensation functions for ultrasonic signals backscattered from random media,” *J. Acoust. Soc. Am.*, vol. 111, pp. 2308–2319, 2002.
- [55] T. A. Bigelow, M. L. Oelze, and W. D. O’Brien, Jr., “Estimation of total attenuation and scatterer size from backscattered ultrasound waveforms,” *J. Acoust. Soc. Am.*, vol. 117, pp. 1–10, 2005.
- [56] T. A. Bigelow and W. D. O’Brien, Jr., “Scatterer size estimation in pulse-echo ultrasound using focused sources: Calibration measurements and phantom experiments,” *J. Acoust. Soc. Am.*, vol. 116, pp. 594–602, 2004.
- [57] E. L. Madsen, F. Dong, G. R. Frank, B. S. Garra, K. A. Wear, T. Wilson, J. A. Zagzebski, H. L. Miller, K. K. Shung, S. H. Wang, E. J. Feleppa, T. Liu, W. D. O’Brien, Jr., K. A. Topp, N. T. Sanghvi, A. V. Zaitsev, T. J. Hall, F. B. Fowlkes, O. D. Kripfgans, and J. G. Miller, “Interlaboratory comparison of ultrasonic backscatter, attenuation, and speed measurements.” *J. Ultrasound Med.*, vol. 18, pp. 615–631, 1999.

- [58] K. A. Wear, T. A. Stiles, G. R. Frank, E. L. Madsen, F. Cheng, E. J. Feleppa, C. S. Hall, B. S. Kim, P. Lee, W. D. O'Brien, Jr., M. L. Oelze, B. I. Raju, K. K. Shung, T. A. Wilson, and J. R. Yuan, "Interlaboratory comparison of ultrasonic backscatter coefficient measurements from 2 to 9 MHz." *J. Ultrasound Med.*, to be published.
- [59] M. Unser, P. Thevenaz, and L. Yaroslavsky, "Convolution-based interpolation for fast, high quality rotation of images," *Trans. Image Proc.*, vol. 4, pp. 1371–1381, 1995.
- [60] Y. Keller, A. Averbuch, and M. Israeli, "Pseudopolar-based estimation of large translations, rotations, and scalings in images," *Trans. Image Processing*, vol. 14, pp. 12–22, 2005.
- [61] G. J. Grevera and J. K. Udupa, "An objective comparison of 3D image interpolation methods," *Trans. Med. Im.*, vol. 17, pp. 642–652, 1998.
- [62] G. J. Grevera and J. K. Udupa, "A task-specific evaluation of three-dimensional image interpolation techniques," *Trans. Med. Im.*, vol. 18, pp. 137–143, 1999.
- [63] R. P. Woods, S. R. Cherry, and J. C. Maziotta, "Rapid automated aligning and reslicing PET images," *J. Comput. Assist. Tomogr.*, vol. 22, pp. 620–633, 1992.
- [64] J. Kim and J. A. Fessler, "Intensity-based image registration using robust correlation coefficients," *Trans. Med. Im.*, vol. 23, pp. 1430–1444, 2004.
- [65] R. Chamgoulov, P. Lane, and C. MacAulay, "Optical computed-tomographic microscope for three-dimensional quantitative histology," *Cell. Oncol.*, vol. 26, pp. 319–327, 2004.
- [66] J. Rosenthal, V. Mangal, D. Walker, M. Bennett, T. J. Mohun, and C. W. Lo, "Rapid high resolution three-dimensional reconstruction of embryos with episcopic fluorescence image capture," *Birth Defects Res.*, vol. 72, pp. 213–223, 2004.
- [67] A. Oatridge, J. V. Hajnal, N. Saeed, E. S. Newlands, W. L. Curati, S. J. White, B. K. Puri, and G. M. Bydder, "Subvoxel image registration of multislice (2D) magnetic resonance images in patients with high-grade gliomas of the brain," *Clin. Radiol.*, vol. 57, pp. 1098–1108, 2002.
- [68] E. Steen and B. Olstad, "Volume rendering of 3D medical ultrasound data using direct feature mapping," *Trans. Med. Im.*, vol. 13, pp. 517–525, 1994.
- [69] R. Shekhar and V. Zagrodsky, "Mutual information-based rigid and nonrigid registration of ultrasound volumes," *Trans. Med. Im.*, vol. 21, pp. 9–21, 2002.

- [70] M. Tabei, T. D. Mast, and R. C. Waag, “A k -space method for coupled first-order acoustic propagation equations,” *J. Acoust. Soc. Am.*, vol. 111, pp. 53–63, 2002.

AUTHOR'S BIOGRAPHY

Jonathan Mamou was born in Saint-Germain-En-Laye, France, on August 10, 1978. After graduating high-school in July 1996, he enrolled in the mathematics and physics preparatory classes at Lycée Thiers in Marseille, France. In August 1998, he was admitted to the Ecole Nationale Supérieure des Télécommunications in Paris, France. After graduating in July 2000, he worked as an intern in video processing software company, Montage Group, in New York. In January 2001, he began his graduate studies in electrical and computer engineering at the University of Illinois at Urbana-Champaign. His master's thesis in the Bioacoustics Research Laboratory under the direction of Professor William D. O'Brien, Jr., involved acoustic imaging in soil. After earning his M.S. in May 2002, Mr. Mamou remained in the Bioacoustics Research Laboratory to conduct research on ultrasonic tissue characterization and three-dimensional acoustic modeling of tissues. He completed his Ph.D. dissertation in May 2005. He is also a certified H.M.D. Tae Kwon Do Black Belt and Instructor. Mr. Mamou was an Avery Brundage scholar during scholar years 2003-2004 and 2004-2005. In 2005, he was also awarded the R. T. Chien memorial award by the Department of Electrical and Computer Engineering.